CONFINED QUANTUM FERMIONIC SYSTEMS

A Thesis
Presented to
The Academic Faculty

by

Ying Li

In Partial Fulfillment
of the Requirements for the Degree
Doctor of Philosophy in the
School of Physics

Georgia Institute of Technology
May 2009

CONFINED QUANTUM FERMIONIC SYSTEMS

Approved by:

Professor Uzi Landman, Advisor
School of Physics
Georgia Institute of Technology

Professor Mei-Yin Chou
School of Physics
Georgia Institute of Technology

Professor Mostafa A. El-Sayed
School of Chemistry and Biochemistry
Georgia Institute of Technology

Doctor Robert Barnett
School of Physics
Georgia Institute of Technology

Doctor Constantine Yannouleas
School of Physics
Georgia Institute of Technology

Date Approved: Oct 28, 2008

To my mother,

from whom I gain my inner strength.

ACKNOWLEDGEMENTS

First, I would like to express my sincere gratitude to my advisor Professor Uzi Landman, for his broad vision, deep insight, and sparking inspiration throughout the entire course of my doctoral work.

I'm deeply indebted to Dr. Robert Barnett and and Dr. Constantine Yannouleaus for their valuable guidance and stimulating instructions.

I am also grateful to all the other members of the Computational Material Science Center for their help and discussions.

Lastly, I would like to thank my family and friends for their support and caring during all the years in my graduate study.

TABLE OF CONTENTS

LIST OF TABLES

LIST OF FIGURES

SUMMARY

This thesis consists of two parts. The first two chapters belong to the first part, whereas chapter III and chapter IV belong to the second part.

In the first part, the properties of excess electrons in water clusters are studied via a hybrid quantum and classical mechanics method. The existence of the solvated electron in water was experimentally demonstrated long ago, and it is among the most interesting charged species. However, a satisfactory characterization of the water clusters has always been a challenge. In our simulation, we treat a region of the cluster nearest to the centroid of the excess electron distribution quantum mechanically, while the rest of the water molecules are treated classically. The binding energies of a localized excess electron are calculated in clusters with sizes ranging from 16 to 300. The density distributions of the excess electrons verify the existence of both surface localization mode and interior localization model. We found that the energetically favored localization mode depended on the sizes of the clusters. The transition between those two localization modes are explored with comparison to the experimental results in [22].

In the second part, the energy spectra, spin configurations, and entanglement characteristics of a system of four electrons in lateral double quantum dots are investigated using exact diagonalization (EXD), as a function of interdot separation, applied magnetic field, and strength of interelectron repulsion. A distinctly different quantum behavior is found compared to that of circular single quantum dots. As a function of the magnetic field, the energy spectra exhibit a low-energy band consisting of a group of six states, with the number six being a consequence of the conservation

of the total spin of the four electrons and the ensuing spin degeneracies. These six states appear to cross at a single value of the magnetic field, with the crossing point becoming sharper for larger interdot distances. As the strength of the Coulomb repulsion increases, the six states tend to become degenerate and a well defined energy gap separates them from the higher-in-energy excited states. The appearance of the low-energy band is a consequence of the formation of a Wigner supermolecule, with the four electrons being localized at the vertices of a rectangular parallelogram. Using the spin-resolved pair-correlation functions, one can map the EXD many-body wave functions onto the spin functions associated with the four localized electrons. Analogies with nanomagnets, such as finite Heisenberg clusters, are discussed. The ability to determine associated spin functions enables investigations concerning entanglement properties of the system of four electrons. In particular, the formation of Wigner supermolecules generates EXD solutions belonging to the class of strongly entangled states referred to as N-qubit Dicke states in the quantum-information literature.

PART I

EXCESS ELECTRON IN WATER CLUSTERS

CHAPTER I

HYBRID QM/MM SIMULATION FOR WATER CLUSTERS

Water is a common chemical substance that is essential for the survival of all known forms of life. About 1.460 petatonnes (Pt) of water covers 71% of the Earth's surface, and it composes roughly 70% of the human body mass. Experiments allow the measurement of many properties of water like density, diffusion coefficient, heat capacity, melting and boiling temperatures. Moreover, theoretical and computational modeling, especially taking into account current advances in computer simulations, provides insight into systems in which water plays a fundamental role at the microscopic level. Of course, the accuracy of the computational simulation depends on the underlying methodologies we employ to describe water.

In this chapter, we present a hybrid quantum mechanical and molecular mechanics(QM/MM) method to investigate water clusters with an excess electron. Both computational method alone has its strength and weakness. Molecular mechanical methods can calculate large compounds fast with limitations in accuracy and details in chemical environment. Quantum mechanics methods can treat the electronic degree of freedom accurately at the cost of huge computational resources. The hybrid QM/MM method, which treats a crucial portion of a large system quantum mechanically while incorporating the remaining system classically, is designed to give efficient results that has a reasonable level accuracy without the sacrifice of speed.

The development of accurate and reliable methods for QM/MM descriptions has

been a major goal of computational physics for over the past decade. In our formulation, the hamiltonian of the hybrid QM/MM system has the following form:

$$H_{QM/MM} = H_{QM} + H_{MM} + V_{QM/MM} \tag{1.1}$$

where H_{QM} and H_{MM} are the hamiltonian associated with the QM and MM regions respectively, while $V_{QM/MM}$ is the interaction between QM and MM components. The rest of this chapter will explain the hybrid QM/MM approach to model excess electrons in water clusters in detail.

1.1 Molecular Mechanics Region

In this section, we will discuss the methods employed to treat the molecular mechanics region in the water clusters. Two issue will be addressed here. One is the TIP3P model that we use to describe the classical water molecules. The other is the algorithm we applied to conduct molecular mechanics simulation.

1.1.1 TIP3P water model

Many water models have been proposed in the simulations of water clusters, liquid water, and aqueous solutions with explicit solvent. They can be classified by the number of points used to define the model (atoms plus dummy sites), whether the structure is rigid or flexible, and whether the model includes polarization effects.

In our simulation, we employ the TIP3P model for water molecule.(see Fig. 1). It treats each water molecule with 3 sites, corresponding to the three atoms of the water molecule. The hydrogen atoms and the oxygen atom are linked through flexible bonds, and the angle between the bonds is also flexible. The positive charges are located at the nuclei of the hydrogen atoms, while the negative charges are located along the HOH angle bisector. Besides, the oxygen atom also gets the Lennard-Jones parameters. The electrostatic interaction is modeled using Coulomb's Law, and the dispersion and repulsion forces using the Lennard-Jones potential, which is

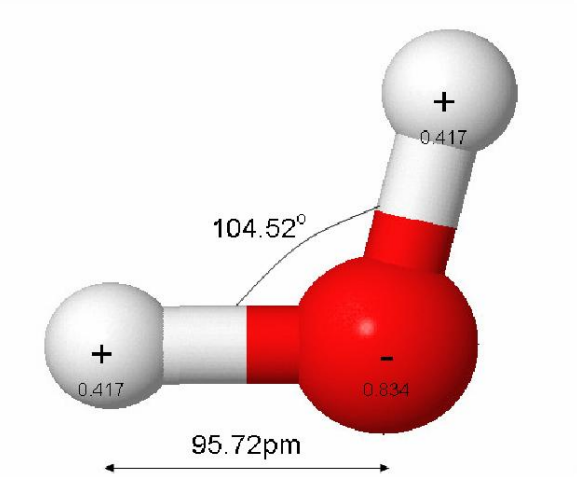

Figure 1: TIP3P model for water molecule.

Table 1: Parameters of TIP3P model for water molecules

r(OH),Å	HOH,deg	A×10^{-3},kcal $(Å)^12$/mol	B,kcal $(Å)^6$/mol	q(O)	q(H)
0.9572	104.52	582.0	595.0	-0.834	+0.417

represented by

$$E_{ab} = \sum_{i}^{on\ a} \sum_{j}^{on\ b} \frac{k_C q_i q_j}{r_{ij}} + \frac{A}{r_{OO}^{12}} - \frac{B}{r_{OO}^{6}} \tag{1.2}$$

where k_C, the electrostatic constant, has a value of 332.1Å×kcal/mol; q_i is the partial charges relative to the charge of an electron; r_{ij} is the distance between two atoms. The Lennard-Jones terms only apply to oxygen atoms, and A and B are the Lennard-Jones parameters. See Table 1 for all the parameters employed in the TIP3P model[66]. Those parameters have been chosen to yield reasonable structural and energetic results for both gas-phase dimers and pure liquids.

1.1.2 Algorithm for molecular dynamics simulation

Usually, molecular dynamics (MD) refers to the computational method that calculates statistical properties of an ensemble of particles by tracking the trajectories of each particle in the system. Molecular dynamics simulations are in many respects very

similar to real experiments. First, we select a model system consisting of N particles and we solve Newton's equations of motion for this system until the properties of the system do not change with time, which indicates the system has reached equilibrium. Then we perform the actual measurement. We will concentrate on the first part of the simulation in this section.

For a system consisting of N interactive particles, the equations of motion are:

$$m_i \dot{\mathbf{v}}_i = \mathbf{f}_i, \qquad i = 1, 2, \ldots, N \tag{1.3}$$

$$\mathbf{f}_i = -\frac{\partial}{\partial \mathbf{r}_i} V(\sum_{j=1}^{N} \mathbf{r}_j), \qquad i = 1, 2, \ldots, N \tag{1.4}$$

$$\dot{\mathbf{r}}_i = \mathbf{v}_i, \qquad i = 1, 2, \ldots, N \tag{1.5}$$

where m_i is the mass of the i-th particle, $\mathbf{r}_i$ is its position, $\mathbf{v}_i$ is the velocity, $\mathbf{f}_i$ is the force on this particle, and $V(\sum_{i=1}^{N} \mathbf{r}_i)$ is the interaction potential of the entire system. Note that $\mathbf{r}_i$, $\mathbf{f}_i$ and $\mathbf{v}_i$ here are three-dimensional vectors. In this way, the dynamics of the system is depicted by the 6N first order Newtonian ordinary equations. However, it is very often that the analytic solutions to the 6N ordinary equations are not available; and only numerical solutions can be obtained to some systems with a modest particle number N, with the help of modern computers. Therefore, it represents an interface between laboratory experiments and the theory, and can be understood as a "virtual experiment". The most time-consuming part of almost all molecular dynamics simulations is the calculation of the force acting on every particle. If we consider a model system consisting of N particles with pairwise additive interactions, the time needed for the evaluation of forces scales as N^2 with no tricks. There exist efficient techniques to speed up the evaluation of both short-range and long-range forces. But since for our systems, N is in the range of 10^1 to 10^2, considerably small in molecular dynamics simulation. We will skip this part now. You can go to [14] for some details in saving cpu time at the evaluation of pairwise forces.

Now that we have computed all forces between the particles, we can integrate Newton's equations of motion. In molecular dynamics, the Newton's equations of motion are integrated using finite difference methods. However, since the system may comprise a large number of particles, the choice for the appropriate algorithms is very limited. There are several criteria applied to the choice [4]. Among them, most importantly, is wether the algorithm is fast enough and conserves the total energy well. The Verlet algorithm [62] is one of those desirable algorithms. It was first employed by Verlet for a Lennard-Jones system in 1967. The original form of the Verlet algorithm is [4]:

$$\mathbf{r}_i(t+\delta t) = 2\mathbf{r}_i(t) - \mathbf{r}_i(t-\delta t) + \delta t^2 \frac{\mathbf{f}_i(t)}{m_i}, \qquad i = 1, 2, \ldots, N \tag{1.6}$$

where

$$\mathbf{f}_i(t) = -\frac{\partial}{\partial \mathbf{r}_i} V(\sum_{j=1}^{N} \mathbf{r}_j) \tag{1.7}$$

is the total force on the i-th particle and δt is the time step for each integration. Note that, in this form the Verlet algorithm directly integrates the 3N second order Newtonian equations of motion with no velocity appearing in the formula, and the velocity of each particle is obtained by an extra finite difference formula along the trajectories. For example [4],

$$\mathbf{v}_i(t) = \frac{\mathbf{r}_i(t+\delta t) - \mathbf{r}_i(t-\delta t)}{2\delta t}. \tag{1.8}$$

In practice, a variance of the Verlet algorithm is more convenient for implementation. It is called "velocity Verlet" [63, 4] and was proposed by Swope, Andersen, Berens, and Wilson in 1982. With the velocity explicitly expressed, the formula for the "velocity Verlet" is [4],

$$\mathbf{r}_i(t+\delta t) = \mathbf{r}_i(t) + \delta t \mathbf{v}_i(t) + \frac{\delta t^2}{2m_i}\mathbf{f}_i(t), \tag{1.9}$$

$$\mathbf{v}_i(t+\delta t) = \mathbf{v}_i(t) + \frac{\delta t}{2m_i}\left[\mathbf{f}_i(t) + \mathbf{f}_i(t+\delta t)\right]. \tag{1.10}$$

It is easy to verify that the "velocity Verlet" algorithm is equivalent to the original form by replacing the velocity in Eq. (1.9) with

$$\mathbf{v}_i(t) = \frac{\mathbf{r}_i(t) - \mathbf{r}_i(t - \delta t)}{\delta t}. \tag{1.11}$$

The entire "velocity Verlet" algorithm is divided into three steps in programming. In each iteration $\mathbf{r}_i(t+\delta t)$ is first calculated through Eq. (1.9) and part of the velocity $\mathbf{v}_i(t + \delta t)$ is calculated as,

$$\mathbf{v}_i^{part}(t + \delta t) = \mathbf{v}_i(t) + \frac{\delta t}{2m_i}\mathbf{f}_i(t), \tag{1.12}$$

where, $\mathbf{f}_i(t)$ has been assessed in the previous iteration; then the force $\mathbf{f}_i(t+\delta t)$ of each particle in the new position $\mathbf{r}_i(t + \delta t)$ is calculated; finally, with the newly calculated force, the other part of the velocity $\mathbf{v}_i(t + \delta t)$ is calculated and added to Eq. (1.12) to get the entire $\mathbf{v}_i(t + \delta t)$ through

$$\mathbf{v}_i(t + \delta t) = \mathbf{v}_i^{part}(t + \delta t) + \frac{\delta t}{2m_i}\mathbf{f}_i(t + \delta t). \tag{1.13}$$

One of the advantages of the "velocity Verlet" algorithm is that it improves the accuracy of the velocity calculation.

1.2 Quantum Mechanics Region

In this section, we will introduce the theorems we used to simulate the quantum region of the systems. We will cover the Born-Oppenheimer approximation, the basic idea of the density functional theory and the Kohn-Sham method and the dual-space plane-wave method we use in our simulation.

The Schrödinger equation in quantum mechanics is like the Newton's equations in classical mechanics. Suppose a system is composed of N electrons and M nuclei, where each nucleus has a positive charge $Z_\alpha e$ (α=1,2,...,M). The Schrödinger equation is

$$i\hbar\frac{\partial}{\partial t}\Psi = \hat{H}\Psi, \tag{1.14}$$

with $\Psi(\mathbf{x}_1, \mathbf{x}_2,...,\mathbf{x}_N; \mathbf{X}_1, \mathbf{X}_2,...,\mathbf{X}_M)$ being the wave function of the many-body system, and

$$\hat{H} = \sum_{\alpha=1}^{M}\left(-\frac{1}{2m_\alpha}\nabla_\alpha^2\right) + \sum_{\alpha<\beta}^{M}\frac{Z_\alpha Z_\beta}{r_{\alpha,\beta}} + \sum_{j=1}^{N}\left(-\frac{1}{2}\nabla_j^2\right) + \sum_{j<k}^{N}\frac{1}{r_{j,k}} + \sum_{j,\alpha}^{N,M}\left(-\frac{Z_\alpha}{r_{j,\alpha}}\right) \quad (1.15)$$

the Hamiltonian operator (atomic units used). m_α is the mass of the nucleus α, and r is the distance between two particles in the system. ($\hbar$=1, e^2=1, m_e=1)

1.2.1 Born-Oppenheimer Approximation

The computation of the energy and wave function of an average-size molecule is a formidable task. However, due to the high ratio of nuclear and electronic masses, the motion of the nuclei is much slower than the motion of electrons. The Born-Oppenheimer approximation says that in many cases, especially when we focus on the electronic structure of the material in its condensed (liquid/crystalline) states, the motion of nuclei can be separated adiabatically from the motion of electrons. After separation, the wave function becomes:

$$\Psi_{total} = \Psi_{electronic} \times \Psi_{nuclear}, \quad (1.16)$$

And the remaining time-independent Hamiltonian for the electrons is

$$\hat{H} = \sum_{j=1}^{N}\left(-\frac{1}{2}\nabla_j^2\right) + \sum_{j<k}^{N}\frac{1}{r_{j,k}} + \sum_{j}^{N} v(\mathbf{r}_j), \quad (1.17)$$

in which

$$v(\mathbf{r}_j) = -\sum_{\alpha}^{M}\frac{Z_\alpha}{r_{j,\alpha}}, \quad (1.18)$$

Here, $v(\mathbf{r}_j)$ is the external potential acting on electron j, or the potential due to nuclei of charge Z_α.

Hense, the Born-Oppenheimer(BO) approximation makes it possible to compute the wave function in two less formidable, consecutive steps. In the first step, the electronic Schrödinger equation is solved, yielding the wave function $\Psi_{electronic}$ depending

on electrons only. During this solution the nuclei are fixed in a certain configuration, very often the equilibrium configuration. The set of electronic energies thus computed becomes a function of the nuclear coordinates. In the second step this function serves as a potential on nuclei to obtain their movements.

1.2.2 Density Functional Theorem

Now, let's concentrate on $\Psi_{electronic}$, and we simplify it as Ψ. In most cases, we are concerned with time independent systems. For an isolated N-electron system, the time independent Schrödinger equation is:

$$\hat{H}\ \Psi = E\ \Psi, \tag{1.19}$$

E is the electronic energy, and

$$E[\Psi] = \frac{<\Psi \mid \hat{H} \mid \Psi>}{<\Psi \mid \Psi>} \tag{1.20}$$

1.2.2.1 Hohenberg-Kohn theorem

For an N-electron M-nuclei system, the nuclear distribution determines the external potential $v(\mathbf{r})$, which fixes the Hamiltonian. Together with the number of electrons N, it totally fix the electronic properties, or the ground state, for this system. In 1964, Hohengerg and Kohn proposed to use electronic density $n(\mathbf{r})$ in place of N and $v(\mathbf{r})$ as basic variable. It states: The external potential $v(\mathbf{r})$ is determined, within a trivial additive constant, by the electron density $n(\mathbf{r})$. Since $n(\mathbf{r})$ determines the number of electrons, it follows that $n(\mathbf{r})$ also determines the ground state wave function Ψ and all other electronic properties of the system. We will follow the book "Nanocatalysis" [60] closely for further clarification of the HK theorem.

The essence of the original basic theorem is that an exact representation of the ground state properties of a stationary, nonrelativistic, many-body system in terms of the ground state density alone is possible. The theorem ensures that the ground state can be calculated from a variational principle involving only the density, that

is, without having to solve the Schrödinger equation. For a given system, the exact ground state density and energy can be obtained via minimization of the energy expressed as a functional of the density. In a schematic way the gist of the HK theorem may be summarized as:

$$n(\mathbf{r}) \rightarrow \Psi(\mathbf{r}_1, ..., \mathbf{r}_N) \rightarrow v(\mathbf{r}). \tag{1.21}$$

To prove the HK theorem, let's first define two maps C and D in Equation 1.22 and 1.23 respectively.

$$C : v \rightarrow \Psi \tag{1.22}$$

$$D : \Psi \rightarrow N \tag{1.23}$$

Obviously, these two maps are injective (one to one) and thus, in light of the surjectivity of these maps, they are also bijective (that is, fully invertible). As a consequence of the unique inversion capability of the map D

$$D^{-1} : n(\mathbf{r}) \rightarrow |\Psi[n]\rangle \tag{1.24}$$

the HK theorem can be restated: the ground state expectation value of any observable $\hat{O}$ is a unique functional of the exact ground state density

$$\left\langle \Psi[n] \left| \hat{O} \right| \Psi[n] \right\rangle = O[n] \tag{1.25}$$

The full inverse map

$$CD^{-1} : n(\mathbf{r}) \rightarrow v(\mathbf{r}), \tag{1.26}$$

expresses the fact that knowledge of the ground state density determines the external potential of the system(to within a trivial constant) and thus, since the kinetic energy and the interpartical interaction are specified, the entire Hamiltonian.

Consider a system of inhomogeneous interacting electron gas under the influence

of external potential $v(\mathbf{r})$, with Hamiltonian $H = T + V + U$ (Equation (1.17)), and

$$T \equiv \frac{1}{2}\int \nabla\psi^*(\mathbf{r})\nabla\psi(\mathbf{r})d\mathbf{r} \tag{1.27}$$

$$V \equiv \int v(\mathbf{r})\psi^*(\mathbf{r})\psi(\mathbf{r})d\mathbf{r} \tag{1.28}$$

$$U = \frac{1}{2}\int \frac{1}{|\mathbf{r}-\mathbf{r}'|}\psi^*(\mathbf{r})\psi^*(\mathbf{r}')\psi(\mathbf{r}')\psi(\mathbf{r})d\mathbf{r}d\mathbf{r}', \tag{1.29}$$

where $\hat{T}$ is the kinetic energy, $\hat{U}$ is the interaction energy between electrons, and $\hat{V}$ is the potential energy of the electrons in an external field $v(\mathbf{r})$ (due to positively charged nuclei, for example). The HK theorem establishes also the variational character of the energy functional.

$$E_{v_0}[n] := \left\langle \Psi[n] \left| \hat{T} + \hat{U} + \hat{V}_0 \right| \Psi[n] \right\rangle, \tag{1.30}$$

where V_0 is the external potential of a specific system with ground state density $n_0(\mathbf{r})$ and ground state energy E_0. The states $|\Psi[n]\rangle$ are generated via D^{-1} from the elements of the set N. Due to the Rayleigh-Ritz variational principle $E_{v_0}[n]$ obeys the relations:

$$E_0 < E_{v_0}[n] \quad for \;\; n \neq n_0 \tag{1.31}$$

and

$$E_0 = E_{v_0}[n]\ . \tag{1.32}$$

Consequently, the exact ground state density can be determined by minimization of the functional $E_{v_0}[n_0]$. In summary,

$$E_0 = min\ E_{v_0}[n_0] \quad for \;\; n \subset N. \tag{1.33}$$

1.2.2.2 Kohn-Sham equation

Through Hohenberg-Kohn theorem, the N electron wave function Ψ, which depends on 3N variables, has been reduced to the density function $n(\mathbf{r})$, depending on 3 variables. However, it is still not an implementable scheme, in the sense that is does not

provide a guide for the explicit construction of the functionals in question. To date no exact functionals are known for any multiparticle system. In 1965, Kohn and Sham invented an ingenious indirect approach to the kinetic energy functional $T[n]$, which turned density functional theory into a practical tool for rigorous calculation. The ansatz used by KS replaces the interacting problem with and auxiliary independent particle one, with all the many-body effect included in an exchange correlation functional. In practice, the KS scheme introduces an equivalent orbital picture (rigorously established), with the resulting KS equations solved self consistently.

Let's first return to the HK definition of Hamiltonian, and define

$$F[n(\mathbf{r})] \equiv (\Psi, (T+U)\Psi) \tag{1.34}$$

Now, the energy functional

$$E_v[n] \equiv (\Psi, H\Psi) = \int v(\mathbf{r})n(\mathbf{r})d\mathbf{r} + F[n] \tag{1.35}$$

equals the ground-state energy for the correct $n(\mathbf{r})$, and has a minimum, given that the number of particles of the system $N[n] \equiv \int n(\mathbf{r})d\mathbf{r}$ is kept constant.

In analogy with above, Kohn and Sham invoked a corresponding noninteracting reference system, with the Hamiltonian:

$$T_s[n] = \sum_i^N \left\langle \psi_i \left| -\frac{1}{2}\nabla_i^2 \right| \psi_i \right\rangle \tag{1.36}$$

and

$$n(\mathbf{r}) = \sum_i^N \sum_s |\psi_i(\mathbf{r}, s)|^2 \tag{1.37}$$

in which there are no electron-electron repulsion terms, and the ground state density is exactly as before. However, the definition of kinetic energy $T_s[n]$, is not exactly as the kinetic energy functional $T[n]$. Nevertheless, if we define

$$F[n] = T_s[n] + J[n] + E_{xc}[n], \tag{1.38}$$

where $J[n]$ is the purely classical electron-electron repulsion energy:

$$J[n] = \frac{1}{2}\int\int \frac{1}{r_{12}} n(\mathbf{r}_1)n(\mathbf{r}_2)d\mathbf{r}_1 d\mathbf{r}_2, \tag{1.39}$$

Compared with what's in the HK Hamiltonian:

$$F[n] = T[n] + U[n] \tag{1.40}$$

We know

$$E_{xc} \equiv T[n] - T_s[n] + U[n] - J[n] \tag{1.41}$$

From the definition, the $E_{xc}(n)$ term, which we call exchange-correlation energy, contains the difference between T and T_s, presumably very small, and the nonclassical part of electron repulsion. Now the energy functional can be rewritten as:

$$\begin{aligned} E[n] &= T_s[n] + J[n] + E_{xc}[n] + \int v(\mathbf{r})n(\mathbf{r})d\mathbf{r} \\ &= \sum_i^N \sum_s \int \psi_i^*(\mathbf{r})(-\frac{1}{2}\nabla^2)\psi_i(\mathbf{r})d\mathbf{r} + J[n] + E_{xc}[n] + \int v(\mathbf{r})n(\mathbf{r})d\mathbf{r} \end{aligned} \tag{1.42}$$

while

$$n(\mathbf{r}) = \sum_i^N \sum_s |\psi_i(\mathbf{r}, s)|^2 \tag{1.43}$$

As mentioned before, Kohn and Sham built this theorem on the basis of non-interacting reference as in Equation (1.36) and Equation (1.37), which indicates the orthogonality of the orbital:

$$\int \psi_i^*(\mathbf{r})\psi_j(\mathbf{r})d\mathbf{r} = \delta_{ij} \tag{1.44}$$

Therefore, if we define the effective KS potential as:

$$\begin{aligned} v_{eff}(\mathbf{r}) &= v(\mathbf{r}) + \frac{\delta J[n]}{\delta n(\mathbf{r})} + \frac{\delta E_{xc}[n]}{\delta n(\mathbf{r})} \\ &= v(\mathbf{r}) + \int \frac{n(\mathbf{r}')}{|\mathbf{r} - \mathbf{r}'|} d\mathbf{r}' + v_{xc}\mathbf{r} \end{aligned} \tag{1.45}$$

with

$$v_{xc}(\mathbf{r}) = \frac{\delta E_{xc}[n]}{\delta n(\mathbf{r})} \tag{1.46}$$

Then, to a system of N non-interacting electrons, we have

$$\left\{-\frac{1}{2}\nabla^2 + v^{eff}(\mathbf{r})\right\}\psi_i(\mathbf{r}) = \epsilon_i\psi_i(\mathbf{r}), \tag{1.47}$$

while

$$n(\mathbf{r}) = \sum_i^N \sum_s |\psi_i(\mathbf{r}, s)|^2 \tag{1.48}$$

Equation (1.45) to (1.48)are the famous Kohn-Sham equations. Notice that v_{eff} depends on density $n(\mathbf{r})$, and then produces a set of ψ_i, which lead to a new density $n(\mathbf{r})$. Hence, this equations must be solved self consistently. We start from a trial density $n^{in}(\mathbf{r})$, solves the KS equations to obtain the eigenvalues ϵ_i and eigen states $\psi_i(\mathbf{r})$, which results in a new density $n^{out}(\mathbf{r})$. Through a proper mixing procedure, a new input density is constructed, and the process is repeated until self-consistency is achieved.

After we obtain a self consistent solution, we have

$$\sum_i^N \epsilon_i = \sum_i^N \left\langle \psi_i \left| -\frac{1}{2}\nabla^2 + v_{eff}(\mathbf{r}) \right| \psi_i \right\rangle \tag{1.49}$$

$$= T_s[n] + \int v_{eff} n(\mathbf{r}) d\mathbf{r} \tag{1.50}$$

Together with the total energy functional Equation (1.42) and the definition of v_{eff}, the total energy can be expressed as

$$E = \sum_{i=1}^N \epsilon_i - \frac{1}{2}\int\int \frac{n(\mathbf{r})n(\mathbf{r}')}{|\mathbf{r}-\mathbf{r}'|} d\mathbf{r}d\mathbf{r}' + E_{xc}[n] - \int v_{xc}(\mathbf{r})n(\mathbf{r})d\mathbf{r} \tag{1.51}$$

1.2.2.3 Approximations to E_{xc}: LDA method and GGA method

Through the introduction of KS equations, we are able to treat N orbital independently. The price to pay for is the precision in the calculation. The most disturbing term in the KS equations is the exchange correlation energy. The search for an accurate E_{xc} has encountered tremendous difficulty and continues to be the greatest challenge in the density functional theory. In this section, we will intoduce two different

approximations to estimate E_{xc}. The first method is called the Local Density Approximation(LDA). Assuming that the exchange correlation energy for a nonuniform system can be obtained by applying uniform electron gas multiplication to infinitesimal portions of the nonuniform electron distribution, then

$$E_{xc}^{LDA}[n] = \int n(\mathbf{r})\epsilon_{xc}[n]d\mathbf{r} \tag{1.52}$$

where $\epsilon_{xc}(n)$ represents the exchange and correlation energy per particle of a uniform electron gas of density n. The corresponding exchange correlation potential becomes

$$v_{xc}^{LDA}(\mathbf{r}) = \frac{\delta E_{xc}^{LDA}}{\delta n(\mathbf{r})} = \epsilon[n(\mathbf{r})] + n(\mathbf{r})\frac{\partial \epsilon_{xc}[n]}{\partial n} \tag{1.53}$$

The function $\epsilon_{xc}[n]$ can be further divided into the exchange and the correlation terms as

$$\epsilon_{xc}[n] = \epsilon_x[n] + \epsilon_c[n], \tag{1.54}$$

From the Dirac exchange energy functional, the exchange term is given as

$$\epsilon_x[n] = -\frac{3}{4}\left(\frac{3}{\pi}\right)^{1/3} n^{1/3}, \tag{1.55}$$

As to the correlation term, quantum Monte Carlo calculations of Ceperley and Alder [9] have provided accurate values for ϵ_c. These values has also been interpolated to an analytic form by Vosko, Wilk and Nusair in 1980 [51].

The major source of error in the LDA method comes from exchange energy. In 1965, Perdew proposed a model by imposing the conditions for the correct exchange hole on the approximate hole given by the gradient expansion. This model leaves only 1% error in the exchange energy and is further simplified in 1986 [21] and to the so-called generalized gradient approximation(GGA). A In this method, E_{xc} is a functional of the local electron density and its gradient. Namely,

$$E_{xc} = E_{xc}[n; \nabla n], \tag{1.56}$$

In practice,

$$E_x^{GGA}[n] = -\frac{3}{4}(\frac{3}{\pi})^{1/3}\int n^{4/3}F(s)d\mathbf{r} \tag{1.57}$$

with

$$s = \frac{|\nabla n(\mathbf{r})|}{(2k_F n)} \tag{1.58}$$

$$k_F = (3\pi^2 n)^{1/3} \tag{1.59}$$

and

$$F(s) = (1 + 1.296s^2 + 14s^4 + 0.2s^6)^{1/15} \tag{1.60}$$

There are many other effective forms for exchange and correlation energy, and we expect to see more accurate approximations to be developed in the future. In our simulation, we will employ the GGA method.

1.2.3 Dual Space Plane-wave Method for Finite Systems

In the previous section, we introduce the Kohn-Sham theorem and briefly describe how to solve the Kohn-Sham equation using self-consistently method. In this section, we discuss in detail our use of the dual-space(both real- and momentum-space) plane-wave method in the calculation of the ground state of the electronic energy of a finite system. [7].

1.2.3.1 Plane-wave expansion of the wave functions

Let's define a calculational cell to be the region of space given by

$$\mathbf{r} \equiv (x, y, z); 0 \leq x \leq L_x, 0 \leq y \leq L_y, 0 \leq z \leq L_z. \tag{1.61}$$

The wave function $\psi_{j\sigma}(\mathbf{r}) = \langle \mathbf{r}|j\sigma\rangle$ is expanded in a plane-wave basis within the cell, i.e.,

$$\psi_{j\sigma}(\mathbf{r}) = \Omega^{-1/2}\sum_g \tilde{\phi}_{j\sigma}(\mathbf{g})e^{i\mathbf{g}\cdot\mathbf{r}} \tag{1.62}$$

for $\mathbf{r}$ in the cell, and

$$\psi_{j\sigma}(\mathbf{r}) = 0 \tag{1.63}$$

for **r** outside the cell.

In Equation 1.62 Ω is the volume of the cell, $\Omega = L_x L_y L_z$, and $\tilde{phi}_{i\sigma}(\mathbf{g})$ are the coefficients of the plane-wave expansion. The reciprocal-space(g-space) grid is defined by

$$\mathbf{g} = 2\pi(k_x/L_x, k_y/L_y, k_z/L_z), \tag{1.64}$$

where $k_\alpha(\alpha = x, y, z)$ are integers satisfying

$$-N_\alpha/2 \leq k_\alpha \leq N_\alpha/2. \tag{1.65}$$

The sum over **g** in 1.62 includes all combinations of (k_x, k_y, k_z) satisfying Equation 1.65. We note that while the wave function is defined to be zero outside the cell, its amplitude $\psi_{j\sigma}(\mathbf{r})$ and gradient $\nabla\psi_{j\sigma}(\mathbf{r})$ are required to vanish (or be negligibly small) on the boundary of the cell. For a finite system this condition can be satisfied by increasing the dimensions of the calculational cell $\{L_\alpha\}$ and/or by translating and rotating the system inside the cell. the L_α need no t be equal(i.e., the cell need not be a cube). In most circumstances we choose the lengths $\{L_\alpha\}$ and the integers $\{N_\alpha\}$ such that $N_x/L_x = N_y/L_y = N_z/L_z = g_{max}/\pi$ and impose a spherical momentum cutoff, that is,

$$\tilde{\phi}_{j\sigma}(\mathbf{g}) = 0 \quad for \;\; |\mathbf{g}| > g_{max}. \tag{1.66}$$

The choice of the momentum cutoff g_{max} is dictated primarily by the nature of the ionic pseudopotentials while the lengths $\{L_\alpha\}$ are determined by the physical size and geometry of the system. Together these determine the number of plane waves $N = N_x N_y N_z$.

Since we are dealing with eigenfunctions of a finite nonperiodic system, we can require, without loss of generality, that the wave functions be real in real space, i.e.,

$$\psi_{j\sigma}(\mathbf{r}) = \psi^*_{j\sigma}(\mathbf{r}) \;\; and \;\; \tilde{\phi}_{j\sigma}(\mathbf{g}) = \tilde{\phi}^*_{j\sigma}(-\mathbf{g}). \tag{1.67}$$

Orthonormality of the wave functions gives

$$\langle j\sigma|j'\sigma\rangle = \sum_g \tilde{\phi}_{j\sigma}(-\mathbf{g})\tilde{\phi}_{j'\sigma}(-\mathbf{g}) = \delta_{jj'} \ . \tag{1.68}$$

In the dual-space method, the gradient operator is diagonal in the plane-wave basis,

$$\nabla\psi_{j\sigma}(\mathbf{r}) = \Omega^{-1/2}\sum_g i\mathbf{g}\tilde{\phi}_{j\sigma}(\mathbf{g})e^{i\mathbf{g}\cdot\mathbf{r}}, \tag{1.69}$$

and

$$\left\langle j\sigma \left| -\frac{1}{2}\nabla^2 \right| j'\sigma \right\rangle = \frac{1}{2}\sum_g g^2\tilde{\phi}_{j\sigma}(-\mathbf{g})\tilde{\phi}_{j'\sigma}(\mathbf{g}) \ . \tag{1.70}$$

1.2.3.2 Plane-wave expansion of the density and the real-space grid

The density $n_\sigma(\mathbf{r})$ can also be expanded in a Fourier series but requires a momentum cutoff which is twice as large as that of the wave f unctions. This expansion is useful in evaluating the gradient corrections to the LSD, and in motivation our treatment of the potential operators in real space. Thus, we write

$$n_\sigma(\mathbf{r}) = \Omega^{-1}\sum_g\sum_{g'}[\sum_j f_{j\sigma}\tilde{\phi}_{j\sigma}(-\mathbf{g})p\tilde{h}i_{j\sigma}(\mathbf{g}')]e^{i(\mathbf{g}-\mathbf{g}')\cdot\mathbf{r}} \tag{1.71}$$

$$= \Omega^{-1}\sum_G \tilde{D}_\sigma(\mathbf{G})e^{i\mathbf{G}\cdot\mathbf{r}} \ . \tag{1.72}$$

The "G-space" grid in Equation 1.71 is defined as

$$\mathbf{G} = 2\pi(m_x/L_x, m_y/L_y, m_z/L_z), \tag{1.73}$$

where $m_\alpha(\alpha = x, y, z)$ are integers satisfying

$$-M_\alpha/2 \leq m_\alpha \leq M_\alpha/2 \ \ and \ M_\alpha = 2N_\alpha \ . \tag{1.74}$$

Now the gradient, $\nabla n_\sigma(\mathbf{r})$, which is needed for evaluation of the exchange correlation gradient corrections, is given by

$$\nabla n_\sigma(\mathbf{r}) = \Omega^{-1}\sum_G i\mathbf{G}\tilde{D}_\sigma(\mathbf{G})e^{i\mathbf{G}\cdot\mathbf{r}} \ . \tag{1.75}$$

The coeffients $\tilde{D}_\sigma(\mathbf{G})$ can be evaluated directly from the wave function coefficients $\{\tilde{\phi}_{j\sigma}\}$(see Equation 1.71). A more efficient method is to evaluate $n_\sigma(\mathbf{r})$ on a real-space grid which is the dual of the G-space grid, and use a discrete Fourier transform, i.e., FFT to get $\tilde{D}_\sigma(\mathbf{G})$. We define the real-space grid, the "S grid", as

$$\mathbf{S} = (i_x L_x/M_x, i_y L_y/M_y, i_z L_z/M_z), \tag{1.76}$$

where i_α are integers satisfying $0 \leq i_\alpha \leq M_\alpha - 1$. The density on the S grid is defined as

$$D_\sigma(\mathbf{S}) = (\Omega/M) n_\sigma(\mathbf{S}), \tag{1.77}$$

where $M = M_x M_y M_z$ is the number of real-space grid points, and the set $[D_\sigma(\mathbf{S})]$ is the "FFT dual" of $[\tilde{D}_\sigma(\mathbf{G})]$,

$$\tilde{D}_\sigma(\mathbf{G}) = M^{-1/2} \sum_S D_\sigma(\mathbf{S}) e^{-i\mathbf{G}\cdot\mathbf{S}} \; . \tag{1.78}$$

In order to obtain $\{D_\sigma(\mathbf{S})\}$ we define the wave function on the S grid

$$\phi_{j\sigma}(\mathbf{S}) = (\Omega/M)^{1/2} \psi_{j\sigma}(\mathbf{S}) \tag{1.79}$$

or, in terms of plane-wave coefficients,

$$\phi_{j\sigma}(\mathbf{S}) = M^{-1/2} \sum_g \tilde{\phi}_{j\sigma}(\mathbf{g}) e^{i\mathbf{g}\cdot\mathbf{S}} \; , \tag{1.80}$$

where the coefficients $D_\sigma(\mathbf{S})$ are given by

$$D_\sigma(\mathbf{S}) = \sum_j f_{j\sigma} |\phi_{i\sigma}(\mathbf{S})|^2 \; . \tag{1.81}$$

We note here that the wave function on the S grid, $\{\phi_{j\sigma}(\mathbf{S})\}$ in Equation 1.80, is not the FFT dual of the plane-wave coefficients, $\{\tilde{\phi}_{j\sigma}(\mathbf{g})\}$. There are several methods for obtaining $\{\phi_{j\sigma}(\mathbf{S})\}$ from $\{\tilde{\phi}_{j\sigma}(\mathbf{g})\}$ using standard FFT routines.

1.2.4 Pseudopotential

This section will introduce briefly the definition of pseudopotentials and then explain in detail the techniques we used to estimate the electron-ion interaction via separable nonlocal psedopotentials in conjunction with the dual-space plane wave method.

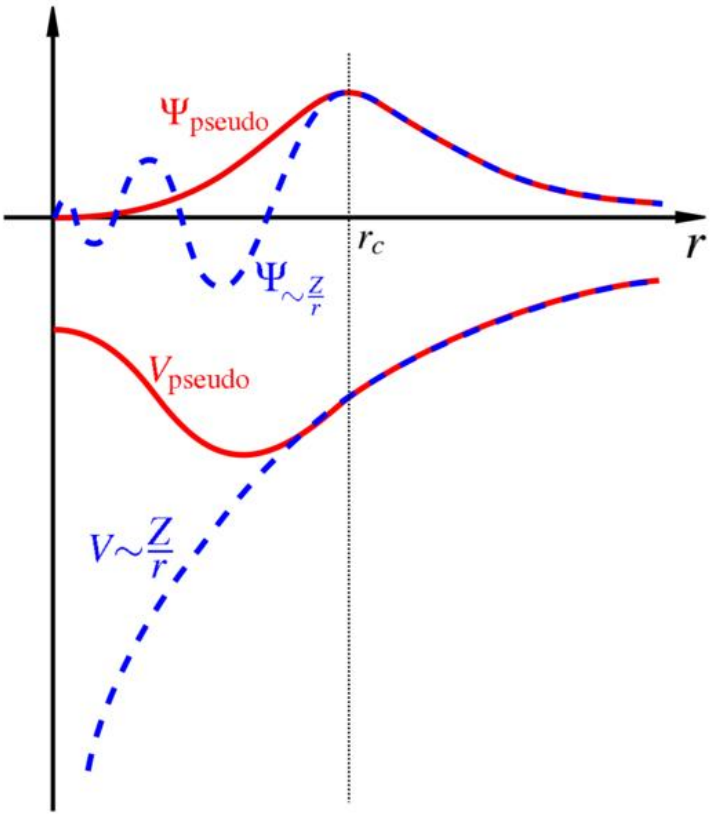

Figure 2: Comparison of a wave function in the Coulomb potential of the nucleus (blue) to the one in the pseudopotential (red). The real and the pseudo wave function and potentials match above a certain cutoff radius r_c.

1.2.4.1 General ideas about pseudopotentials

A pseudopotential is constructed to replace the atomic all-electron potential so that the complicated effects from the motion of the core (i.e. non-valence) electrons of an atom and its nucleus will be eliminated and the valence electrons are described by nodeless pseudo wave functions [33]. (See Fig. 2). In this approach only the chemically active valence electrons are dealt with explicitly, while the core electrons are 'frozen', or considered together with the nuclei as rigid non-polarizable ion cores. The principal objectives to consider are (i) the transferability of the pseudopotentials, its ability to accurately describe the valence electrons in different environments. (ii) Their efficiency, that is, to keep the computational workload in applications as low as possible, allowing to compute wave functions and electron densities with as few basis

functions and operations as possible.

In general, Pseodopotentials can be categorized into two classes: norm-conserving and ultra-soft. Norm-conserving pseudopotentials are derived from an atomic reference state, requiring that the pseudo and the all-electron valence eigenstates have the same (reference) energies and the same amplitude (and thus density) outside a chosen core cutoff radius r_c. Pseudopotentials with larger cutoff radius are said to be "softer", but the norm-conserving constraint leaves little room for any significant improvement. The ultra-soft pseudopotential is formed by a summation of a few separable terms, which becomes local and vanishes outside the core. The scattering properties and their energy derivatives are constructed to be correct at several energies spanning the range of occupied states. In our simulation, we used the separable nonlocal pseodopotential proposed by Troullier-Martins [39] in 1991.

1.2.4.2 Separable nonlocal pseudopotentials

The electron-ion interaction treated via separable nonlocal pseudopotential can be written as:

$$E_{eI} = \sum_{j\sigma} f_{j\sigma} \sum_{I} \left\langle j\sigma \left| \tilde{V}_I \right| j\sigma \right\rangle, \tag{1.82}$$

where in real space

$$V_I(\mathbf{r}_I; \mathbf{r}, \mathbf{r}') = V_I^{lc}(|\mathbf{r} - \mathbf{r}_I|)\delta(\mathbf{r} - \mathbf{r}') + V_I^{nlc}(\mathbf{r} - \mathbf{r}_I, \mathbf{r}' - \mathbf{r}_I). \tag{1.83}$$

and $\{f_{j\sigma}\}$ are the occupation numbers.

The nonlocal term (for an ion at the origin) is obtained from a semilocal pseudopotential via the Kleinman-Bylander prescription [24]:

$$V_I^{nlc}(\mathbf{r}, \mathbf{r}') = \sum_{l,m} F_l^I K_{lm}^I(\mathbf{r}) K_{lm}^I(\mathbf{r}'), \tag{1.84}$$

where

$$K_{lm}^I(\mathbf{r}) = \triangle V_l^I(\mathbf{r}) R_l^I(r) Y_{lm}(\hat{r}), \tag{1.85}$$

and

$$F_l^I = \left[\int_0^\infty dr[rR_l^I(r)]^2 \triangle V_l^I(r)\right]^{-1} \tag{1.86}$$

where $\triangle V_l^I(r)$ and $R_l^I(r)$ are the semilocal pseudopotential and radial pseudowave function, respectively.

To evaluate those separable nonlocal pseudopotentials, an integral involving the wave function can be done most efficiently in real space since the semilocal pseudopotential $\triangle V_l^I(r) = 0$ for $r > r_c$, and thus the integral in real space need not be over all space. Define

$$B_{lm}^I(\mathbf{S}) = \sum_G \int_0^{L_x} dx \int_0^{L_y} dy \int_0^{L_z} dz K_{lm}^I(\mathbf{r}, \mathbf{r}_I) e^{i\mathbf{G}\cdot(\mathbf{S}-\mathbf{r})}, \tag{1.87}$$

then without approximation

$$\sum_S B_{lm}^I(\mathbf{S})\phi_{j\sigma}(\mathbf{S}) = \int d^3r K_{lm}^I(\mathbf{r}-\mathbf{r}_I)\psi_{j\sigma}(\mathbf{r}). \tag{1.88}$$

We now make the approximation

$$B_{lm}^I(\mathbf{S}) \cong K_{lm}^I(\mathbf{S}-\mathbf{r}_I). \tag{1.89}$$

In principle, the sum in Equation (1.88) could be performed on a real space grid which is the dual of the reciprocal space g grid; however, since we have already made use of the wave functions represented on the S grid, $\{\phi_{j\sigma}(\mathbf{S})\}$ in the evaluation of the local terms, we use the S grid here as well.

1.3 QM/MM Interface

The interaction between the QM region and the MM region, $V_{QM/MM}$, is the heart of a hybrid QM/MM method. We will introduce our treatment of it briefly here.

In general, the interaction can be split into two terms:

$$V_{QM/MM} = V_{QM/MM}^{NB} + V_{QM/MM}^{B}, \tag{1.90}$$

representing the non-bonded($V^{NB}_{QM/MM}$) and the bonded($V^{B}_{QM/MM}$) interactions. These two terms distinguish between the interactions of the QM region with MM atoms which are separated by more than one molecular bond(non-bonded) or that are directly linked through a molecular bond(bonded). Bonded interactions is often used for QM/MM treatment of large biological molecules that the active region includes only a limited portion of a large macromolecule. In this case, the transition between the QM and MM regions occurs across molecular bonds, where the interaction includes bond stretching, bond bending and internal rotation (Fig. 3). The description for bonded

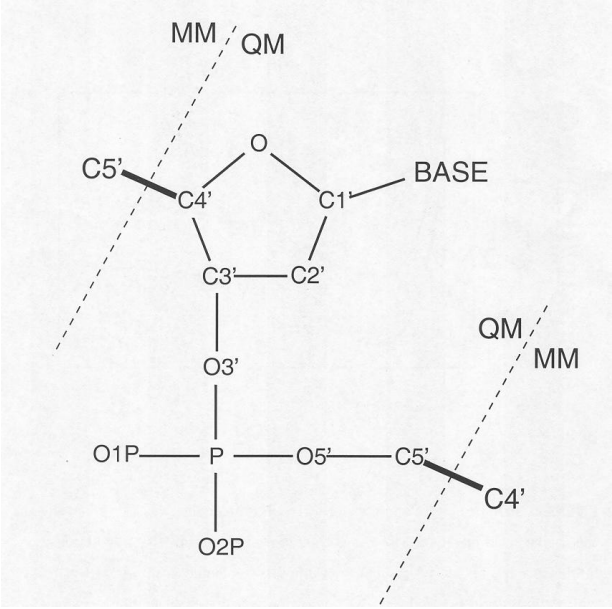

Figure 3: Schematic illustration of the QMMM partition of a DNA strand. The QM region contains a single nucleobase with its corresponding sugar and phosphate group. The connections between the QM part with the MM region occurs through the linking atoms $C5\prime$ and $C4\prime$, on the $5\prime$ and $3\prime$ side, respectively. The QMMM interfacial $C4\prime$ - $C5\prime$ bonds are highlighted by using thick black sticks bisected by dashed lines.

interaction can get very complicated. However, for our water cluster systems, which solely consists of small water molecules, we only need non-bonded interaction, and we will focus on it in the following context. Non-bonded MM atoms interact with the QM region through Coulomb force, Pauli repulsion and van der Waals interactions.

In particular, we have:

$$V^{NB}_{QM/MM} = \sum_{I \in MM} [\int d\mathbf{r}\ \rho_{QM}(\mathbf{r})\ V_I^{Coul.}(\mathbf{r})\ +\ \sum_{J \in QM} V_{LJ}(r_{IJ})], \tag{1.91}$$

where ρ_{QM} is the QM charge density including both the electronic and ionic contributions, $V_I^{Coul.}$ is the electrostatic potential generated by the MM partial charge, and V_{LJ} is a Lennard-Jones potential. This latter term describes the Pauli repulsion and the van der Waals attraction between the MM and QM atoms and is calculated by employing the parameters provided by the Amber force field[53, 64]. Atoms in the MM region carry partial charges. Within a MM scheme, these point-like charges model the redistribution of the electronic charge upon formation of the bonding network. In a QM scheme based on plane-waves, the Coulomb interaction of a bare point-like charge with the QM region can give rise to the detrimental "spill-out effects".[32, 3] To avoid these spurious effects, the electrostatic interaction between the QM and MM regions is usually treated through the smearing of the MM partial charges according to a parametrized distribution function.[32, 3] In our QM/MM scheme we employ a gaussian distribution. Thus, the electrostatic potential generated by a MM partial charge Q_I corresponds to:

$$V_I^{Coul.}(\mathbf{r}) = \frac{Q_I}{r}\ erf(\frac{r}{\sqrt{2}\sigma}), \tag{1.92}$$

To determine the width of the gaussian distribution, σ, associated with each charged MM atoms, we carried out first-principles calculations on charged atoms, using our QM program.[**?**] These calculations show that for each atomic species the gaussian width is related to the amount of excess charge. In particular, we find that σ depends linearly on the excess charge (See Fig. 4). Hence, in our QM/MM scheme we use the linear relations derived form first-principles calculations to assign σ to each charged MM atoms.

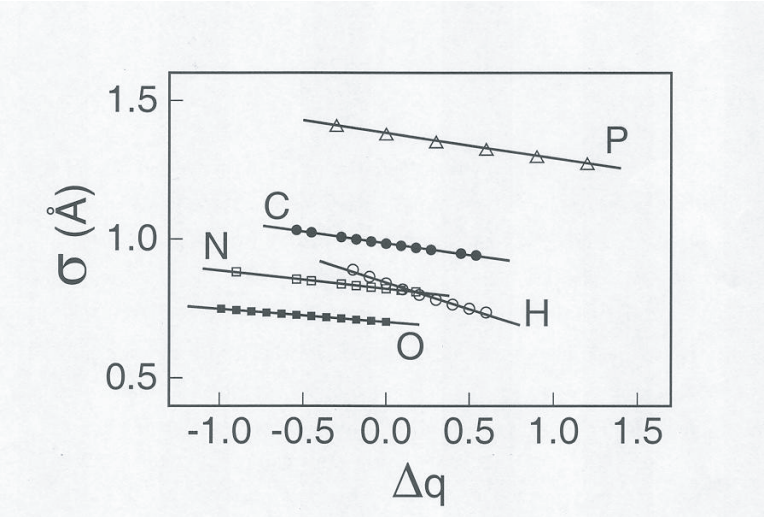

Figure 4: The width (σ in $\mathring{A}$) of the gaussian distributions which best-fit the spatial distributions of the excess electronic charge densities ($\triangle$q, in electron charge units) associate with H, C, N, O, and P atoms. Symbols refer to the width derived by fitting first-principle results. For each species, the width depends linearly on the excess charge solid lines.

CHAPTER II

QM/MM INVESTIGATION OF EXCESS ELECTRON IN WATER CLUSTERS

2.1 Introduction

The hydrated electron is a ubiquitous species in aqueous solution and has important implications for various processes such as charge transfer, chemical reactivity, and radiation chemistry. Therefore, a molecular level understanding of electrons solvation, knowledge of which is fundamental to the understanding of basic solute-solvent phenomena, has emerged as one of the outstanding problems in contemporary chemical physics. However, the satisfactory characterization of excess electron has proven to be a difficult task. Early theoretical work [46, 44, 45] predicted formation of surface states of the excess electron for small water clusters ($(H_2O)_n^-$) for $n \leq 30$) with a gradual transition to interior localized states of the excess electron for clusters with $n \geq 60$ water molecules. These predictions were made on the basis of simulations which involved a single electron moving in a potential specifically constructed to describe the effective interaction of a water molecules with an electron [44]. The intermolecular interaction between water molecules was described through the use of a classical interaction potential. Recently there has been a surge of activity on this subject, with experiments on large water cluster anions [22] providing evidence that indeed, the excess electron observed previously in water cluster anions with higher vertical binding energies was internally solvated, as predicted by afore-mentioned early theory. On the other hand, for smaller water clusters the vertical binding energies are lower, correlating with the predicted surface states of the excess electron.

This conclusions were challenged by a most recent theoretical work, [26], where as in the earlier simulations the single-electron Schrodinger equation was solved for an excess electron interacting with the water molecules of the cluster through a (modified) interaction potential. The authors of this theoretical investigation concluded that in all experimental studies published till now, the state of the excess electron may be assigned as a surface-bound electronic state (even for clusters with $n \geq 200$ water molecules). This conclusion was questioned by th authors of Ref.[22]. In light of the above we have embarked on a comprehensive investigation of the states of excess electrons in water clusters of variable size. Unlike the early simulations [46, 44, 45] and the most recent one [26], where only a single electron was treated quantum mechanically while all the water molecules were described classically, our investigation utilizes the newly developed QM/MM method. In the calculations, the excess electron and part of the water cluster are described quantum mechanically, while only part of the water cluster is treated classically. We use the TIP3P model for the description of MM water molecules, while in the quantum region, we include 8 valence electrons per H_2O molecule interacting with the oxygen and hydrogen cores via norm-conserving pseudo potentials [39]. The QM calculations used the Born-Oppenheimer spin-density functional method [7], with generalized gradient corrections(GGA) after Ref.[20]. A plane-wave basis with a cutoff energy of 62 Ry was used. The following content in this chapter will be devoted to the details and results of this calculation.

2.2 Computational Details

In this section, we will explain some technical specifics utilized in our simulation.

2.2.1 Construction of Initial Cluster Geometries

Conducting QM/MM calculation with water molecules and the excess electron randomly placed will be very time-consuming to reach a stable state, instead, we would

like to choose a starting point for QM/MM calculation with reasonable cluster geometries. Therefore, we first start classical simulation with a water cluster containing a Cl^- anion. The Cl^- anion either occupies an internal cavity which creates an interior state water anion, or localizes on the surface, corresponding to surface state water anion. Such cluster is generated randomly with the radius occupied by the Cl^- about $2.65\mathring{A}$ (See Fig. 5(a)). The cluster is then classically relaxed at certain temperature until it reaches equilibration (Fig. 5(b)). A configuration with minimum energy is identified at this point and some water molecules(mostly around 20) nearest to the Cl^- are selected to be treated quantum mechanically (Fig. 5(c)). Next, the Cl^- is removed and replaced by an excess electron, leading to the QM/MM simulation for this water anion (Fig. 5(d)). The purpose of the Cl^- in the classical relaxation part of simulation is to create a negatively charged cluster with a cavity (or pocket) to hold the excess electron, which is very similar to a water anion with an excess electron. We choose Cl^- because its size is comparable to the size of solvated electron.

2.2.2 QM/MM Simulation

QM/MM scheme is applied to the water anion created from the process discussed above. Using dynamic evolution the water cluster is equilibrated at high temperature for a duration of 1 to 2 ps to encourage maximum interaction and movement. Subsequently the system is cooled gradually and equilibrated at lower temperature(preferably room temperature). This is called the annealing process. See Fig. 6 for an annealing process of $(H_2O)^-_{16}$ process.

As the cluster reaches equilibrium, the localization mode and other physical properties of the excess electron could be observed through its density distribution. The vertical detachment energy(VDE), defined as the energy needed to remove the excess electron from the cluster without rearrangement of atoms, is obtained as the difference between the total energy of the cluster anion and the total energy of the neutral

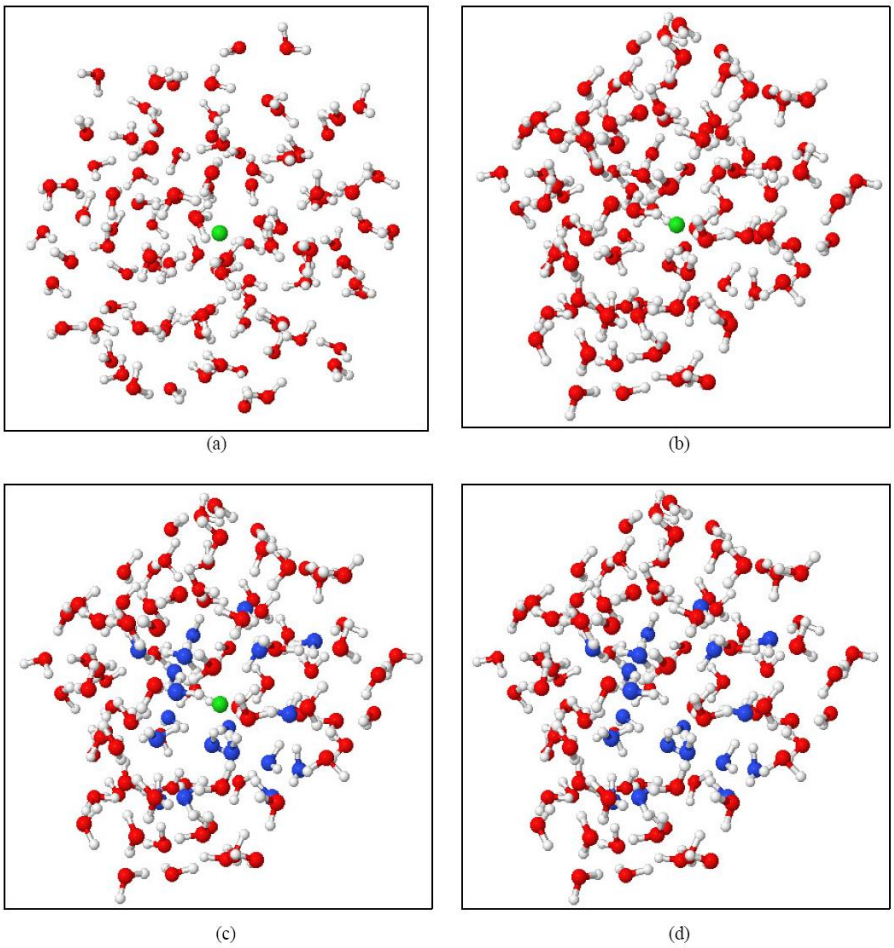

Figure 5: Preparing $(H_2O)^-_{100}$ cluster for QM/MM simulation. (a)Creating a $(H_2O)_{100}Cl^-$ cluster randomly with the Cl^- in the middle. The Cl^- is represented by the green dot in the picture. (b)After classical relaxation, the $(H_2O)_{100}Cl^-$ has a local minimum energy configuration. (c)19 water molecules nearest to the chlorine are selected as quantum water molecules, with their oxygens colored in blue. (d)The chlorine is removed and replaced by an excess electron.

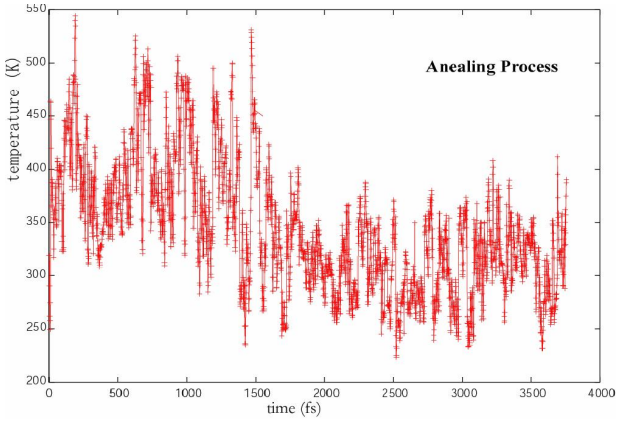

Figure 6: Annealing process of an $(H_2O)_{16}^-$ cluster. The cluster is equilibrated at high temperature 400 K for a duration of 1.5 ps, and then gradually cooled down to 300 K.

cluster with the same nuclear geometry as the water anion. We also collect the size of the localized excess electron charge distribution, calculated as the radius of gyration of the electron distribution associated with the highest occupied Kohn-Sham orbital, and study the relationship between the VDE and the gyration radius. A key point to guarantee accuracy in this QM/MM simulation is that the water molecules treated quantum mechanically should be in the active QM region, which in our case means they should be in the shell of water molecules surrounding the excess electron. Although we identify water molecules closest to the excess electron as quantum water molecules in the beginning of QM/MM simultaion, as the system evolves, some water molecules might move from QM region to MM region, and vice versa. Our strategy towards this problem is to pinpoint the position of the excess electron as the centroid of its density distribution, track the relative distance between every molecule with the excess electron, and determine whether it should be treated classically or quantum mechanically along the trajectory.

2.3 Results of Various Water Anions

2.3.1 $(H_2O)_{16}^-$ surface state

For such a small cluster, we are capable of applying fully QM calculation to it. The $(H_2O)_{16}Cl^-$ was generated with the Cl^- inside the cluster. However, after classical relaxation, the Cl^- moves to the surface (See Fig. 7). We replace the Cl^- with an excess electron at this point and start QM simulation.

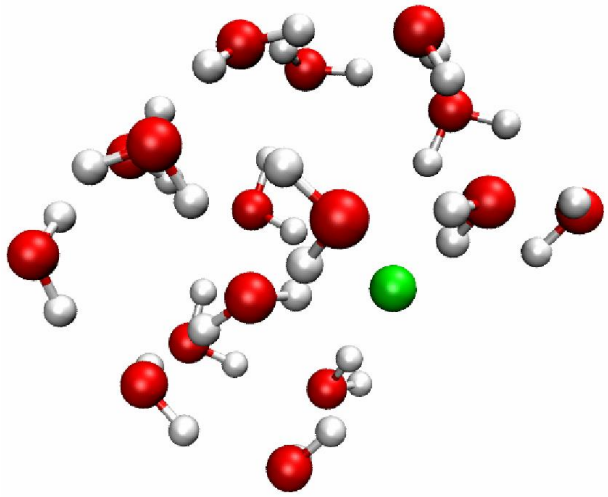

Figure 7: The lowest energy configuration of $H_2O_{16}(Cl)^-$ from MM relaxation. It's also the starting configuration of QM calculation. The green point represents the position of the Cl^- in the former case, and the center of the excess electron distribution in the latter.

After QM simulation, we can see from Fig. 8 that the excess electron remains on the surface of the cluster, which classifies the cluster to a surface state cluster. The distribution of the excess electron looks like a pocket, and the size of it is around 7 $\mathring{A}$, comparable to the size of the whole cluster 9$\mathring{A}$. We also plot the eigenvalues of energy level around the highest occupied Kohn-Shan orbital in Fig. 9(a) and the gyration radius of the excess electron in Fig. 9(b) along the equilibrium trajectory. The pink curve in Fig. 9(a) characterize the energy eigenvalue of the highest occupied Kohn-Shan orbital, and that is the energy level at which the excess electron stays. As you can see, its value fluctuates around 0 eV, indicating the excess electron is

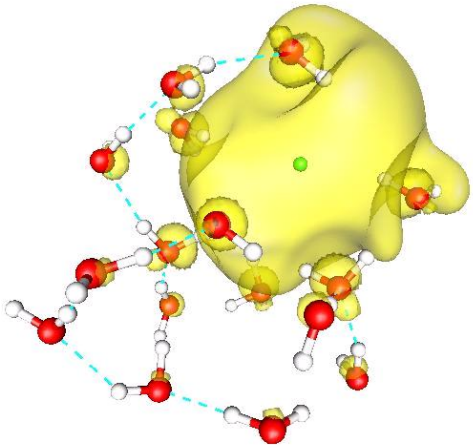

Figure 8: Configuration of $(H_2O)_{16}^-$ at 300 K in equilibrium. The yellow contour is the equi-density surface which encompassing more than 50% of the excess electron density corresponding to the highest occupied Kohn-Shan orbital. The green dot represents the centroid of the excess electron distribution. The blue dash lines indicate the hydrogen bonds between oxygen and hydrogen.

very loosely bounded to the cluster. And this energy level is quite separated from both other occupied energy levels and all the unoccupied energy levels. The gyration radius also fluctuates as time evolves. From Fig. 10, we fitted a linear line between VDE and the gyration radius. Since the VDE is inversly correlated with the gyration radius, the excess electron is more likely to escape when it occupies larger space on the surface of the cluster.

2.3.2 $(H_2O)_{30}^-$ surface and interior states

We generate the $(H_2O)_{30}(Cl)^-$ as before, and let the system relax at room temperature. The Cl^- again drifts from the center of the cluster to its surface (See Fig. 11). It's much more time consuming to conduct fully QM calculation for systems with this size, therefore, we select 19 water molecules closest to the Cl^- as quantum water molecules, and show them in blue in Fig. 11. The Cl^- is then replaced by an excess electron, and QM/MM simulation starts from here. The system reaches equilibrium after 2 ps with a time step 1 fs. We continue the simulation to 4.5 ps to and discover a VDE of $(1.56 \pm 0.14)eV$. Fig. 12 is a equilibrated configuration of the $(H_2O)_{30}(Cl)^-$

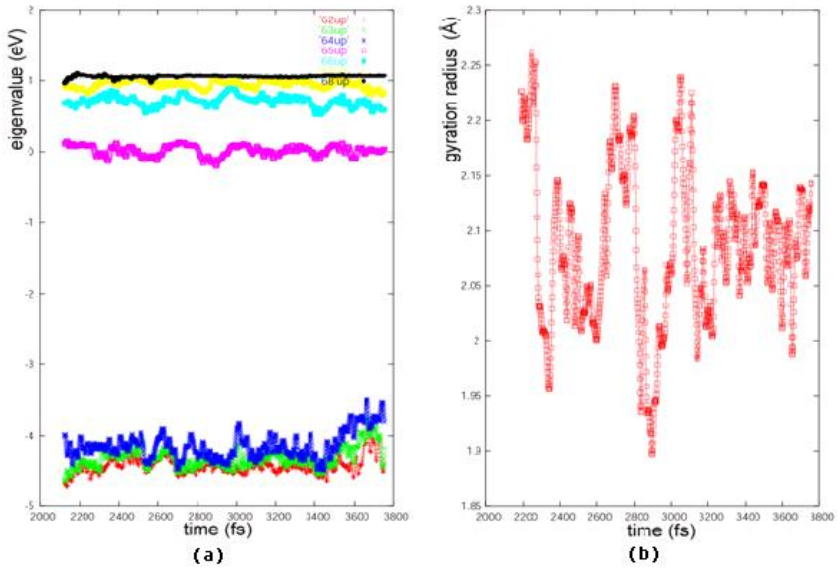

Figure 9: Equilibrium trajectory of $(H_2O)_{16}^-$ cluster at 300 K from 2 ps to 3.8 ps. (a)Eigenvalues of energy levels around the highest occupied Kohn-Shan orbital at which the excess electron stays. The highest occupied Kohn-Shan orbital is colored in pink. (b)Gyration radius of the excess electron.

cluster and with density distribution of the excess electron. From the picture the excess electron occupies a pocket like space on the surface of the cluster. The size of the pocket is around $6.6\mathring{A}$, while the size of the whole cluster is around $10\mathring{A}$. Obviously this is a surface state.

We also capture the eigenvalues of energy level around the highest occupied Kohn-Shan orbital and the gyration radius of the excess electron along equilibrium trajectory as shown in Fig. 13. Compared with the energy levels in $(H_2O)_{16}^-$ cluster, again, the highest occupied Kohn-Shan orbital is the energy level at which the excess electron stays, and it is well separated with all the other energy levels. However, the value of this orbital are mostly below 0, lower than the values in $(H_2O)_{16}^-$ cluster. Therefore, we conclude the excess electron is more tightly bounded to the $(H_2O)_{30}^-$ cluster.

From the discussion above, we conclude that at temperature 300 K, the equilibrium state for $(H_2O)_{30}^-$ is a surface state. Is it possible to obtain an interior state for

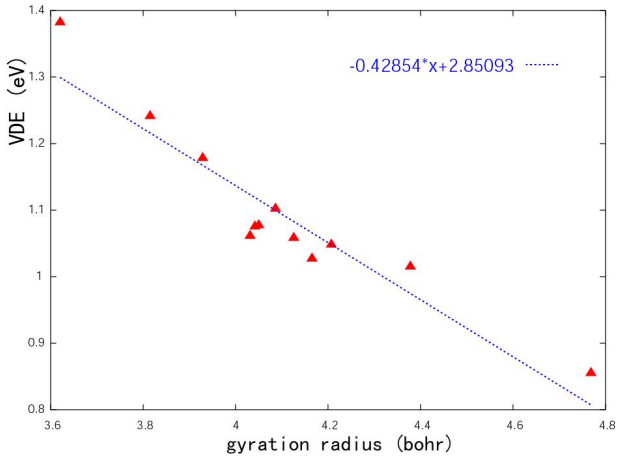

Figure 10: Relationship between gyration radius of the excess electron with its VDE in $(H_2O)_{16}^-$ cluster at 300 K.

such cluster? We create an $(H_2O)_{30}Cl^-$ cluster again with the Cl^- in the middle, relax it at 30 K to confine the chlorine inside. A minimum energy configuration for such cluster is shown in Fig. 14. We keep temperature at 30 K and apply QM/MM approach to this system with QM water molecules colored with blue oxygens. The cluster reaches equilibrium after a duration of 2 ps with a time step 2 fs. We continue the simulation and obtain an equilibrium trajectory for another 4 ps. Fig. 15 is a picture of the cluster in equilibrium. The excess electron stays inside the cluster, forming a cavity of size 4.5$\mathring{A}$, while the size of the cluster is about 10$\mathring{A}$. We conclude the excess electron is in an interior state. Compared with the surface state of the same cluster, the sizes of the clusters are similar, but the excess electron occupies less space in the interior state. The average VDE of the excess electron is computed from 10 equally spaced points along the equilibrium trajectory from 2 ps to 6 ps and the value is $(2.14 \pm 0.04)eV$. The eigenvalues of energy level around the highest occupied Kohn-Shan orbital and the gyration radius of the excess electron along equilibrium trajectory are plotted in Fig. 16. From the eigenvalue of the highest occupied Kohn-Shan orbital, the excess electron is even more tightly bounded to the cluster in the interior state than in the surface state.

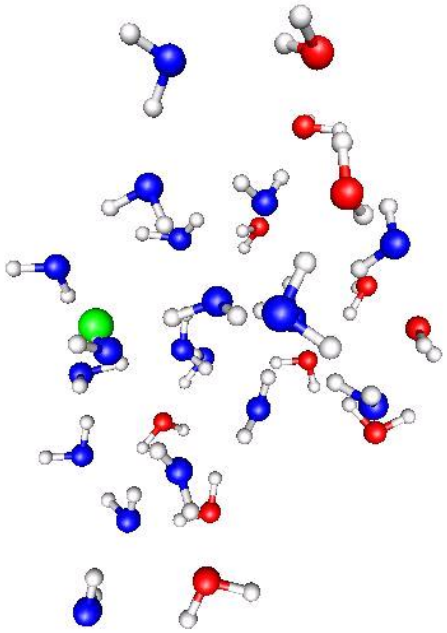

Figure 11: The starting configuration of QM/MM calculation for $(H_2O)_{30}^-$. The green point represents the centroid of the excess electron distribution. And the red and blue oxygens indicates MM and QM water molecules respectively.

2.3.3 $(H_2O)_{50}^-$ surface and interior states

The $(H_2O)_{50}(Cl)^-$ cluster is created with the Cl^- in the center of the cluster, and relaxed at room temperature until it reaches a local minimum energy configuration, when the Cl^- moves to the surface of the cluster.(See Fig. 17). We identify 20 water molecules nearest to the chlorine as quantum water molecules, and start QM/MM calculations. The system reaches equilibrium after 2.5 ps with a time step 1 fs. We continue the simulation to 5 ps and discover a VDE of $(1.24 \pm 0.2)eV$. From Fig. 18, the excess electron localizes on the surface of the cluster. The space the excess electron occupies is around $9.5\mathring{A}$, the size of the whole cluster is around $12\mathring{A}$.

The eigenvalues of energy level around the highest occupied Kohn-Shan orbital and the gyration radius of the excess electron along equilibrium trajectory are show in Fig. 19.

This simulation shows us that at 300 K, the equilibrium state for $(H_2O)_{50}^-$ is a surface state. To confide the excess electron inside the cluster, we control the

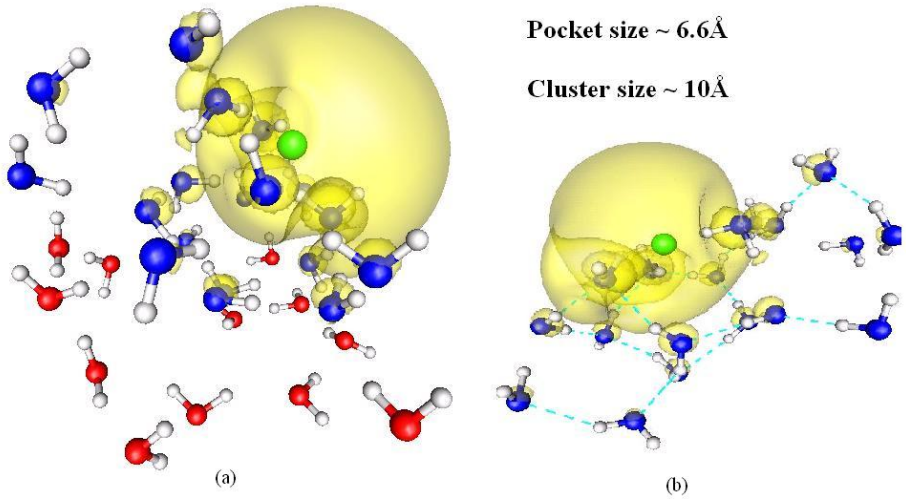

Figure 12: Configuration of $(H_2O)_{30}^-$ in equilibrium at 300 K. (a)The water molecules with oxygens colored in red are treated classically, while blue oxygens indicates quantum water molecules. The yellow contour is the equi-density surface which encompasses more than 50% of the density of the excess electron. (b)An enlarged picture of the excess electron density contour with only the QM water molecules. Blue dashed lines indicate hydrogen bonds.

temperature at 30 K after generating the same $(H_2O)_{50}Cl^-$ cluster with the Cl^- in the middle. (See Fig. 20). We keep temperature at 30 K and apply QM/MM approach to this system with QM water molecules colored with blue oxygens. The cluster reaches equilibrium after a duration of 3 ps with a time step 2 fs. We continue the simulation and obtain an equilibrium trajectory for another 4 ps. Fig. 21 is a picture of the cluster in equilibrium. The excess electron stays inside the cluster, forming a cavity of size $3\mathring{A}$, while the size of the cluster is about $12\mathring{A}$. We conclude the excess electron is in an interior state. Compared with the surface state of the same cluster, the whole clusters stays at similar size, but the excess electron occupies much less space in the interior state. The average VDE of the excess electron is computed from 10 points along the equilibrium trajectory from 3 ps to 7 ps and its value is $(2.14 \pm 0.086)eV$. The eigenvalues of energy level around the highest occupied Kohn-Shan orbital and the gyration radius of the excess electron along equilibrium trajectory are plotted in Fig. 22.

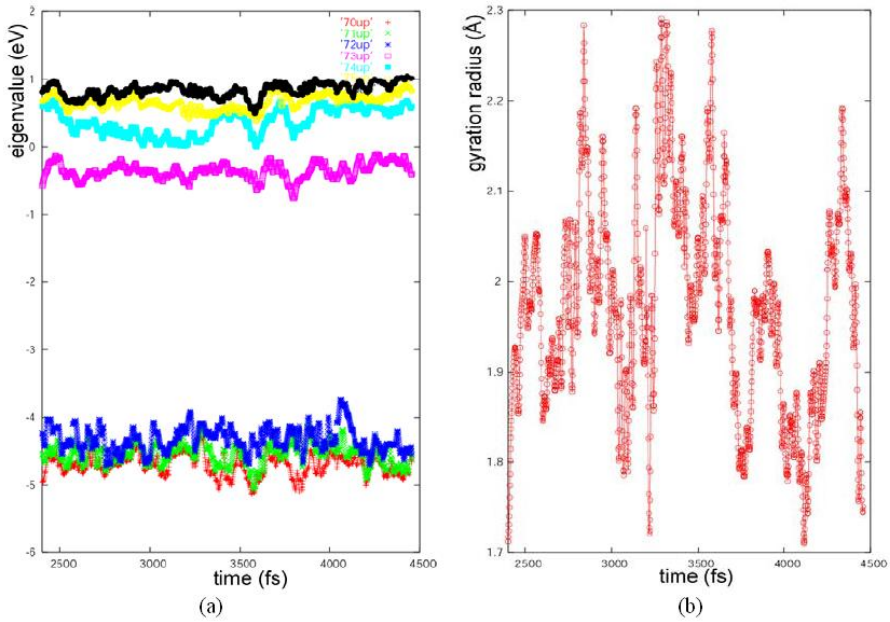

Figure 13: Equilibrium trajectory of the $(H_2O)_{30}^-$ cluster at 300 K from 2.4 ps to 4.5 ps. (a)Eigenvalues of energy level around the highest occupied Kohn-Shan orbital at which the excess electron stays. The highest occupied Kohn-Shan orbital is colored in pink. (b)Gyration radius of the excess electron.

2.3.4 $(H_2O)_{100}^-$ interior and surface states

After creating the $(H_2O)_{100}(Cl)^-$ cluster with the Cl^- in the center of the cluster, we run molecular dynamics simulation at room temperature until it reaches a local minimum energy configuration. From Fig. 23 we see for this cluster, the Cl^- stays inside the cluster. About 20 water molecules nearest to the chlorine are selected as quantum water molecules, and we start QM/MM calculations after replacing the chlorine with an excess electron. The system is equilibrated at 600 K for 2 ps and then gradually cooled to 300 K. An average value VDE of $(2.38 \pm 0.30)eV$ was determined from calculation corresponding to 20 points along the equilibrium trajectory at 300 K. Fig. 24 shows a configuration of the $(H_2O)_{100}^-$ cluster in equilibrium state at 300 K. From the picture the excess electron localizes inside the cluster. The space the excess electron occupies is around $5\mathring{A}$, the size of the whole cluster is around $19.5\mathring{A}$.

The eigenvalues of energy level around the highest occupied Kohn-Shan orbital

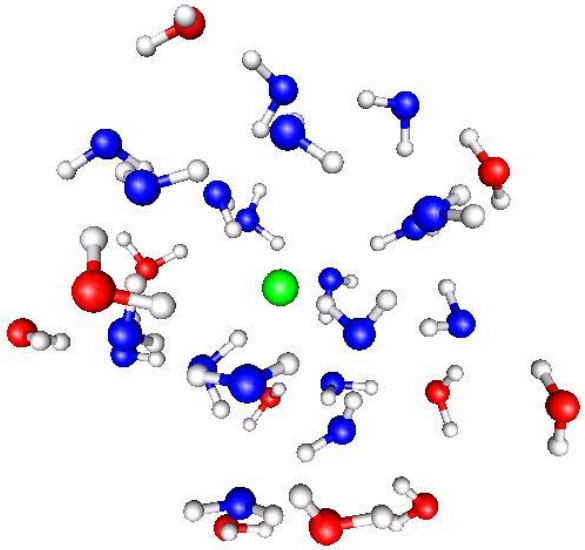

Figure 14: The starting configuration of QM/MM calculation at 30 K for $(H_2O)_{30}^-$. The green point represents the centroid of the excess electron distribution. And the red and blue oxygens indicates MM and QM water molecules respectively.

and the gyration radius of the excess electron along equilibrium trajectory are shown in Fig. 25.

This simulation shows us that at 300 K, the excess electron will locate at an interior cavity if it is created in the middle of the cluster. But that doesn't exclude the existence of a stable surface-bound state. To test it, we generate another $(H_2O)_{100}Cl^-$ cluster with the Cl^- on the surface, and control the Cl^- on the surface while relaxing the whole system. Fig. 26 is a local minimum energy configuration from this procedure. QM/MM approach is then applied to this system with QM water molecules colored with blue oxygens in Fig. 26. The simulation shows that if the temperature is kept at 300 K, the excess electron starting on the surface of the cluster tends to gradually move into the middle of the cluster. To confide the electron on the surface, temperature must be reduced from 200 K. Fig. 27 shows a surface state of the $(H_2O)_{100}^-$ in equilibrium at 200 K, and we compute the VDE of the excess electron to be $(1.34 \pm 0.1)eV$. The eigenvalues of energy level around the highest occupied Kohn-Shan orbital and the gyration radius of the excess electron along equilibrium

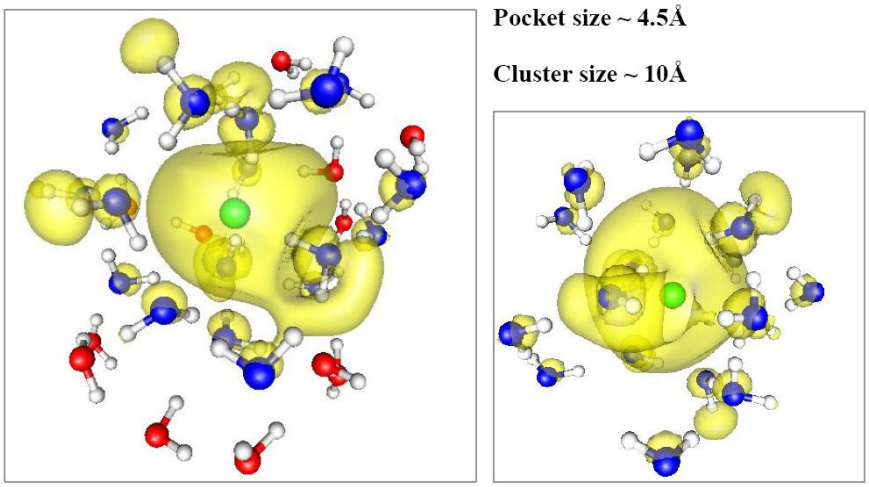

Figure 15: Configuration of $(H_2O)_{30}^-$ in equilibrium at 30 K. (a)The water molecules with oxygens colored in red are treated classically, while colored in blue are treated quantum mechanically. The yellow contour is the equi-density surface which encompasses more than 50% of the density of the excess electron. (b)An enlarged picture of the excess electron density contour with only the QM water molecules. Blue dashed lines indicate hydrogen bonds.

trajectory are plotted in Fig. 28.

2.3.5 $(H_2O)_{300}^-$ interior state

The $(H_2O)_{300}(Cl)^-$ cluster is created again with the Cl^- in the center of the cluster. After molecular dynamics relaxation the system rearrange itself with the Cl^- staying inside.(See Fig. 29. From this point we start QM/MM calculations after replacing the chlorine with an excess electron. The system is equilibrated at 300 K for 3 ps with a time step of 1 fs. An average value VDE of $(2.446 \pm 0.38)eV$ is determined along the equilibrium trajectory. Fig. 24 shows that the excess electron will localize inside the cluster, forming a cavity of size $8\mathring{A}$, while the size of the whole cluster around $25\mathring{A}$.

The eigenvalues of energy level around the highest occupied Kohn-Shan orbital and the gyration radius of the excess electron along equilibrium trajectory are shown in Fig. 31.

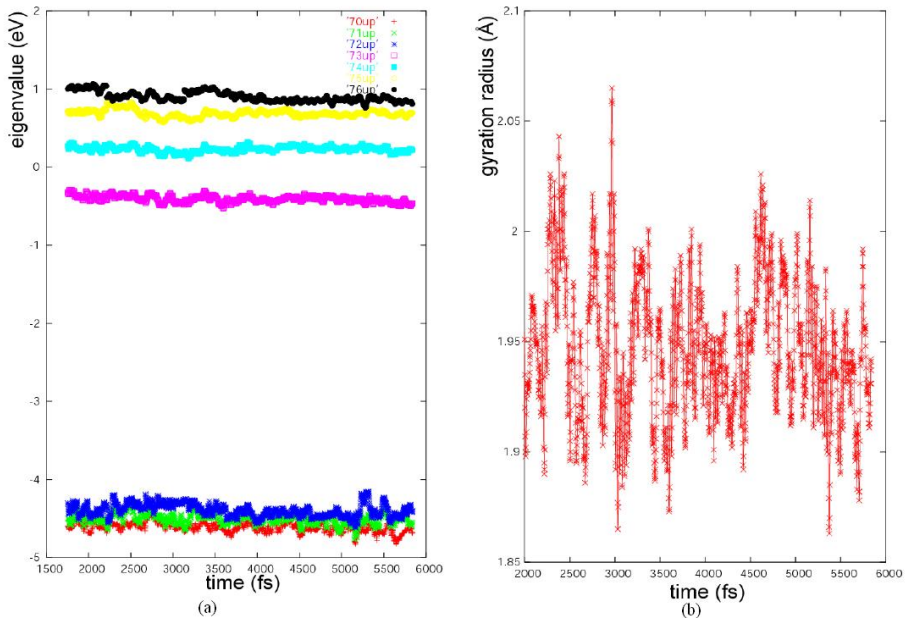

Figure 16: Equilibrim trajectory of the $(H_2O)_{30}^-$ cluster at 30 K from 2 ps to 6 ps. (a)Eigenvalues of energy level around the highest occupied Kohn-Shan orbital at which the excess electron stays. The highest occupied Kohn-Shan orbital is colored in pink. (b)Gyration radius of the excess electron.

Table 2: Comparison of VDE with experimental results

	Interior		Surface	
cluster size	Exp., eV	Ours', eV	Exp., eV	Ours', eV
16	-	-	0.97	1.13 ± 0.1 (300K)
30	1.34	2.14 ± 0.04 (30K)	0.59	1.56 ± 0.14 (300K)
50	1.77	2.14 ± 0.09 (30K)	0.97	1.24 ± 0.2 (300K)
100	2.19	2.38 ± 0.3 (300K)	1.14	1.34 ± 0.1 (200K)
300	2.38	2.45 ± 0.2 (300K)	-	-

2.4 Conclusion

We have performed a hybrid QM/MM simulation and subsequent analysis of the electron localization sites existing in various finite size neutral water clusters. We computed the VDE energy for water clusters with sizes ranging from 16 to 300. Table 2 lists our results with comparison to the experimental results in [22]. We also demonstrated the existence of both the surface and the interior localization modes through energetic structural and spectroscopic analysis.

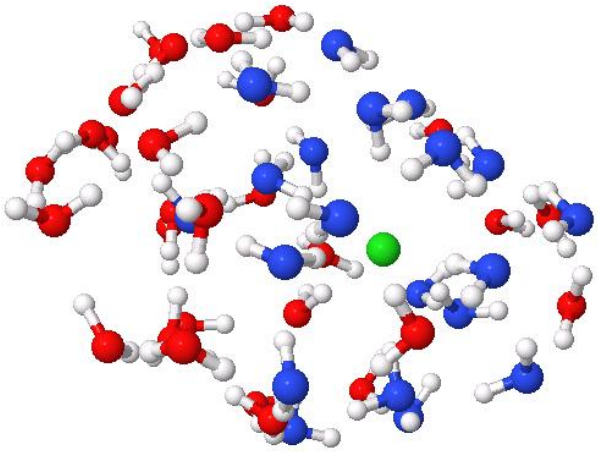

Figure 17: The starting configuration of QM/MM calculation for $(H_2O)^-_{50}$. The green point represents the centroid of the excess electron distribution. And the red and blue oxygens indicates MM and QM water molecules respectively.

From our analysis, at room temperature, surface state is more stable for cluster $n \leq 50$. To form an interior state at this small sizes, an electron has to be initiated in the middle of the cluster and temperature must kept very low to prohibit the movement of the electron. For cluster $n \geq 100$, interior state is more stable at room temperature. Temperature needs to be reduced to 200K to maintain a surface state for $H_2O^-_{100}$. Interior state will evolve to surface state very fast for $H_2O^-_{100}$. The transition happens between water clusters size 50 and 100.

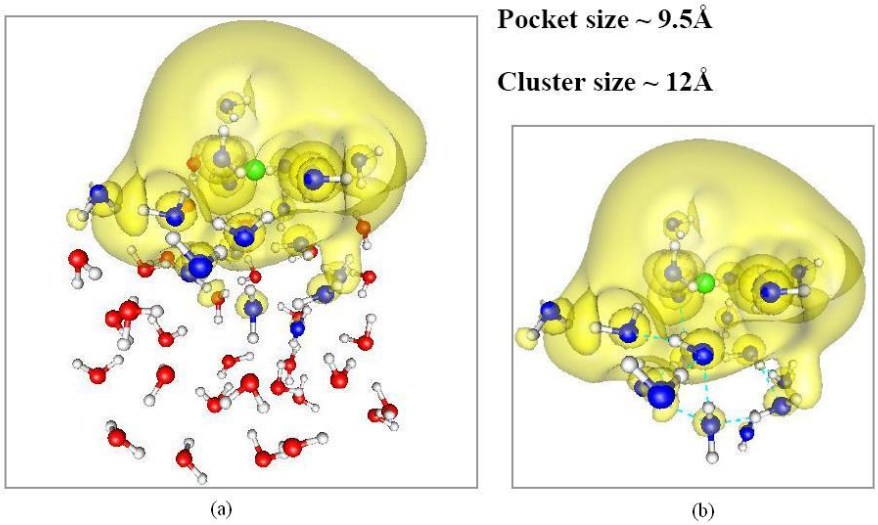

Figure 18: Configuration of $(H_2O)_{50}^-$ at equilibrium state at 300 K. (a)The water molecules with oxygens colored in red are treated classically, while blue oxygens indicate quantum water molecules. The yellow contour is the equi-density surface which encompasses more than 50% of the density of the excess electron. (b)An enlarged picture of the excess electron density contour with only the QM water molecules. Blue dashed lines indicate hydrogen bonds.

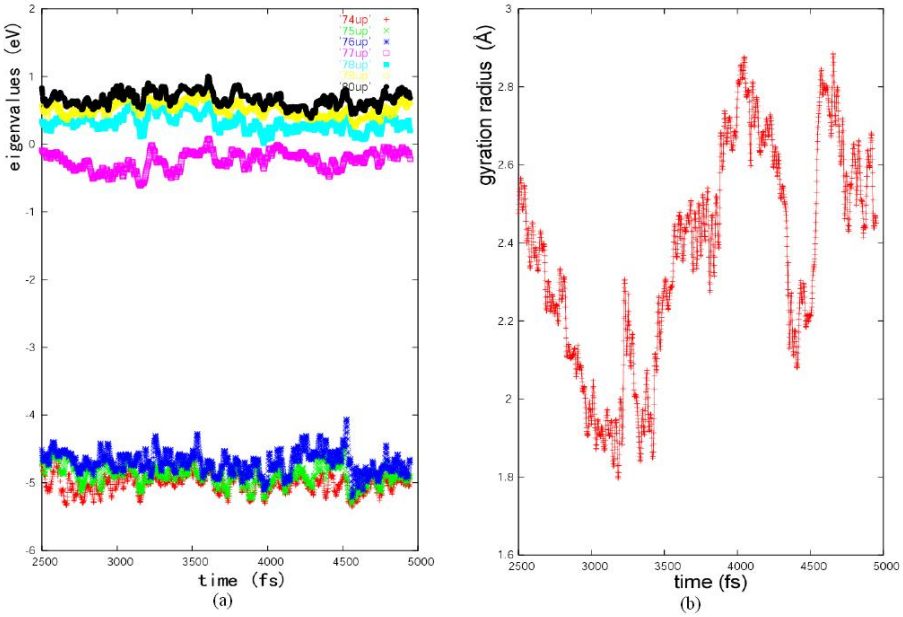

Figure 19: Equilibrium trajectory of the $(H_2O)_{50}^-$ cluster at 300 K from 2.5 ps to 5 ps. (a)Eigenvalues of energy level around the highest occupied Kohn-Shan orbital at which the excess electron stays. The highest occupied Kohn-Shan orbital is colored in pink. (b)Gyration radius of the excess electron.

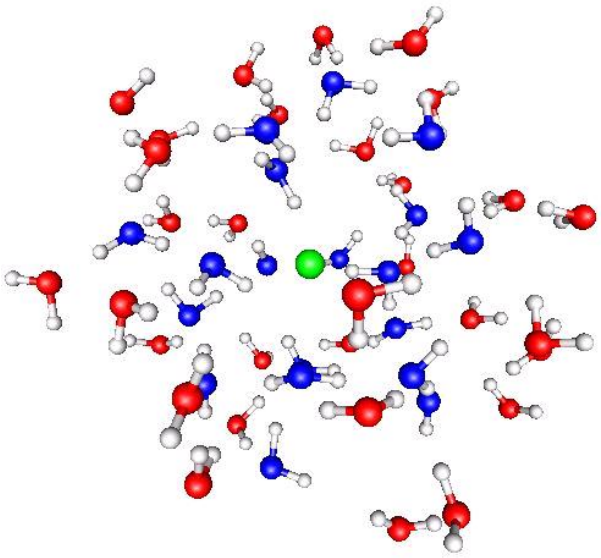

Figure 20: The starting configuration of QM/MM calculation at 30 K for $(H_2O)_{50}^-$. The green point represents the centroid of the excess electron distribution. And the red and blue oxygens indicates MM and QM water molecules respectively.

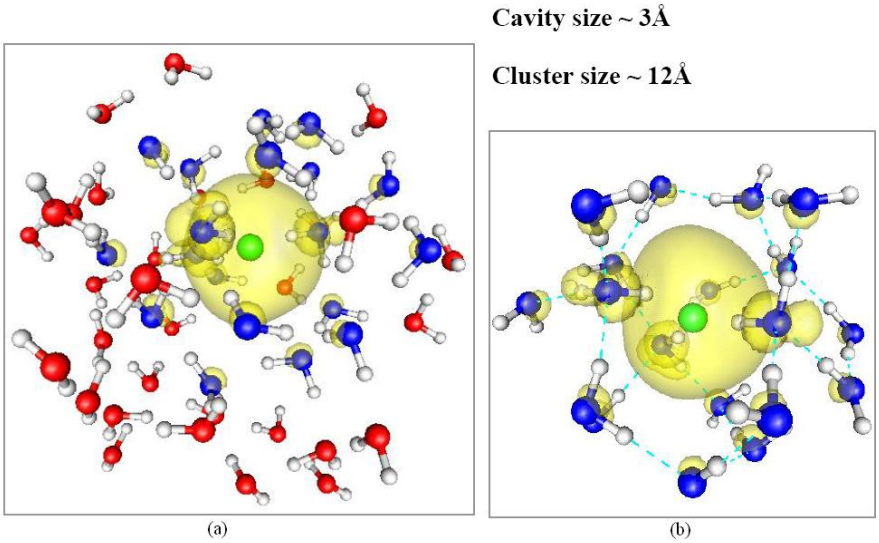

Figure 21: Configuration of $(H_2O)_{50}^-$ in equilibrium at 30 K. (a)The water molecules with oxygens colored in red are treated classically, while blue oxygens indicate quantum water molecules. The yellow contour is the equi-density surface which encompasses more than 50% of the density of the excess electron. (b)An enlarged picture of the excess electron density contour with only the QM water molecules. Blue dashed lines indicate hydrogen bonds.

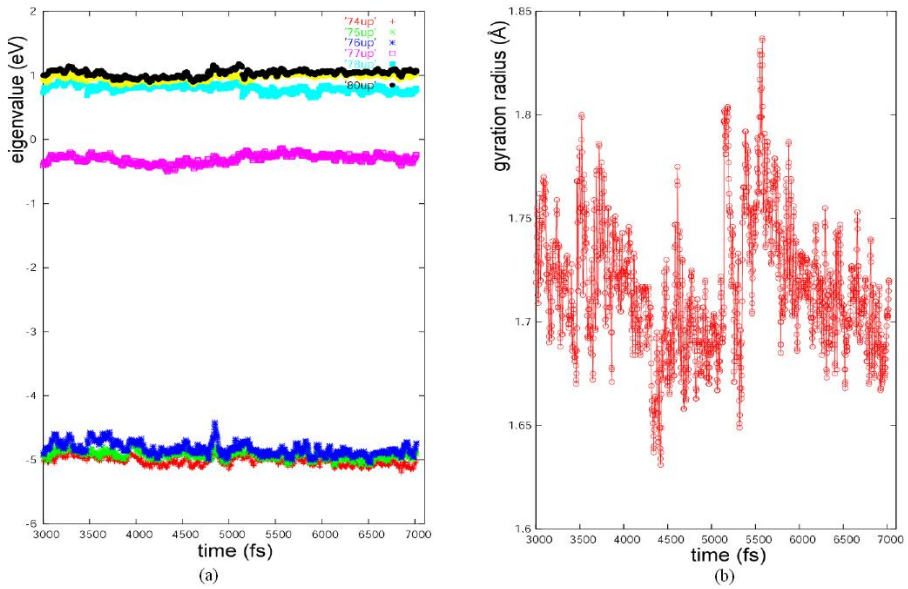

Figure 22: Equilibrium trajectory of the $(H_2O)_{50}^-$ cluster at 30 K for 4 ps. (a)Eigenvalues of energy level around the highest occupied Kohn-Shan orbital at which the excess electron stays. The highest occupied Kohn-Shan orbital is colored in pink. (b)Gyration radius of the excess electron.

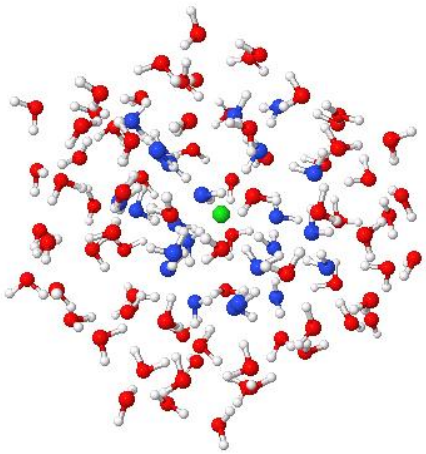

Figure 23: The starting configuration of QM/MM calculation for $(H_2O)_{100}^-$. The green point represents the centroid of the excess electron distribution. And the red and blue oxygens indicates MM and QM water molecules respectively.

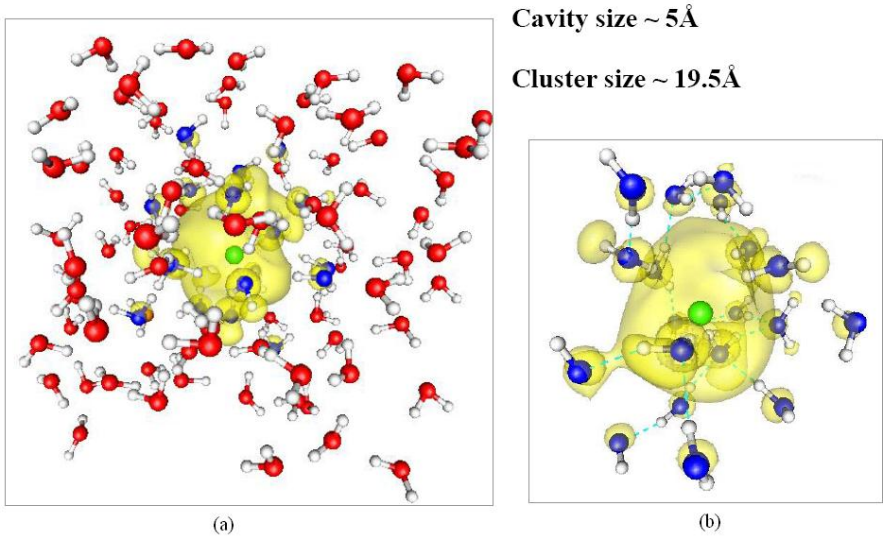

Figure 24: Configuration of $(H_2O)_{100}^-$ in equilibrium at 300 K. (a)The water molecules with oxygens colored in red are treated classically, while blue oxygens indicate quantum water molecules. The yellow contour is the equi-density surface which encompasses more than 50% of the density of the excess electron. (b)An enlarged picture of the excess electron density contour with only the QM water molecules. Blue dashed lines indicate hydrogen bonds.

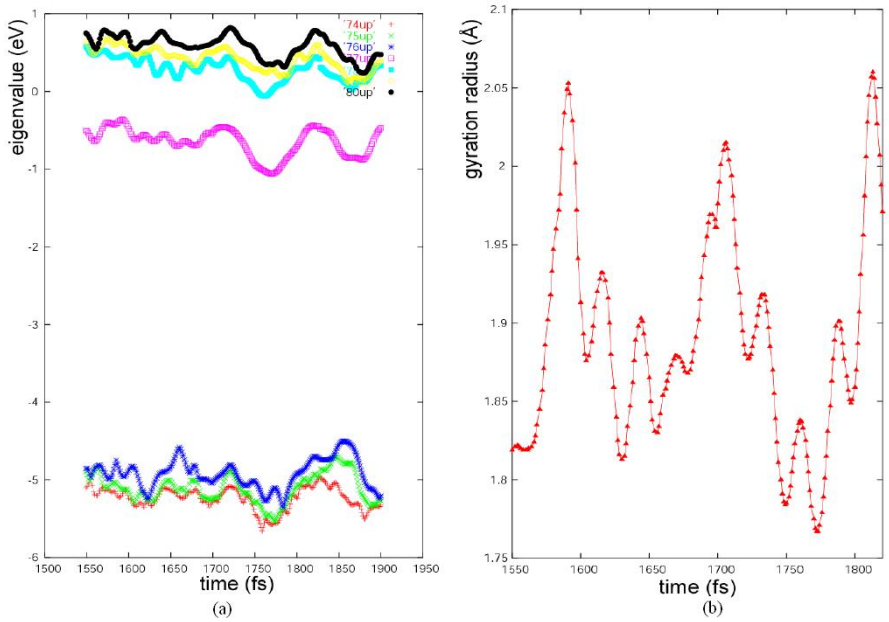

Figure 25: Equilibrium trajectory of the $(H_2O)_{100}^-$ cluster at 300 K for 0.45 ps. (a)Eigenvalues of energy level around the highest occupied Kohn-Shan orbital at which the excess electron stays. The highest occupied Kohn-Shan orbital is colored in pink. (b)Gyration radius of the excess electron.

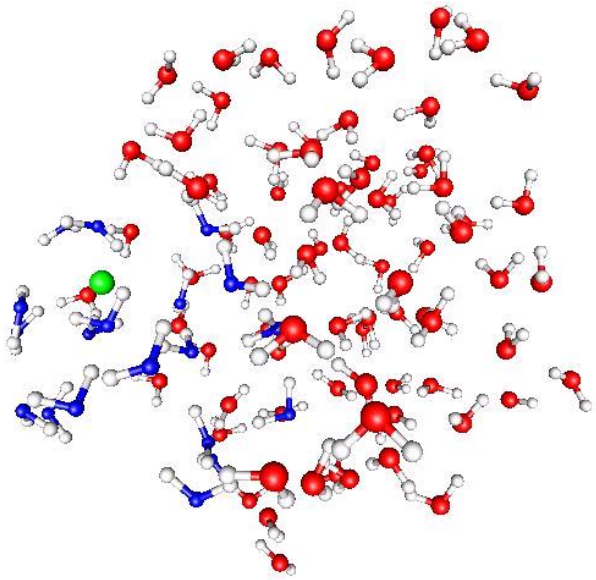

Figure 26: The starting configuration of QM/MM calculation for $(H_2O)^-_{100}$. The green point represents the centroid of the excess electron distribution. And the red and blue oxygens indicates MM and QM water molecules respectively.

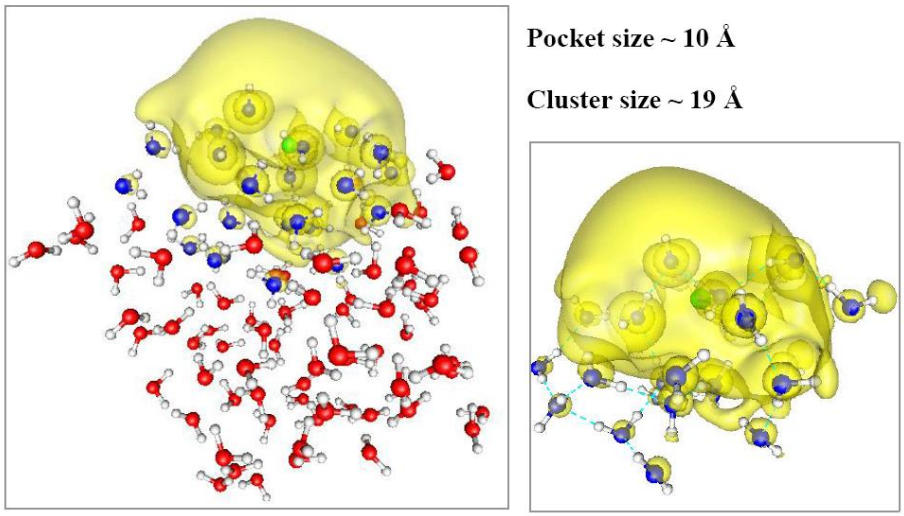

Figure 27: A surface state configuration of $(H_2O)^-_{100}$ in equilibrium at 200 K. (a)The water molecules with oxygens colored in red are treated classically, while blue oxygens indicate quantum water molecules. The yellow contour is the equi-density surface which encompasses more than 50% of the density of the excess electron. (b)An enlarged picture of the excess electron density contour with only the QM water molecules. Blue dashed lines indicate hydrogen bonds.

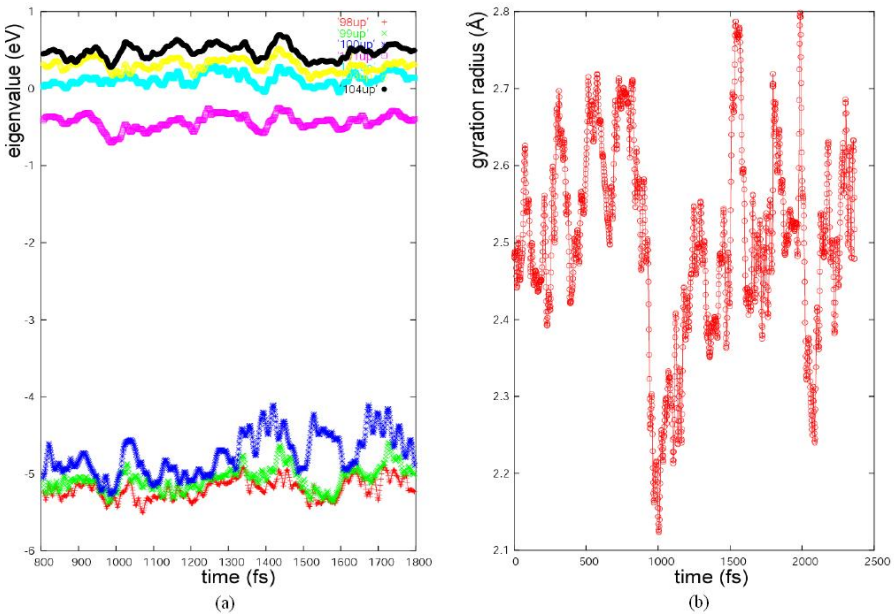

Figure 28: Equilibrium trajectory of the $(H_2O)^-_{100}$ cluster at 200 K. (a)Eigenvalues of energy level around the highest occupied Kohn-Shan orbital at which the excess electron stays. The highest occupied Kohn-Shan orbital is colored in pink. (b)Gyration radius of the excess electron.

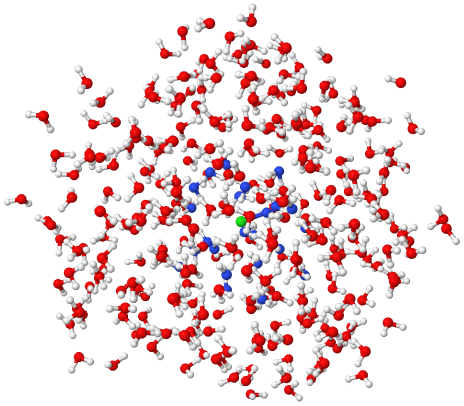

Figure 29: The starting configuration of QM/MM calculation for $(H_2O)^-_{300}$. The green point represents the centroid of the excess electron distribution. And the red and blue oxygens indicates MM and QM water molecules respectively.

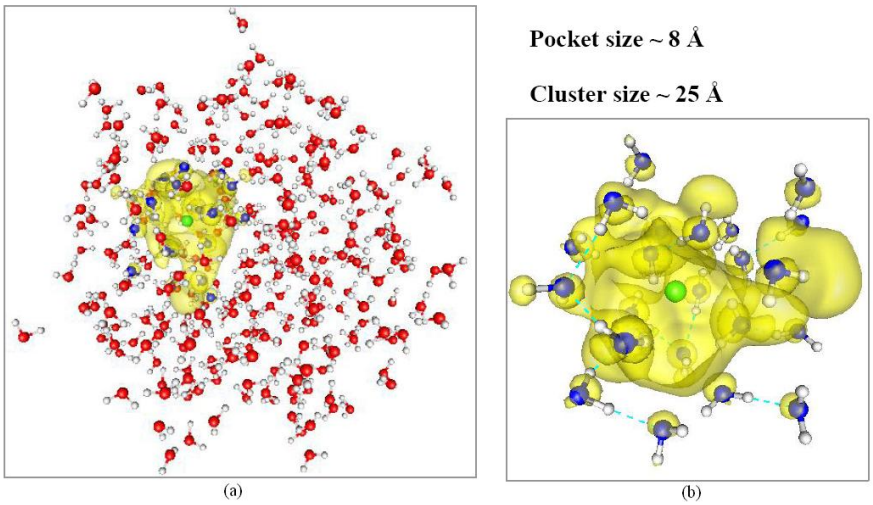

Figure 30: Configuration of $(H_2O)^-_{300}$ in equilibrium at 300 K. (a)The water molecules with oxygens colored in red are treated classically, while colored in blue are treated quantum mechanically. The yellow contour is the equi-density surface which encompasses more than 50% of the density of the excess electron. (b)An enlarged picture of the excess electron density contour with only the QM water molecules. Blue dashed lines indicate hydrogen bonds.

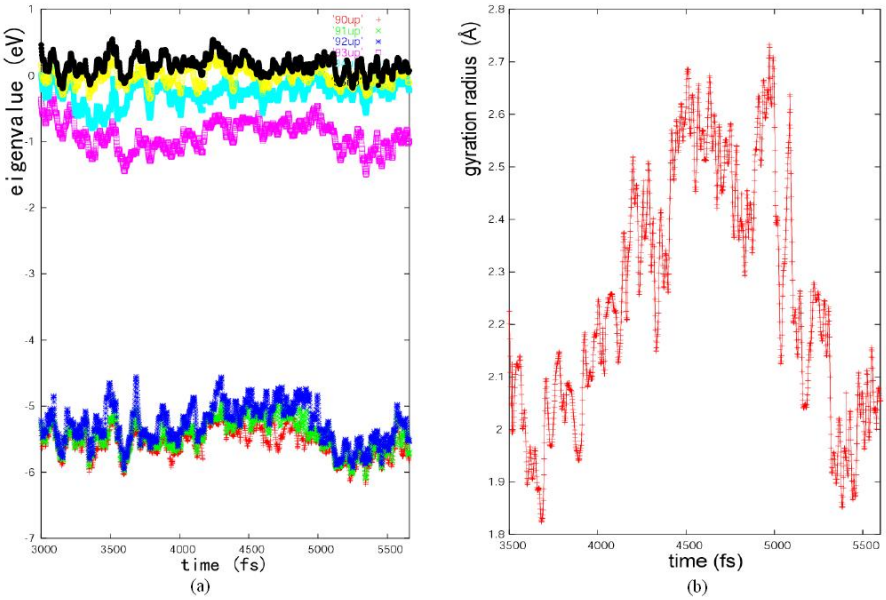

Figure 31: Equilibrium trajectory of the $(H_2O)^-_{300}$ cluster at 300 K for 2.5 ps. (a)Eigenvalues of energy level around the highest occupied Kohn-Shan orbital at which the excess electron stays. The highest occupied Kohn-Shan orbital is colored in pink. (b)Gyration radius of the excess electron.

PART II

ELECTRONIC SPECTRUM AND SPIN STRUCTURES OF FOUR-ELECTRON DOUBLE QUANTUM DOTS

CHAPTER III

EXACT DIAGONALIZATION METHOD FOR LATERAL DOUBLE QUANTUM DOTS

Semiconductor quantum dots(QD) are small man-made structures in a solid, typically with sizes ranging from nanometers to a few microns. They consist of $10^3 - 10^9$ atoms with an equivalent number of electrons. In semiconductors all electrons are tightly bound to the nuclei except for a small fraction of free electrons. This small number can be anything from a single free electron, to a puddle of several thousands, in quantum dots defined in a semiconductor. Current nanofabrication technology allows us to precisely control the size and shape of these dots. The electronic properties of dots show many parallels with those of atoms. Most notably, the confinement of the electrons in all three spatial directions results in a quantized energy spectrum. Quantum dots are therefore regarded as artificial atoms [48, 6], a term suggestive of strong similarities between these manmade nanodevices and the physical behavior of nature atoms.

Two dimensional semiconductor QD's are typically fabricated in the semiconductor heterostructures using lithographic techniques. Current-voltage measurements are used to observe the atom-like properties of the quantum dot. In addition, it is possible to vary the exact number of electrons on the dot by changing the voltage applied to a nearby gate electrode. This control allows one to scan through the entire periodic table of artificial elements by simply changing the voltage. Quantum dot technology is one of the most promising candidates for various fields. In electronic applications they have been proven to operate like a single-electron transistor and

show the Coulomb blockage effect. They have been suggested as implementations of qubits for quantum information processing. With superior transport and optical properties, they are also being researched for use in diode lasers, amplifiers, and biological sensors.

Driven by growing interest in solid state nanostrucutres and potential technological considerations, an intensive effort has been devoted towards the elucidations of quantum dots. A natural extension has also developed in the direction of two-dimensional QD molecules(QDM's, often referred to as artificial molecules), aiming at clarifying the analogies and differences between such artificially fabricated molecular nanostructures and the natural molecules. A major attraction of QD's and QDM's is the fact that, due to their larger size, orbital magnetic effects become important for magnetic field values easily attainable in the laboratory. This contrasts with the case of natural atoms and molecules for which magnetic fields of sufficient strength for the production of phenomena related to orbital magnetism are known to occur only in astrophysical environments, e.g., on the surfaces of neutron stars.

The N-electron QD's has been extensively studied in the last few years, both experimentally [25, 31, 10] and theoretically [40, 50, 67, 30, 72, 74, 75, 70, 73]. Experimentally, the case of parabolic QDs with a small number of electrons ($N \leq 30$) has attracted particular attentions, as a result of precise control of the number of electrons in the dot that has been demonstrated in several experimental investigations. Naturally, QDs with a small number of electrons are also most attractive for theoretical investigations.

A major factor motivating the study of two dimensional quantum dots has been the promising outlook and potential of quantum dots concerning the implementation of solid-state quantum computing and quantum information devices [28, 15, 47]. To this effect highly precise control of the space and spin degrees of freedom of a small number N of confined electrons (down to an empty [54, 31, 29] QD) needs to be

achieved, and experimentally this was demonstrated recently for two electrons in a lateral double quantum dot molecule [43]. From the theoretical standpoint, high-level computational methods beyond the mean-field approximations are needed [76] that are able to provide solutions preserving all the symmetries of the many-body Hamiltonian. For example, conservation of total spin is essential for describing spin entanglement in small assemblies of electrons that exhibit localization in space. Such assemblies may be viewed as finite Heisenberg spin clusters [41, 52] whose quantum behavior (due to finite-size fluctuations and correlation effects) differs drastically from the behavior expected from magnetic systems in the thermodynamic limit [41, 13].

There is an abundance of experimental and theoretical publications concerning *circular single* quantum dots with a small number of electrons [40, 49, 25, 76, 36, 35, 2]. In this thesis, we use exact diagonalization [76] (EXD) to investigate the properties of *lateral double quantum dots* (DQDs) containing four electrons. DQDs are referred to also as artificial molecules. DQDs containing two electrons have been already studied extensively both experimentally [43] and theoretically [76, 34, 27]. Experimental studies of DQDs with three or four electrons are absent as yet. We are aware of one theoretical study of a lateral DQD with three electrons [59].

Due to novel quantum behavior discovered in our investigations (compared to circular QDs, both concerning the spectra and entanglement aspects), we hope that the present work will motivate further experimental studies on lateral DQDs.

3.1 The two-center-oscillator confining potential

Following the course of development for single QD's, first insights into the energetics and spectra of lateral QDM's may be gained from single-electron (SE) energy levels calculated for harmonic confinements using a semi-analytic two-center oscillator model (TCOM).Indeed, the single-particle levels associated with the confining potential of the artificial molecule are determined by the single-particle hamiltonian

[69, 38, 68]

$$H = T \;+\; \frac{1}{2}m^*\omega_{xk}^2 x^2 + \frac{1}{2}m^*\omega_{yk}^2 y_k'^2 \\ +\; V_{neck}(y) + h_k + \frac{g^*\mu_B}{\hbar}\mathbf{B}\cdot\mathbf{s}\ , \tag{3.1}$$

where $y_k' = y - y_k$ with $k = 1$ for $y < 0$ (left) and $k = 2$ for $y > 0$ (right), and the h_k's control the relative well-depth, thus allowing studies of hetero-QDM's. x denotes the coordinate perpendicular to the interdot axis (y). $T = (\mathbf{p} - e\mathbf{A}/c)^2/2m^*$, with $\mathbf{A} = 0.5(-By, Bx, 0)$, and the last term in Eq. (3.1) is the Zeeman interaction with g^* being the effective g factor, μ_B the Bohr magneton, and $\mathbf{s}$ the spin of an individual electron. Here we limit ourselves to systems with $\hbar\omega_{x1} = \hbar\omega_{x2} = \hbar\omega_x$. The most general shapes described by H are two semiellipses connected by a smooth neck [$V_{neck}(y)$]. $y_1 < 0$ and $y_2 > 0$ are the centers of these semiellipses, $d = y_2 - y_1$ is the interdot distance, and m^* is the effective electron mass.

For the smooth neck, we use $V_{neck}(y) = \frac{1}{2}m^*\omega_{yk}^2[c_k y_k'^3 + d_k y_k'^4]\theta(|y| - |y_k|)$, where $\theta(u) = 0$ for $u > 0$ and $\theta(u) = 1$ for $u < 0$. The four constants c_k and d_k can be expressed via two parameters, as follows: $(-1)^k c_k = (2 - 4\epsilon_k^b)/y_k$ and $d_k = (1 - 3\epsilon_k^b)/y_k^2$, where the barrier-control parameters $\epsilon_k^b = (V_b - h_k)/V_{0k}$ are related to the actual (controllable) height of the bare barrier (V_b) between the two QD's, and $V_{0k} = m^*\omega_{yk}^2 y_k^2/2$ (for $h_1 = h_2$, $V_{01} = V_{02} = V_0$).

The single-particle levels of H, including an external perpendicular magnetic field B, are obtained by numerical diagonalization in a (variable-with-separation) basis consisting of the eigenstates of the auxiliary hamiltonian:

$$H_0 = \frac{\mathbf{p}^2}{2m^*} + \frac{1}{2}m^*\omega_x^2 x^2 + \frac{1}{2}m^*\omega_{yk}^2 y_k'^2 + h_k\ . \tag{3.2}$$

This eigenvalue problem is separable in x and y, i.e., the wave functions are written as

$$\Phi_{\mu\nu}(x, y) = X_\mu(x)Y_\nu(y). \tag{3.3}$$

The solutions for $X_\mu(x)$ are those of a one-dimensional oscillator, and for $Y_\nu(y)$ they can be expressed through the parabolic cylinder functions [69, 38, 68] $U[\alpha_k, (-1)^k \xi_k]$, where $\xi_k = y'_k \sqrt{2m^* \omega_{yk}/\hbar}$, $\alpha_k = (-E_y + h_k)/(\hbar\omega_{yk})$, and $E_y = (\nu + 0.5)\hbar\omega_{y1} + h_1$ denotes the y-eigenvalues. The matching conditions at $y = 0$ for the left and right domains yield the y-eigenvalues and the eigenfunctions $Y_\nu(y)$ (μ is integer and ν is in general real).

In this paper, we will limit ourselves to symmetric (homopolar) QDM's, i.e., $\hbar\omega_x = \hbar\omega_{y1} = \hbar\omega_{y2} = \hbar\omega_0$, and use $\hbar\omega_0 = 5$ meV and $m^* = 0.067 m_e$ (this effective-mass value corresponds to GaAs).

3.2 Single particle states

The single-particle levels of H, including an external perpendicular magnetic field B, are obtained by numerical diagonalization in a (variable-with-separation) basis consisting of the eigenstates of the auxiliary hamiltonian:

$$H_0 = \frac{\mathbf{p}^2}{2m^*} + \frac{1}{2} m^* \omega_x^2 x^2 + \frac{1}{2} m^* \omega_{yi}^2 y_i'^2 + h_i \ . \tag{3.4}$$

This eigenvalue problem is separable in x and y, i.e., the wave functions are written as $\Phi_{\mu\nu}(x, y) = X_\mu(x) Y_\nu(y)$. The solutions for $X_\mu(x)$ are those of a one-dimensional oscillator, and for $Y_\nu(y)$ they can be expressed through the parabolic cylinder functions $U[\alpha_i, (-1)^i \xi_i]$, where $\xi_i = y'_i \sqrt{2m^* \omega_{yi}/\hbar}$, $\alpha_i = (-E_y + h_i)/(\hbar\omega_{yi})$, and $E_y = (\nu + 0.5)\hbar\omega_{y1} + h_1$ denotes the y-eigenvalues. The matching conditions at $y = 0$ for the left and right domains yield the y-eigenvalues and the eigenfunctions $Y_\nu(y)$ (m is integer and ν is in general real).

The TCOM single-particle spectrum for a QDM made of two coupled (identical) QDs (with $\hbar\omega_x \hbar\omega_{y1} = \hbar\omega_{y2} = 3$ meV), plotted versus the distance, d, between the centers of the two dots, is given Fig. 32. In these calculations the height of the barrier between the dots varies as a function of d, thus simulating reduced coupling between them as they are separated; we take the barrier control parameter $\epsilon_1^b = \epsilon_2^b = 0.5$. In

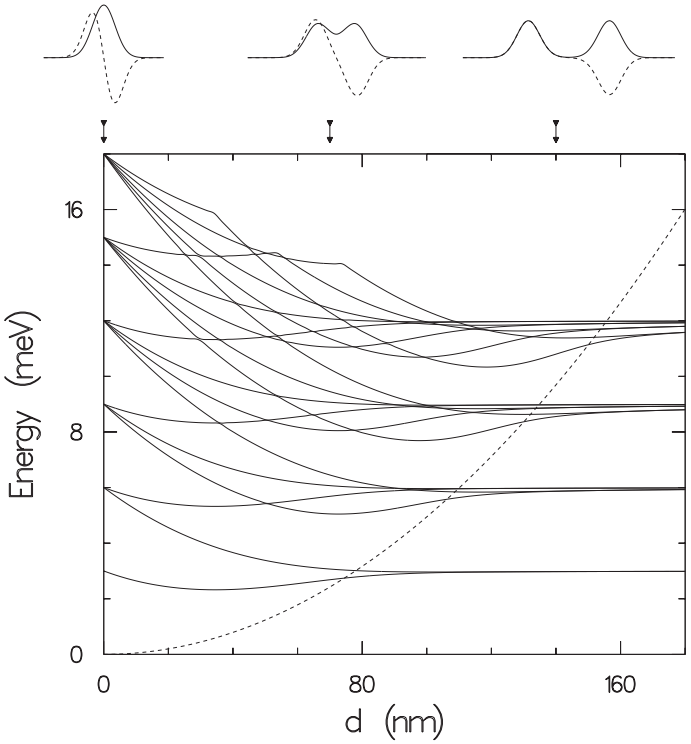

Figure 32: SE spectra of QDM's plotted versus the distance d between two (identical) coupled QD's with TCOM confinement $\hbar\omega_{y1} = \hbar\omega_{y2} = \hbar\omega_x = 3$ meV and $h_1 = h_2 = 0$. For all d's the barrier control parameters were taken as $\epsilon_1^b = \epsilon_2^b = 0.5$, i.e., the barrier height (depicted by the dashed line) varies as $V_b(d) = V_0(d)/2$. MO's correlating the united ($V_b = 0$) and separated-dots limits are denoted along with the corresponding (on the right) SQD states. Wavefunction cuts at $x = 0$ along the y-axis at several distances d (see arrows) corresponding to the lowest bonding and antibonding eigenvalues (solid and dashed lines) are displayed at the top. Energies in meV and distances in nm.

all our calculations, we used GaAs values, $m^* = 0.067m_e$ and a dielectric constant $\kappa = 12.9$; the scaled units which we use are 2 Ry$^* = m^*e^4/\hbar^2\kappa^2 = 10.96$ meV and $\mathrm{a}_B^* = \hbar^2\kappa/m^*e^2 = 10.188$ nm. For the SQD (large d) and the UQD ($d = 0$) limits the spectra are the same, corresponding to that of a 2D harmonic oscillator (two of them for the SQD) with a level degeneracy of 1, 2, 3, ... In analogy with real molecules, the states in the intermediate region ($d > 0$) may be interpreted as molecular orbitals (MO's) made of linear superpositions of the states of the two dots comprising the QDM. This description is intuitively appealing, though it is more appropriate for the weaker coupling regime (large d); nevertheless we continue to use it for the whole

range of coupling strength between the dots, including the strong coupling regime where reference to the states of the individual dots is only approximate. Thus, for example, as the two dots approach each other, the lowest levels (n_x, n_y) with $n_x = n_y = 0$ on the two dots may combine symmetrically ("bonding") or antisymmetrically ("antibonding") to form [0,0;0] and [0,0;1] MOs, with the third index denoting the total number of nodes of the MO along the interdot axis (y), that is, $2n_y + I$, $I = 0$ or 1; for symmetric combinations ($I = 0$) this index is even and for antisymmetric ones ($I = 1$) it is odd. Between the SQD and UQD limits the degeneracies of the individual dots' states are lifted, and in correlating these two limits the number of y-nodes is conserved; for example the [0,0;1] MO converts in the UD limit into the (0,1) state of a single QD, the [0,1;2] MO into the (0,2) state, and the [1,0;1] MO into the (1,1) state (see Fig. 32). Note that MOs of different symmetries may cross while they do not if they are of the same symmetry. The evolution of the $d = 70$ nm QDM spectrum as a function of V_b displayed in Fig. 33, shows that the level spectrum with $V_b = 0$, corresponding to a large non-circular dot, converges as the coupling is decreased (i.e., increasing V_b) into that of two separated dots; note however that even for large V_b the 2D harmonic oscillator spectrum is not recovered because of the unharmonicity introduced by the interdot barrier.

To explore the properties of QDM's in a magnetic field, we start first with a simple generalization of the non-interacting electrons's Darwin-Fock model. The SE spectra for the QDM ($d = 70$ nm, $V_b = 2.43$ meV) in a magnetic field (B) are shown in Fig. 34 (here we neglect the Zeeman interaction which is small for our range of B values with $g^* = -0.44$ for GaAs). The main features are: (i) the multiple crossings (and avoided crossings) as B increases, (ii) the decrease of the energy gap between levels, occurring in pairs (such as the lowest bonding-antibonding pair), portraying an effective reduced coupling between the QD's comprising the QDM as B increases, (see the electron densities for $B = 0$ and $B = 4$ T in Fig. 34). And (iii) the "condensation"

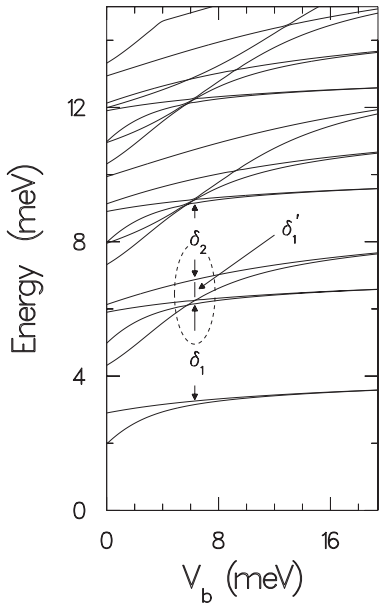

Figure 33: SE spectra of a QDM at $d = 70nm$ plotted versus the barrier height V_b.

of the spectrum into the sequence of Landau levels $(N_L + 1/2)\hbar\Omega_c$, $N_L = 0, 1, 2, ...$, similar to the behavior of the SE Darwin-Fock spectrum for harmonically confined electrons in a circular QD (note however that the geometry of the QDM is non-circular and deviates from a simple harmonic confinement).

3.3 The Many-Body Hamiltonian and the exact diagonalization method

The many-body hamiltonian $\mathcal{H}$ for a dimeric QDM comprising N electrons can be expressed as a sum of the single-particle part $H(i)$ defined in Eq. (3.1) and the two-particle interelectron Coulomb repulsion,

$$\mathcal{H} = \sum_{i=1}^{N} H(i) + \sum_{i=1}^{N} \sum_{j>i}^{N} \frac{e^2}{\kappa r_{ij}} \ , \tag{3.5}$$

where κ is the dielectric constant and r_{ij} denotes the relative distance between the i and j electrons.

As we mentioned in the introduction, we will use the method of exact diagonalization for determining the solution of the many-body problem specified by the

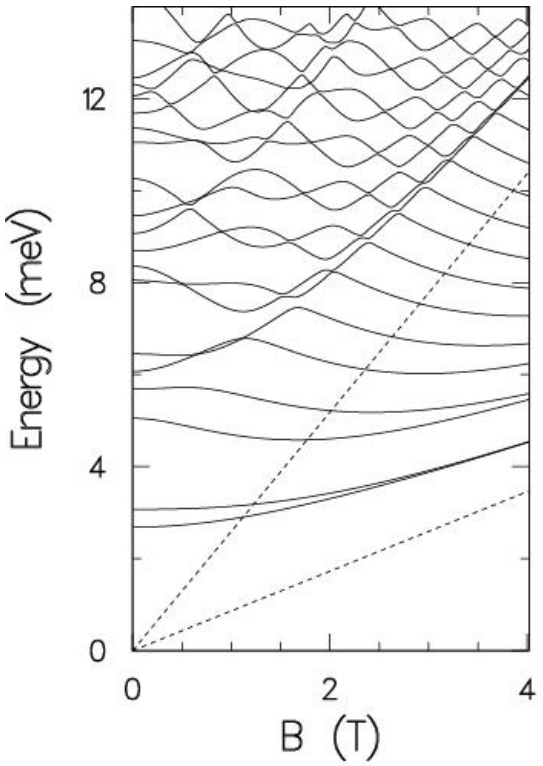

Figure 34: SE spectrum of the $d = 70$ nm ($\hbar\omega_{y1} = \hbar\omega_{y2} = \hbar\omega_x = 3$ meV, $V_b = 2.43$ meV, $\Delta h = 0$) QDM versus B (in T). The $\hbar\Omega_c/2$ and $3\hbar\Omega_c/2$ Landau levels are given by the dashed lines. The electron densities (shown as insets) for the lowest bonding (bottom) and antibonding (top) states at $B = 0$ and $B = 4$ T illustrate the contraction of the orbitals caused by the magnetic field, which underlines the field-induced decoupling of the dots ("QDM dissociation"). Contour values are in units of 3.571 10^{-4} nm^{-2}.

hamiltonian (3.5). In the EXD method, one writes the many-body wave function $\Phi_N^{\rm EXD}(\mathbf{r}_1, \mathbf{r}_2, \ldots, \mathbf{r}_N)$ as a linear superposition of Slater determinants $\Psi^N(\mathbf{r}_1, \mathbf{r}_2, \ldots, \mathbf{r}_N)$ that span the many-body Hilbert space and are constructed out of the single-particle *spin-orbitals*

$$\chi_j(x, y) = \varphi_j(x, y)\alpha, \quad \text{if} \quad 1 \leq j \leq K, \tag{3.6}$$

and

$$\chi_j(x, y) = \varphi_{j-K}(x, y)\beta, \quad \text{if} \quad K < j \leq 2K, \tag{3.7}$$

where $\alpha(\beta)$ denote up (down) spins. Namely

$$\Phi_{N,p}^{\rm EXD}(\mathbf{r}_1, \ldots, \mathbf{r}_N) = \sum_I C_I^p \Psi_I^N(\mathbf{r}_1, \ldots, \mathbf{r}_N), \tag{3.8}$$

where

$$\Psi_I^N = \frac{1}{\sqrt{N!}} \begin{vmatrix} \chi_{j_1}(\mathbf{r}_1) & \dots & \chi_{j_N}(\mathbf{r}_1) \\ \vdots & \ddots & \vdots \\ \chi_{j_1}(\mathbf{r}_N) & \dots & \chi_{j_N}(\mathbf{r}_N) \end{vmatrix}, \tag{3.9}$$

and the master index I counts the number of arrangements $\{j_1, j_2, \dots, j_N\}$ under the restriction that $1 \leq j_1 < j_2 < \dots < j_N \leq 2K$. Of course, $p = 1, 2, \dots$ counts the excitation spectrum, with $p = 1$ corresponding to the ground state.

The exact diagonalization of the many-body Schrödinger equation

$$\mathcal{H}\Phi_{N,p}^{\mathrm{EXD}} = E_{N,p}^{\mathrm{EXD}}\Phi_{N,p}^{\mathrm{EXD}} \tag{3.10}$$

transforms into a matrix diagonalizatiom problem, which yields the coefficients C_I^p and the EXD eigenenergies $E_{N,p}^{\mathrm{EXD}}$.

The matrix elements $\langle\Psi_N^I|\mathcal{H}|\Psi_N^J\rangle$ between the basis determinants [see Eq.(3.9)] are calculated using the Slater rules [58]. Naturally, an important ingredient in this respect are the two-body matrix elements of the Coulomb interaction,

$$\frac{e^2}{\kappa}\int_{-\infty}^{\infty}\int_{-\infty}^{\infty} d\mathbf{r}_1 d\mathbf{r}_2 \varphi_i^*(\mathbf{r}_1)\varphi_j^*(\mathbf{r}_2)\frac{1}{|\mathbf{r}_1 - \mathbf{r}_2|}\varphi_k(\mathbf{r}_1)\varphi_l(\mathbf{r}_2), \tag{3.11}$$

in the basis formed out of the single-particle spatial orbitals $\varphi_i(\mathbf{r})$, $i = 1, 2, \dots, K$. In our approach, these matrix elements are determined numerically.

3.4 The spin states

The spin operators corresponding to x, y, z components for one electron can be represented by two-dimensional Hermitian matrices:

$$\mathbf{S}_x = \frac{1}{2}\begin{pmatrix} 0 & 1 \\ 1 & 0 \end{pmatrix}, \quad \mathbf{S}_y = \frac{1}{2}\begin{pmatrix} 0 & -i \\ i & 0 \end{pmatrix}, \quad \mathbf{S}_z = \frac{1}{2}\begin{pmatrix} 1 & 0 \\ 0 & -1 \end{pmatrix} \tag{3.12}$$

The square of the spin is represented by the operator:

$$\mathbf{S}^2 = \mathbf{S}_x^2 + \mathbf{S}_y^2 + \mathbf{S}_z^2 = \frac{3}{4}\begin{pmatrix} 1 & 0 \\ 0 & 1 \end{pmatrix} \tag{3.13}$$

For N electrons,

$$\mathbf{S} = \mathbf{S}_1 + \mathbf{S}_2 + ... + \mathbf{S}_N \tag{3.14}$$

therefore,

$$\mathbf{S}_x = \mathbf{S}_{1x} + \mathbf{S}_{2x} + ... + \mathbf{S}_{Nx}; \tag{3.15}$$

$$\mathbf{S}_y = \mathbf{S}_{1y} + \mathbf{S}_{2y} + ... + \mathbf{S}_{Ny}; \tag{3.16}$$

$$\mathbf{S}_z = \mathbf{S}_{1z} + \mathbf{S}_{2z} + ... + \mathbf{S}_{Nz}. \tag{3.17}$$

It can be proved that operator $\mathbf{S}^2$ commutes with each of the three operators $\mathbf{S}_x$, $\mathbf{S}_y$, $\mathbf{S}_z$. Then, $\mathbf{S}^2$ and $\mathbf{S}_z$ have simultaneous eigenfunctions:

$$\mathbf{S}^2 Y(s,m) = kY(s,m) \tag{3.18}$$

$$\mathbf{S}_z Y(s,m) = mY(s,m). \tag{3.19}$$

It's very useful to define two additional operators:

$$\mathbf{S}_+ = \mathbf{S}_x + i\mathbf{S}_y = \begin{pmatrix} 0 & 1 \\ 0 & 0 \end{pmatrix}, \quad \mathbf{S}_- = \mathbf{S}_x - i\mathbf{S}_y = \begin{pmatrix} 0 & 0 \\ 1 & 0 \end{pmatrix}. \tag{3.20}$$

If we follow Dirac's convention by choosing the phase factor to be 1, then

$$\mathbf{S}_+ Y(s,m) = [(s-m)(s+m+1)]^{\frac{1}{2}} Y(s,m+1) \tag{3.21}$$

$$\mathbf{S}_- Y(s,m) = [(s+m)(s-m+1)]^{\frac{1}{2}} Y(s,m-1) \tag{3.22}$$

A basic property of spin eigenfunctions is that they exhibit degeneracies for $N > 2$, i.e., there may be more than one linearly independent (and orthogonal) spin functions that are simultaneous eigenstates of both $\hat{\mathbf{S}}^2$ and S_z. These degeneracies are usually visualized by means of the *branching diagram*. The axes in this plot describe the number N of fermions (horizontal axis) and the quantum number S of the total spin (vertical axis). At each point (N, S), a circle is drawn containing the number $g(N, S)$ which gives the degeneracy of spin states. It is found[42] that

$$g(N,S) = \begin{pmatrix} N \\ N/2 - S \end{pmatrix} - \begin{pmatrix} N \\ N/2 - S - 1 \end{pmatrix}. \tag{3.23}$$

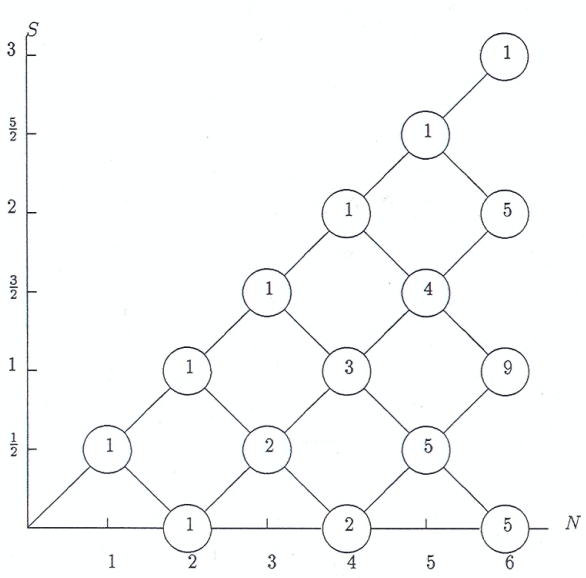

Figure 2.3. Branching diagram.

Figure 35: The branching diagram for the spin degeneracies.

We see from the figure that the highest spin state is always non-degenerate. The number of independent spin states increases sharply as N increases.

3.4.1 Two electrons

In the case of zero magnetic field and for a small number of particles, one can find compact expressions that encompass all possible superpositions. For two electrons, define $\mathbf{S} = \mathbf{S}_1 + \mathbf{S}_2$, then

$$\mathbf{S}_x = \mathbf{S}_{1x} + \mathbf{S}_{2x}, \mathbf{S}_y = \mathbf{S}_{1y} + \mathbf{S}_{2y}, \mathbf{S}_z = \mathbf{S}_{1z} + \mathbf{S}_{2z}. \tag{3.24}$$

A two-electron system has four basic state,

$$|\uparrow\uparrow\rangle\,, \quad |\downarrow\downarrow\rangle\,, \quad |\uparrow\downarrow\rangle\,, \quad |\downarrow\uparrow\rangle\,. \tag{3.25}$$

We can construct the eigenfunctions of $\mathbf{S}^2$ and $\mathbf{S}_z$ by these four states, the solutions are

$$Y_{11} = |\uparrow\uparrow\rangle \tag{3.26}$$

$$Y_{10} = \sqrt{\frac{1}{2}}\,(\,|\uparrow\downarrow\rangle + |\downarrow\uparrow\rangle\,) \tag{3.27}$$

$$Y_{1-1} = |\downarrow\downarrow\rangle \tag{3.28}$$

$$Y_{00} = \sqrt{\frac{1}{2}}\,(\,|\uparrow\downarrow\rangle - |\downarrow\uparrow\rangle\,) \tag{3.29}$$

We call $Y(s,m)$ with $s=1$ triplet state, and $s=0$ singlet state.

3.4.2 Three electrons

Let us construct the spin function with $S=1/2$ [57]. The basic terms for $M=1/2$ are

$$|1\rangle = |\uparrow\uparrow\downarrow\rangle\,,\;\; |2\rangle = |\uparrow\downarrow\uparrow\rangle\,,\;\; |3\rangle = |\downarrow\uparrow\uparrow\rangle\,, \tag{3.30}$$

where the particle indices are assumed to be in increasing order, e.g. in the sate $|1\rangle$ the first and second electrons are in a spin-up state while the third electron is in a spin-down state. The general spin function in this case can be expressed as

$$Y_{ss}(\lambda) = \sum_{i=3}^{3} \lambda_i\,|i\rangle\,. \tag{3.31}$$

The coefficients $(\lambda_1,\lambda_2,\lambda_3)$, characterizing the spin functions, are not independent of each other but must satisfy the condition, $\mathbf{S}_+ Y_s s(\lambda) = 0$, , which leads to the condition of $\lambda_1+\lambda_2+\lambda_3 = 0$. By taking account of the normalization the spin function can be parameterized by a single variable $\theta(-\pi/2 \leqslant \theta \leqslant \pi/2$ as follows:

$$Y_{\frac{1}{2}\frac{1}{2}} = \sqrt{\frac{2}{3}}\sin\theta\,|\uparrow\uparrow\downarrow\rangle + \left(\sqrt{\frac{1}{2}}\cos\theta - \sqrt{\frac{1}{6}}\sin\theta\right)|\uparrow\downarrow\uparrow\rangle - \left(\sqrt{\frac{1}{2}}\cos\theta + \sqrt{\frac{1}{6}}\sin\theta\right)|\downarrow\uparrow\uparrow\rangle\,. \tag{3.32}$$

The θ value is chosen such that $\theta = 0$ corresponds to the spin function with the intermediate spin $S_{12}=0$ whereas $\theta = \pm\pi/2$ to the one with $S_{12}=1$.

By acting with $\mathbf{S}_-$ on this equation, we obtain

$$Y_{\frac{1}{2}-\frac{1}{2}} = -\sqrt{\frac{2}{3}}\sin\theta\,|\downarrow\downarrow\uparrow\rangle - \left(\sqrt{\frac{1}{2}}\cos\theta - \sqrt{\frac{1}{6}}\sin\theta\right)|\downarrow\uparrow\downarrow\rangle + \left(\sqrt{\frac{1}{2}}\cos\theta + \sqrt{\frac{1}{6}}\sin\theta\right)|\uparrow\downarrow\downarrow\rangle\,. \tag{3.33}$$

3.4.3 Four electron spin function

Specifically for $N = 4$ particles, there is one spin eigenfunction with $S = 2$, three with $S = 1$, and two with $S = 0$. In general the spin part of the EXD wave functions involves a linear superposition over all the degenerate spin eigenfunctions for a given S.

For $N = 4$ and $S = 0$, $S_z = 0$ one has:

$$\begin{aligned}\mathcal{X}_{00} &= \sqrt{\frac{1}{3}}\sin\theta|\uparrow\uparrow\downarrow\downarrow\rangle + (\frac{1}{2}\cos\theta - \sqrt{\frac{1}{12}}\sin\theta)\,|\uparrow\downarrow\uparrow\downarrow\rangle \\ &\quad -(\frac{1}{2}\cos\theta + \sqrt{\frac{1}{12}}\sin\theta)|\uparrow\downarrow\downarrow\uparrow\rangle \\ &\quad -(\frac{1}{2}\cos\theta + \sqrt{\frac{1}{12}}\sin\theta)\,|\downarrow\uparrow\uparrow\downarrow\rangle \\ &\quad +(\frac{1}{2}\cos\theta - \sqrt{\frac{1}{12}}\sin\theta)\,|\downarrow\uparrow\downarrow\uparrow\rangle + \sqrt{\frac{1}{3}}\sin\theta\,|\downarrow\downarrow\uparrow\uparrow\rangle\,,\end{aligned} \tag{3.34}$$

where the parameter θ satisfies $-\pi/2 \leq \theta \leq \pi/2$ and is chosen such that $\theta = 0$ corresponds to the intermediate spin function with $S_{12} = 0$(two electron); $S_{123} = 1/2$(three electron); whereas $\theta = \pm\pi/2$ corresponds to the one with $S_{12} = 1$, $S_{123} = 1/2$.

For $N = 4$ and $S = 1$, $S_z = 0$ one has:

$$\begin{aligned}
\mathcal{X}_{10} \;=\; & \\
& (\sqrt{\frac{1}{6}}\sin\theta\sin\varphi - \sqrt{\frac{1}{12}}\sin\theta\cos\varphi - \frac{1}{2}\cos\theta)\,|\downarrow\uparrow\uparrow\downarrow\rangle \\
& +(\sqrt{\frac{1}{6}}\sin\theta\sin\varphi - \sqrt{\frac{1}{12}}\sin\theta\cos\varphi + \frac{1}{2}\cos\theta)\,|\uparrow\downarrow\uparrow\downarrow\rangle \\
& +(\sqrt{\frac{1}{12}}\sin\theta\cos\varphi - \sqrt{\frac{1}{6}}\sin\theta\sin\varphi - \frac{1}{2}\cos\theta)\,|\downarrow\uparrow\downarrow\uparrow\rangle \\
& +(\sqrt{\frac{1}{12}}\sin\theta\cos\varphi - \sqrt{\frac{1}{6}}\sin\theta\sin\varphi + \frac{1}{2}\cos\theta)\,|\uparrow\downarrow\downarrow\uparrow\rangle \\
& +(\sqrt{\frac{1}{6}}\sin\theta\sin\varphi + \sqrt{\frac{1}{3}}\sin\theta\cos\varphi)\,|\uparrow\uparrow\downarrow\downarrow\rangle \\
& -(\sqrt{\frac{1}{6}}\sin\theta\sin\varphi + \sqrt{\frac{1}{3}}\sin\theta\cos\varphi)\,|\downarrow\downarrow\uparrow\uparrow\rangle\,,
\end{aligned} \tag{3.35}$$

where the parameters θ and φ satisfy $-\pi/2 \leq \theta \leq \pi/2$ and $-\pi/2 \leq \varphi \leq \pi/2$. The three independent spin functions with definite S_{12} and S_{123} values correspond to the θ and φ values as follows: for $S_{12} = 0$ and $S_{123} = 1/2$, $\theta = 0$; for $S_{12} = 1$ and $S_{123} = 1/2$, $\theta = \pm\pi/2$ and $\varphi = 0$; and for $S_{12} = 1$ and $S_{123} = 3/2$, $\theta = \pm\pi/2$ and $\varphi = \pm\pi/2$.

Finally, for $N = 4$ and $S = 2$, $S_z = 0$ (maximum polarization) case, one has:

$$\begin{aligned}
\mathcal{X}_{20} \;=\; & \\
& \frac{|\downarrow\downarrow\uparrow\uparrow\rangle + |\downarrow\uparrow\downarrow\uparrow\rangle + |\downarrow\uparrow\uparrow\downarrow\rangle + |\uparrow\downarrow\downarrow\uparrow\rangle + |\uparrow\downarrow\uparrow\downarrow\rangle + |\uparrow\uparrow\downarrow\downarrow\rangle}{\sqrt{6}}.
\end{aligned} \tag{3.36}$$

3.4.4 N electrons

The spin function of the N-electron system cannot be uniquely specified by the total spin S alone. One elementary way to construct it is to use a successive coupling of the spins of the particles. The intermediate spin quantum numbers S_{12}, S_{123}, etc., appearing in the successive coupling serve to specify the spin function. They do not, however, constitute good quantum numbers in general and thus several sets of t he

spin quantum numbers may be needed to obtain a good wave function. The order of the spin coupling in the successive couplings is fixed and in general does not naturally follow the choice of the relative coordinates. We are not going to detail how to get the N-electron spin functions but you can refer to the branching diagram to learn more about it.

3.5 CONSERVATION OF PARITY

Of great help in reducing the size of the matrices to be digitalized is the fact that the parity (with respect to the origin) of the EXD many-body wave function is a good quantum number for all values of the magnetic field when $h_1 = h_2$. Specifically, the xy-parity operator associated with reflections about the origin of the axes is defined as

$$\hat{\mathcal{P}}_{xy}\Phi^{\mathrm{EXD}}_{N,q}(\mathbf{r}_1,\mathbf{r}_2,\mathbf{r}_3,\mathbf{r}_4) = \Phi^{\mathrm{EXD}}_{N,q}(-\mathbf{r}_1,-\mathbf{r}_2,-\mathbf{r}_3,-\mathbf{r}_4) \tag{3.37}$$

and has eigenvalues ± 1.

One can also consider partial parity operators $\hat{\mathcal{P}}_x$ and $\hat{\mathcal{P}}_y$ associated solely with reflections about the x and y axis, respectively; of course $\hat{\mathcal{P}}_{xy} = \hat{\mathcal{P}}_x\hat{\mathcal{P}}_y$. We note that unlike $\hat{\mathcal{P}}_{xy}$, the partial parities $\hat{\mathcal{P}}_x$ and $\hat{\mathcal{P}}_y$ are conserved only for zero magnetic fields ($B = 0$). With the two-center oscillator *cartesian* basis that we use [see Eq. (3.3)], it is easy to calculate the parity eigenvalues for the Slater determinants, Eq. (3.9), that span the many-body Hilbert space. Because $X_\mu(x)$ and $Y_n(y)$ conserve the partial $\hat{\mathcal{P}}_x$ and $\hat{\mathcal{P}}_y$ parities, respectively, one finds:

$$\hat{\mathcal{P}}_{xy}\Psi^N_I = (-)^{\sum_{i=1}^4 m_i+n_i}\Psi^N_I, \tag{3.38}$$

where m_i and n_i count the number of single-particle states associated with the bare two-center oscillator [see the auxiliary hamiltonian H_0 in Eq. (3.4)] along the x axis and the simple oscillator along the y direction (with the assumption that the lowest states have $m = 0$ and $n = 0$, since they are even states). We note again that the

index μ in Eq. (3.3) is not an integer in general, while m here is indeed an integer (since it counts the number of single-particle states along the x direction).

CHAPTER IV

RESULTS OF FOUR-ELECTRON DOUBLE QUANTUM DOTS

4.1 Results: Energy Spectra

The excitation spectra as a function of the applied magnetic field for four electrons in a double QD with interdot distance $d = 2x_2 = -2x_1 = 30$ nm and no voltage bias between the dots ($h_1 = h_2 = 0$) are plotted for three different strengths of interelectron repulsion, i.e., weak [$\kappa = 12.5$ (GaAs); see Fig. 36], intermediate ($\kappa = 6$; see Fig. 37), and strong ($\kappa = 2$; see Fig. 38) Coulomb repulsion. The interdot barrier parameter was taken $\epsilon^b = 0.5$ (because $h_1 = h_2 = 0$, one has $\epsilon_1^b = \epsilon_2^b = \epsilon^b$; see previous section for the definitions). In all cases, we calculated the eight lowest energy levels.

We observe that the lowest six levels form a band that separates through the opening of a gap from the rest of the spectrum. This happens already at a weak repulsion, and it is well developed for the intermediate case ($\kappa = 6$). It is of interest to note that the number six coincides with the total number of spin eigenfunctions for $N = 4$ fermions, as can be seen from the branching diagram displaying the spin degeneracies [42] . In particular, there is one level with total spin $S = 2$ (and parity $\mathcal{P}_{xy} = 1$), three levels with total spin $S = 1$ (two with $\mathcal{P}_{xy} = 1$ and one with $\mathcal{P}_{xy} = -1$), and two levels with total spin $S = 0$ (one with $\mathcal{P}_{xy} = 1$ and the second with $\mathcal{P}_{xy} = -1$). All these six levels approximately cross at one point situated at about $B \approx 3.5$ T for $\kappa = 12.5$ and $B \approx 2.2$ T for $\kappa = 6$.

These trends associated with the opening of a gap and the formation of a six-state low band appear further reinforced for the larger interdot distance of $d = 60$ nm

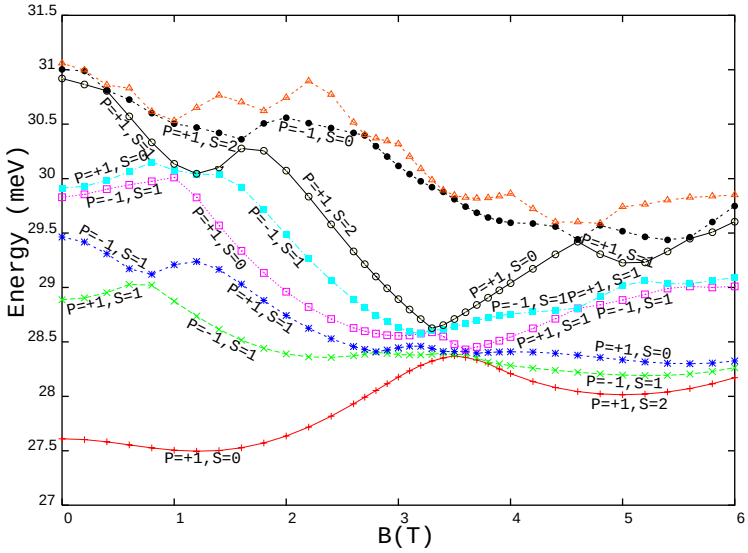

Figure 36: Energy spectra (as a function of the magnetic field B) for $N = 4$ electrons in a double quantum dot with interdot separation $d = 30$ nm. Case of weak interelectron repulsion corresponding to GaAs ($\kappa = 12.5$). The calculation were done for the case $S_z = 0$ and the Zeeman term was neglected. In this case all states with the same total spin S and different spin projections S_z are degenerate. The effect of the Zeeman term can be easily added. Remaining parameters: $\epsilon^b = 0.5$, $m^* = 0.07m_e$, $K = 50$. Energies are referenced to $N\hbar\sqrt{\omega_0^2 + \omega_c^2/4}$, where $\omega_c = eB/(m^*c)$ is the cyclotron frequency.

(displayed in Figs. 39 − 41 for the three cases of $\kappa = 12.5$, 6, and 2, respectively. It is remarkable that the six lower curves cross now at a sharply defined point (situated at $B \approx 3.3$ T for $\kappa = 12.5$ and $B \approx 2.1$ T for $\kappa = 6$. The six curves demonstrate additional near degeneracies regrouping approximately to three curves before and after the crossing point, which results in a remarkable simplification of the spectrum.

For strong repulsion ($\kappa = 2$), all six states in the low band are practically degenerate for both distances ($d = 30$ nm ; see Fig. 38 and $d = 60$ nm; see Fig. 41). This is a consequence of the formation of a near-rigid Wigner molecule with strongly localized electrons. Namely, the overlap between the orbitals of localized electrons are practically zero (see, e.g., Ref. [70]), yielding a vanishing exchange [73], and thus all six possible spin multiplicities become degenerate in energy. Furthermore the physical

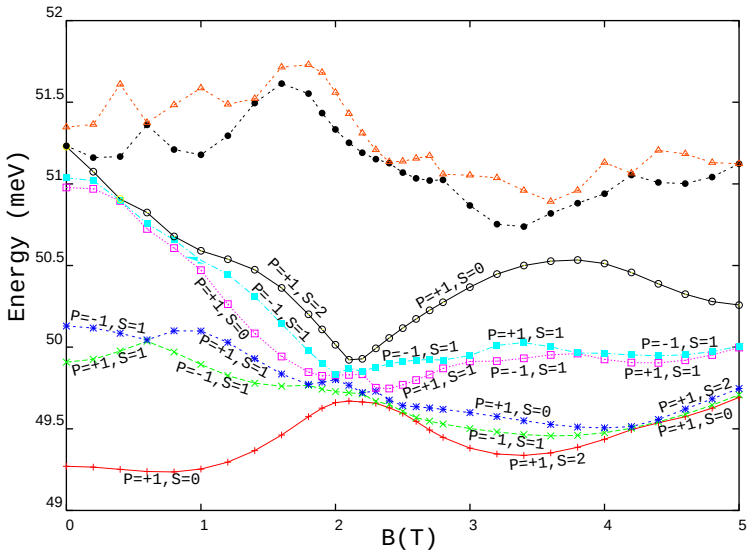

Figure 37: Energy spectra (as a function of the magnetic field B) for $N = 4$ electrons in a double quantum dot with interdot separation $d = 30$ nm. Case of intermediate interelectron repulsion ($\kappa = 6$). Remaining parameters: $\epsilon^b = 0.5$, $m^* = 0.07m_e$, $K = 50$. Energies are referenced to $N\hbar\sqrt{\omega_0^2 + \omega_c^2/4}$, where $\omega_c = eB/(m^*c)$ is the cyclotron frequency.

picture of a near-rigid Wigner molecule suggests that the energy gap to the next band of states corresponds to the excitation of the lowest stretching vibrational mode of the 4-electron molecule.

It is natural to anticipate at this point that the above behavior at low B can be generalized to an arbitrary number of electrons N in a double QD. Namely, as the strength of the interelectron interaction increases, a low-energy band comprising all possible spin multiplicities will form and it will become progressively well separated by an energy gap from the higher excitations. For example, for $N = 6$, an inspection of the branching diagram in leads us to the prediction that there will be 20 states in this low-energy band. A similar behavior emerges also in the case of a *single*, but strongly *anisotropic* quantum dot; indeed a low-energy band of three states (see the branching diagram) was found for $N = 3$ electrons in Ref. [77].

It is of interest to contrast the above behavior of the excitation spectra in a double QD to that of a N-electron circular dot. Specifically, in the circular QD, large

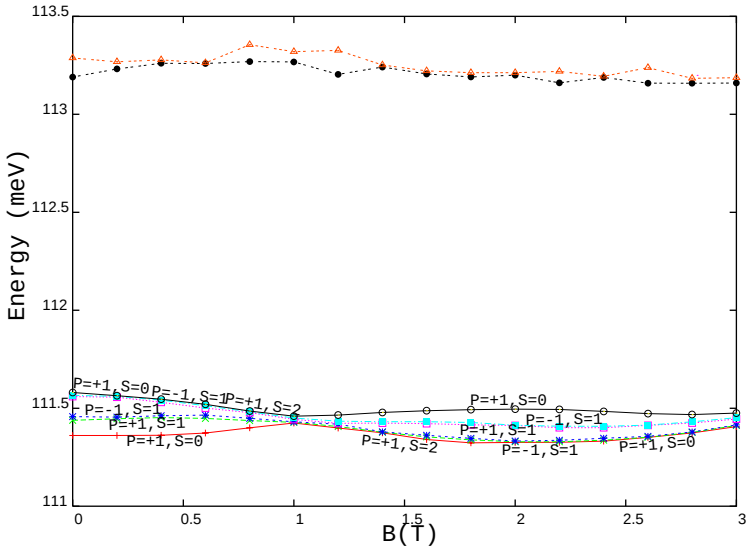

Figure 38: Energy spectra (as a function of the magnetic field B) for $N = 4$ electrons in a double quantum dot with interdot separation $d = 30$ nm. Case of strong interelectron repulsion ($\kappa = 2$). Remaining parameters: $\epsilon^b = 0.5$, $m^* = 0.07m_e$, $K = 50$. Energies are referenced to $N\hbar\sqrt{\omega_0^2 + \omega_c^2/4}$, where $\omega_c = eB/(m^*c)$ is the cyclotron frequency.

inetelectron repulsion leads to formation of a near-rigid *rotating* Wigner molecule that exhibits a rigid moment of inertia. Then the states inside the low-energy band (two states for $N = 2$, three for $N = 3$, six for $N = 4$, etc.) do not become degenerate in energy, but form an yrast rotational band [75] specified by $L^2/2\mathcal{J}_0$, where L is the total angular momentum and $\mathcal{J}_0$ is the classical moment of inertia. We note that the energy splittings among the yrast rotational states are much smaller than the vibrational energy gap in circular dots associated with the quantum of energy $\sqrt{3}\hbar\omega_0$ of the stretching (often referred to also as breathing) mode of the polygonal-ring configuration of the quasiclassical Wigner molecule. [71, 56, 16]

4.2 Results: Electron densities

The electron density is the expectation value of the one-body operator

$$\hat{\rho}(\mathbf{r}) = \sum_{i=1}^{N} \delta(\mathbf{r} - \mathbf{r}_i), \tag{4.1}$$

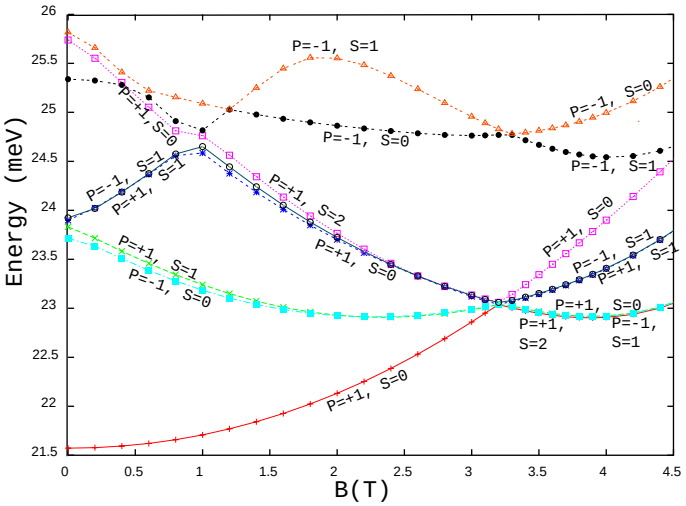

Figure 39: Energy spectra (as a function of the magnetic field B) for $N = 4$ electrons in a double quantum dot with interdot separation $d = 60$ nm. Case of weak interelectron repulsion corresponding to GaAs ($\kappa = 12.5$). Remaining parameters: $\epsilon^b = 0.5$, $m^* = 0.07m_e$, $K = 50$. Energies are referenced to $N\hbar\sqrt{\omega_0^2 + \omega_c^2/4}$, where $\omega_c = eB/(m^*c)$ is the cyclotron frequency.

that is:

$$\begin{aligned} \rho(\mathbf{r}) &= \langle \Phi^{\rm EXD}_{N,q} | \hat{\rho}(\mathbf{r}) | \Phi^{\rm EXD}_{N,q} \rangle \\ &= \sum_{I,J} C^{q*}_I C^q_J \langle \Psi^N_I | \hat{\rho}(\mathbf{r}) | \Psi^N_J \rangle . \end{aligned} \tag{4.2}$$

Since $\hat{\rho}(\mathbf{r})$ is a one-body operator, it connects only Slater determinants Ψ^N_I and Ψ^N_J that differ at most by one spin orbital $\chi_j(\mathbf{r})$; for the corresponding Slater rules for calculating matrix elements between determinants for two-body operators in terms of spin orbitals, see Table 2.3 in Ref. [58].

In Figs. 42, 43 and 44, we display the electron densities for for $N = 4$ electrons in the case of a double dot at zero magnetic field with interdot separation $d = 30$ nm.

In Figs. 45, 46, and 47 we display the electron densities for $N = 4$ electrons in the case of a double dot at zero magnetic field with interdot separation $d = 60$ nm.

For the weak interaction case ($\kappa = 12.5$) at $B = 0$, the electron densities do not exhibit clear signatures of formation of a Wigner molecule for either interdot distance, $d = 30$ nm (Fig. 42) or $d = 60$ nm (Fig. 45). The Wigner molecule is well formed,

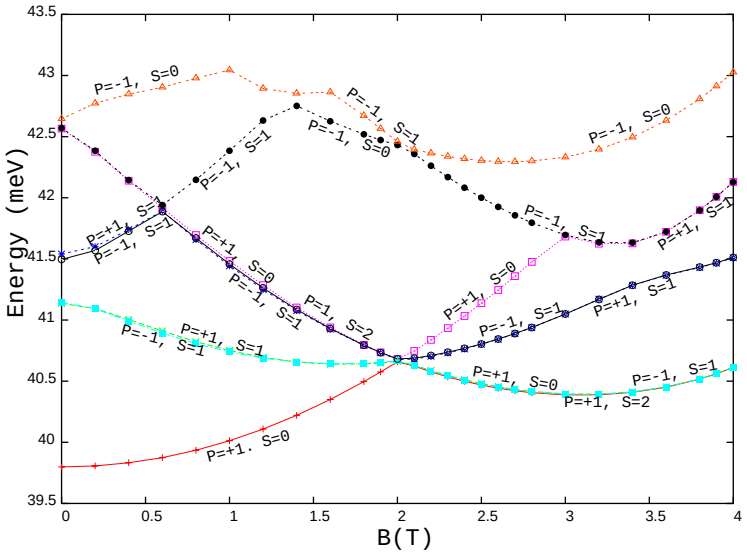

Figure 40: Energy spectra (as a function of the magnetic field B) for $N = 4$ electrons in a double quantum dot with interdot separation $d = 60$ nm. Case of intermediate interelectron repulsion ($\kappa = 6$). Remaining parameters: $\epsilon^b = 0.5$, $m^* = 0.07m_e$, $K = 50$. Energies are referenced to $N\hbar\sqrt{\omega_0^2 + \omega_c^2/4}$, where $\omega_c = eB/(m^*c)$ is the cyclotron frequency.

however, in the case of the intermediate Coulomb repulsion ($\kappa = 6$; see Fig. 46 with $d = 60$ nm). One observes indeed four humps that correspond to the four localized electrons; they are located at (± 34.88 nm, ± 13.13 nm). In the case of strong Coulomb repulsion ($\kappa = 2$) and for the same interdot distance $d = 60$ nm, the electrons are further localized as can be seen from Fig. 47; the four humps occur now at (± 39.86 nm, ± 21.02 nm). The Wigner molecule is also well formed in the the strong-repulsion and $d = 30$ nm case, as can be seen from Fig. 44, with the localized electrons located at (± 29.28 nm, ± 21.11 nm).

4.3 Results: Spin-resolved conditional probability distributions at $B = 0$

4.3.1 Definitions

In the regime corresponding to a well-defined Wigner molecule, the electron densities are characterized by four humps that reflect the localization of the four electrons

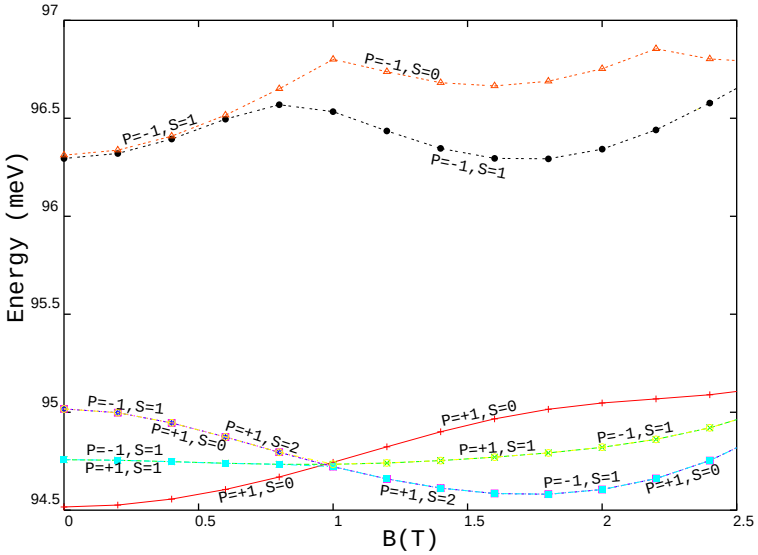

Figure 41: Energy spectra (as a function of the magnetic field B) for $N = 4$ electrons in a double quantum dot with interdot separation $d = 60$ nm. Case of strong repulsion ($\kappa = 2$). Remaining parameters: $\epsilon^b = 0.5$, $m^* = 0.07m_e$, $K = 50$. Energies are referenced to $N\hbar\sqrt{\omega_0^2 + \omega_c^2/4}$, where $\omega_c = eB/(m^*c)$ is the cyclotron frequency.

in the double quantum dot. Such charge densities do not provide any information concerning the spin structure of each EXD state. In fact, all six EXD states in the lower band exhibit very similar four-humped electron densities.

The spin configurations associated with a given (S, S_z) EXD state in the WM regime can be investigated with the help of the spin-resolved two-point anisotropic correlation function defined as:

$$P_{\sigma\sigma_0}(\mathbf{r}, \mathbf{r}_0) = \langle \Phi^{\mathrm{EXD}}_{N,q} | \sum_{i \neq j} \delta(\mathbf{r} - \mathbf{r}_i)\delta(\mathbf{r}_0 - \mathbf{r}_j)\delta_{\sigma\sigma_i}\delta_{\sigma_0\sigma_j} | \Phi^{\mathrm{EXD}}_{N,q} \rangle, \tag{4.3}$$

with the EXD many-body wave function given by Equation [3.8].

Using a normalization constant

$$\mathcal{N}(\sigma, \sigma_0, \mathbf{r}_0) = \int P_{\sigma\sigma_0}(\mathbf{r}, \mathbf{r}_0) d\mathbf{r}, \tag{4.4}$$

we further define a related conditional probability distribution (CPD) as

$$\mathcal{P}_{\sigma\sigma_0}(\mathbf{r}, \mathbf{r}_0) = P_{\sigma\sigma_0}(\mathbf{r}, \mathbf{r}_0)/\mathcal{N}(\sigma, \sigma_0, \mathbf{r}_0), \tag{4.5}$$

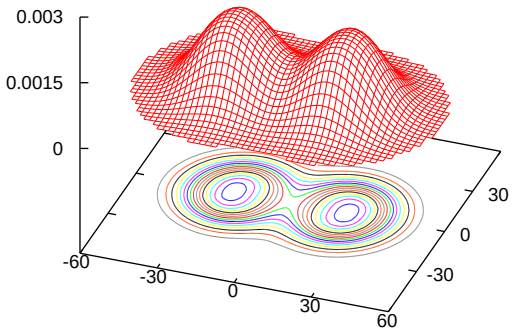

Figure 42: Electron densities at $B = 0$ for the ground state (with $S = 0, S_z = 0$, parity $P_{xy} = 1$, and energy $E = 27.609$ meV) of $N = 4$ electrons in a double quantum dot with interdot separation $d = 30$ nm. Case of weak Coulomb repulsion ($\kappa = 12.5$). Remaining parameters: $\epsilon^b = 0.5$, $m^* = 0.07m_e$, $K = 50$. Distances in nm. Vertical axis in arbitrary units (with the same scale for the two figures 42 and 44).

having the property $\int \mathcal{P}_{\sigma\sigma_0}(\mathbf{r}, \mathbf{r}_0)d\mathbf{r} = 1$. The spin-resolved CPD gives the spatial probability distribution of finding a second electron with spin projection σ under the condition that another electron is located (fixed) at $\mathbf{r}_0$ with spin projection σ_0; σ and σ_0 can be either up ($\uparrow$) or down ($\downarrow$).

To calculate $P_{\sigma\sigma_0}(\mathbf{r}, \mathbf{r}_0)$ in Eq.[4.3], we use a symmetrized operator

$$\begin{aligned}\hat{T}_{\sigma\sigma_0}(\mathbf{r}, \mathbf{r}_0) = \\ \sum_{i<j} \big[\delta(\mathbf{r} - \mathbf{r}_i)\delta(\mathbf{r}_0 - \mathbf{r}_j)\delta_{\sigma\sigma_i}\delta_{\sigma_0\sigma_j} + \\ \delta(\mathbf{r} - \mathbf{r}_j)\delta(\mathbf{r}_0 - \mathbf{r}_i)\delta_{\sigma\sigma_j}\delta_{\sigma_0\sigma_i}\big], \end{aligned} \tag{4.6}$$

yielding

$$\begin{aligned} P_{\sigma\sigma_0}(\mathbf{r}, \mathbf{r}_0) &= \langle \Phi^{\mathrm{EXD}}_{N,q} | \hat{T} | \Phi^{\mathrm{EXD}}_{N,q} \rangle \\ &= \sum_{I,J} C^{q*}_I C^q_J \langle \Psi^N_I | \hat{T} | \Psi^N_J \rangle. \end{aligned} \tag{4.7}$$

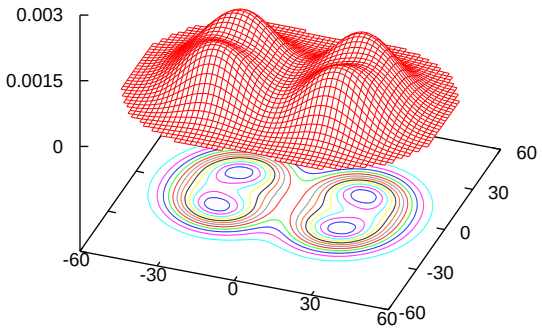

Figure 43: Electron densities at $B = 0$ for the ground state (with $S = 0, S_z = 0$, parity $P_{xy} = 1$, and energy $E = 49.271$ meV) of $N = 4$ electrons in a double quantum dot with interdot separation $d = 30$ nm. Case of intermediate Coulomb repulsion ($\kappa = 6$). Remaining parameters: $\epsilon^b = 0.5$, $m^* = 0.07 m_e$. Distances in nm. Vertical axis in arbitrary units (with the same scale for the two figures 42 and 44).

Since $\hat{T}_{\sigma\sigma_0}(\mathbf{r}, \mathbf{r}_0)$ is a two-body operator, it connects only Slater determinants Ψ_I^N and Ψ_J^N that differ at most by *two* spin orbitals $\chi_{j_1}(\mathbf{r})$ and $\chi_{j_2}(\mathbf{r})$; for the corresponding Slater rules for calculating matrix elements between determinants for two-body operators in terms of spin orbitals, see Table 2.4 in Ref. [58].

4.3.2 Examples of $S = 0$, $S_z = 0$ EXD states

For each charge density, one can plot four different spin-resolved CPDs, i.e.,$\mathcal{P}_{\uparrow\uparrow}$, $\mathcal{P}_{\uparrow\downarrow}$, $\mathcal{P}_{\downarrow\uparrow}$, and $\mathcal{P}_{\downarrow\downarrow}$. This can potentially lead to a very large number of time consuming computations and a large number of plots, which will be difficult to present and analyze within the scope of a single manuscript. For studying the spin structure of the $S = 0, S_z = 0$ states at $B = 0$, however, we found that knowledge of a single CPD, let's say $\mathcal{P}_{\uparrow\downarrow}$ (see Figs. 48 − 49) is sufficient in the regime of Wigner-molecule formation. Indeed, the specific angle θ specifying the spin function $\mathcal{X}_{00}$ Eq.(3.34)

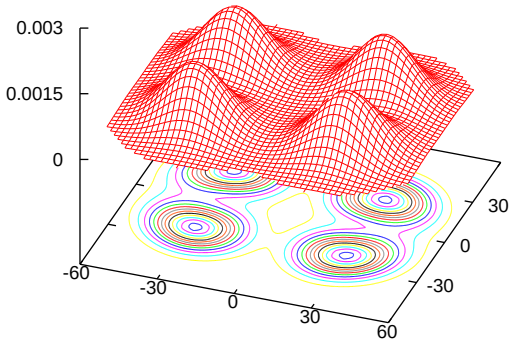

Figure 44: Electron densities at $B = 0$ for the ground state (with $S = 0, S_z = 0$, parity $P_{xy} = 1$, and energy $E = 111.361$ meV) of $N = 4$ electrons in a double quantum dot with interdot separation $d = 30$ nm. Case of strong Coulomb repulsion ($\kappa = 2$). Remaining parameters: $\epsilon^b = 0.5$, $m^* = 0.07 m_e$, $K = 50$. Distances in nm. Vertical axis in arbitrary units (with the same scale for the two figures 42 and 44).

corresponding to the CPDs portrayed in Figs. 48 − 49 can be determined through the following procedure:

We designate with roman indices I, II, III, and IV the four quadrants of the (x, y) plane, starting with the upper left quadrant and going clockwise (see Fig. 48). In the case of a $4e$ Wigner-molecule, a single electron is localized within each quadrant. The same roman indices designate also the positions of the localized electrons in each of the six Slater determinants (e.g., in the $|\uparrow\uparrow\downarrow\downarrow\rangle$) that enter into the spin function $\mathcal{X}_{00}$ in Eq. (3.34). We take always the fixed point to correspond to the fourth (IV) quadrant. An inspection of Eq. (3.34) shows that only three Slater determinants in $\mathcal{X}_{00}$ contribute to $\mathcal{P}_{\uparrow\downarrow}$, namely $|\uparrow\uparrow\downarrow\downarrow\rangle$, $|\uparrow\downarrow\uparrow\downarrow\rangle$, and $|\downarrow\uparrow\uparrow\downarrow\rangle$. From these three Slater determinants, only the first and the second contribute to the conditional probability $\Pi_{\uparrow\downarrow}(I)$ of finding another electron with spin-up in quadrant I; this corresponds to

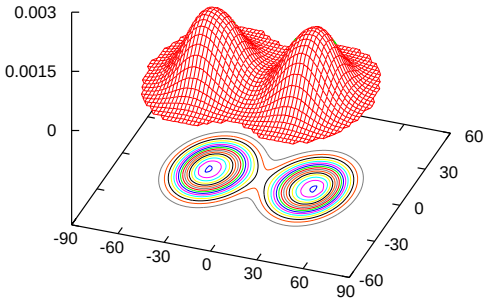

Figure 45: Electron densities at $B = 0$ for $N = 4$ electrons in a double quantum dot with interdot separation $d = 60$ nm. Case of weak Coulomb repulsion ($\kappa = 12.5$). Remaining parameters: $\epsilon^b = 0.5$, $m^* = 0.07 m_e$. Distances in nm. Vertical axis in arbitrary units (with the same scale for all three figures $45 - 47$).

the volume under the hump of the EXD CPD in quadrant I (see, e.g., the hump in Fig. 48). Taking the squares of the coefficients of $|\uparrow\uparrow\downarrow\downarrow\rangle$ and $|\uparrow\downarrow\uparrow\downarrow\rangle$ in Eq. (3.34), one gets

$$\Pi_{\uparrow\downarrow}(I) \propto \frac{\sin^2\theta}{3} + \left(\frac{1}{2}\cos\theta - \sqrt{\frac{1}{12}}\sin\theta\right)^2 . \tag{4.8}$$

Similarly, one finds that only $|\uparrow\uparrow\downarrow\downarrow\rangle$ and $|\downarrow\uparrow\uparrow\downarrow\rangle$ contribute to $\Pi_{\uparrow\downarrow}(II)$, and that

$$\Pi_{\uparrow\downarrow}(II) \propto \frac{\sin^2\theta}{3} + \left(\frac{1}{2}\cos\theta + \sqrt{\frac{1}{12}}\sin\theta\right)^2 . \tag{4.9}$$

Integrating under the humps of the EXD CPD in quadrants I and II, we determine numerically the ratio $\Pi_{\uparrow\downarrow}(I)/\Pi_{\uparrow\downarrow}(II)$, which allows us to specify the absolute value of θ (within the interval $-90° \leq \theta \leq 90°$) via the expressions in Eqs. (4.8) and (4.9). The restriction to the absolute value of θ is a result of the squares of the sine and cosine entering in $\Pi_{\uparrow\downarrow}(I)$ and $\Pi_{\uparrow\downarrow}(II)$. To obtain the actual sign of θ, additional information

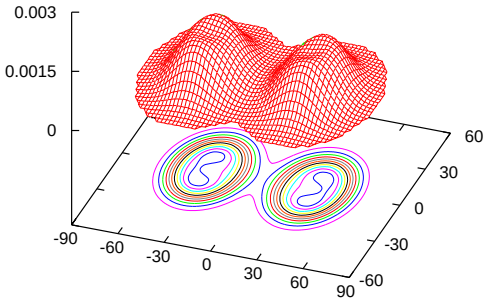

Figure 46: Electron densities at $B = 0$ for $N = 4$ electrons in a double quantum dot with interdot separation $d = 60$ nm. Case of intermediate Coulomb repulsion ($\kappa = 6$). Remaining parameters: $\epsilon^b = 0.5$, $m^* = 0.07 m_e$. Distances in nm. Vertical axis in arbitrary units (with the same scale for three figures $45 - 47$).

is needed: for example the ratio $\Pi_{\uparrow\downarrow}(I)/\Pi_{\uparrow\downarrow}(III)$ can be used in a similar way, where

$$\Pi_{\uparrow\downarrow}(III) \propto \left(\frac{1}{2}\cos\theta - \sqrt{\frac{1}{12}}\sin\theta\right)^2 + \left(\frac{1}{2}\cos\theta + \sqrt{\frac{1}{12}}\sin\theta\right)^2 . \tag{4.10}$$

Using the method described above, we find that $\theta \approx -60°$ for the EXD ground state at $d = 60$ nm (longer interdot distance) and $\kappa = 2$ (strong repulsion; see Fig. 48), and the corresponding spin function simplifies to

$$\mathcal{X}_{00} = -\frac{1}{2}|\uparrow\uparrow\downarrow\downarrow\rangle + \frac{1}{2}|\uparrow\downarrow\uparrow\downarrow\rangle + \frac{1}{2}|\downarrow\uparrow\downarrow\uparrow\rangle - \frac{1}{2}|\downarrow\downarrow\uparrow\uparrow\rangle. \tag{4.11}$$

Remarkably, increasing the interdot barrier from $\epsilon^b = 0.5$ (Fig. 48) to $\epsilon^b = 6$ (Fig. 49), while keeping the other parameters constant, does not influence much the composition of the associated spin function, which remains that given by Eq. (4.11). This happens in spite of the visible change in the degree of localization in the electronic orbitals, with the higher interdot-barrier case exhibiting a sharper localization. In

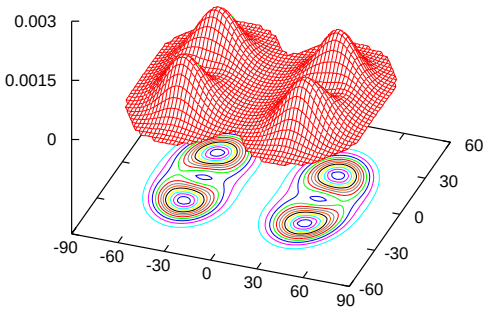

Figure 47: Electron densities at $B = 0$ for $N = 4$ electrons in a double quantum dot with interdot separation $d = 60$ nm. Case of strong Coulomb repulsion ($\kappa = 2$). Remaining parameters: $\epsilon^b = 0.5$, $m^* = 0.07m_e$. Distances in nm. Vertical axis in arbitrary units (with the same scale for all three figures $45 - 47$).

Fig. 50, we display the $\mathcal{P}_{\uparrow\downarrow}$ CPD for an excited state with $S = 0, S_z = 0$ (having $P_{xy} = 1$ and energy $E = 95.017$ meV), with the remaining parameters being the same as in Fig. 48. For this case, following an analysis as described above, we found the angle $\theta \approx 30°$, which is associated with a spin function of the form

$$\begin{aligned}\mathcal{X}_{00} \;=\; & \frac{1}{2\sqrt{3}}|\uparrow\uparrow\downarrow\downarrow\rangle + \frac{1}{2\sqrt{3}}|\uparrow\downarrow\uparrow\downarrow\rangle - \frac{1}{\sqrt{3}}|\uparrow\downarrow\downarrow\uparrow\rangle \\ & -\frac{1}{\sqrt{3}}|\downarrow\uparrow\uparrow\downarrow\rangle + \frac{1}{2\sqrt{3}}|\downarrow\uparrow\downarrow\uparrow\rangle + \frac{1}{2\sqrt{3}}|\downarrow\downarrow\uparrow\uparrow\rangle.\end{aligned} \tag{4.12}$$

We note that the spin functions in Eqs. (4.11) and (4.12) are orthogonal.

In Fig. 51, we display the $\mathcal{P}_{\uparrow\downarrow}$ CPD for the ground state with $S = 0, S_z = 0$ (having $P_{xy} = 1$ and energy $E = 111.361$ meV) and for the shorter interdot distance $d = 30$ nm. For this case, we found an angle $\theta \approx -63.08°$, which corresponds to the

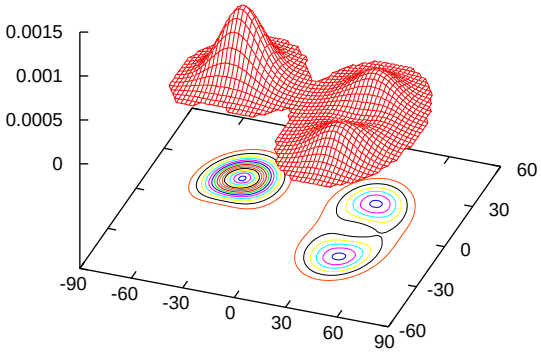

Figure 48: CPD $\mathcal{P}_{\uparrow\downarrow}$ at $B = 0$ for the ground state (with $S = 0, S_z = 0$, parity $P_{xy} = 1$, and energy $E = 94.516$ meV) of $N = 4$ electrons in a double quantum dot with interdot separation $d = 60$ nm. Case of strong Coulomb repulsion ($\kappa = 2$) with an interdot barrier $\epsilon^b = 0.5$. Remaining parameters: $m^* = 0.07m_e$. Distances in nm. Vertical axis in arbitrary units (with the same scale for all seven figures 48 − 54). The fixed point is located at the maximum of the hump in the lower-left quadrant of the corresponding electron density, i.e., at $\mathbf{r}_0 =(-40$ nm, -21 nm).

following spin function:

$$\begin{aligned}\mathcal{X}_{00} &= -0.5148|\uparrow\uparrow\downarrow\downarrow\rangle + 0.4838|\uparrow\downarrow\uparrow\downarrow\rangle + 0.031|\uparrow\downarrow\downarrow\uparrow\rangle \\ &\quad 0.031|\downarrow\uparrow\uparrow\downarrow\rangle + 0.4838|\downarrow\uparrow\downarrow\uparrow\rangle - 0.5148|\downarrow\downarrow\uparrow\uparrow\rangle.\end{aligned} \tag{4.13}$$

We see that the difference in interdot distance resulted in a slight variation of the spin functions [compare Eq. (4.11) with Eq. (4.13)].

4.3.3 Examples of $S = 1$, $S_z = 0$ EXD states

In this section, we turn our attention to partially polarized EXD states with $S = 1$.

In Fig. 52, we display the $\mathcal{P}_{\uparrow\downarrow}$ CPD at $B = 0$ for an excited state with $S = 1, S_z = 0$, parity $P_{xy} = 1$, and energy $E = 94.757$ meV at the longer interdot separation

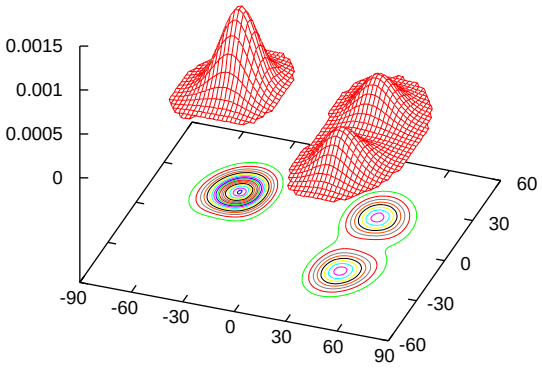

Figure 49: CPD $\mathcal{P}_{\uparrow\downarrow}$ at $B = 0$ for the ground state (with $S = 0, S_z = 0$, parity $P_{xy} = 1$, and energy $E = 96.811$ meV) of $N = 4$ electrons in a double quantum dot with interdot separation $d = 60$ nm. Case of strong Coulomb repulsion ($\kappa = 2$) with an interdot barrier $\epsilon^b = 6$. Remaining parameters: $m^* = 0.07m_e$. Distances in nm. Vertical axis in arbitrary units (with the same scale for all seven figures $48 - 54$). The fixed point is located at the maximum of the hump in the lower-left quadrant of the corresponding electron density, i.e., at $\mathbf{r}_0 =(-40$ nm, -21 nm). This is a case with a higher interdot barrier compared to Fig. 48 where $\epsilon^b = 0.5$.

$d = 60$ nm. Again we consider the case of strong Coulomb repulsion ($\kappa = 2$) with interdot barrier $\epsilon^b = 0.5$. The corresponding spin function $\mathcal{X}_{10}$ [Eq. (3.35)] depends on two different angles θ and ϕ, and one needs at least two different CPDs for determining their specific values. To this effect, we display the $\mathcal{P}_{\downarrow\downarrow}$ CPD for the same state in Fig. 53.

The specific values of θ and ϕ associated with the CPDs in Figs. 52 and 53 can be determined through the ratios $\Pi_{\downarrow\downarrow}(I)/\Pi_{\downarrow\downarrow}(II)$ and $\Pi_{\downarrow\downarrow}(I)/\Pi_{\downarrow\downarrow}(III)$ (see Fig. 53), where

$$\Pi_{\downarrow\downarrow}(I) = \left(\sqrt{\frac{1}{6}} \sin\theta \sin\phi - \sqrt{\frac{1}{12}} \sin\theta \cos\phi - \frac{1}{2} \cos\theta \right)^2 , \tag{4.14}$$

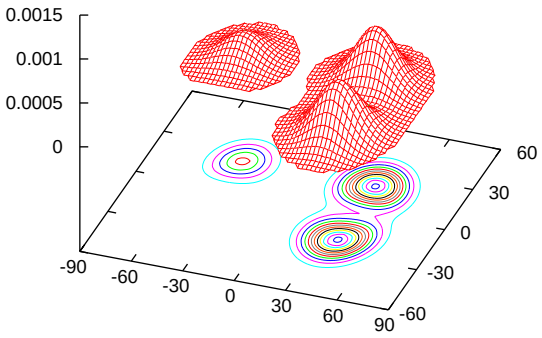

Figure 50: CPD $\mathcal{P}_{\uparrow\downarrow}$ at $B = 0$ for the second excited state (with $S = 0, S_z = 0$, parity $P_{xy} = 1$, and energy $E = 95.017$ meV) of $N = 4$ electrons in a double quantum dot with interdot separation $d = 60$ nm. Case of strong Coulomb repulsion ($\kappa = 2$) with an interdot barrier $\epsilon^b = 0.5$. Remaining parameters: $m^* = 0.07 m_e$. Distances in nm. Vertical axis in arbitrary units (with the same scale for all seven figures $48 - 54$). The fixed point is located at the maximum of the hump in the lower-left quadrant of the corresponding electron density, i.e., at $\mathbf{r}_0 =(-40$ nm, -21 nm).

$$\Pi_{\downarrow\downarrow}(II) = \left(\sqrt{\frac{1}{6}} \sin\theta \sin\phi - \sqrt{\frac{1}{12}} \sin\theta \cos\phi + \frac{1}{2} \cos\theta \right)^2 , \tag{4.15}$$

and

$$\Pi_{\downarrow\downarrow}(III) = \left(\sqrt{\frac{1}{6}} \sin\theta \sin\phi + \sqrt{\frac{1}{3}} \sin\theta \cos\phi \right)^2 . \tag{4.16}$$

Using Eqs. (4.14) $-$ (4.16) and the numerical values of the ratios $\Pi_{\downarrow\downarrow}(I)/\Pi_{\downarrow\downarrow}(II)$ and $\Pi_{\downarrow\downarrow}(I)/\Pi_{\downarrow\downarrow}(III)$ (specified via a volume integration under the humps of the EXD CPDs), we determined that $\theta = -45°$ and $\sin\phi = -\sqrt{2/3}$, $\cos\phi = \sqrt{1/3}$ (i.e., $\phi \approx -54.736°$). Thus, the corresponding spin function reduces to the simple form

$$\mathcal{X}_{10} = \sqrt{\frac{1}{2}} |\uparrow\downarrow\uparrow\downarrow\rangle - \sqrt{\frac{1}{2}} |\downarrow\uparrow\downarrow\uparrow\rangle. \tag{4.17}$$

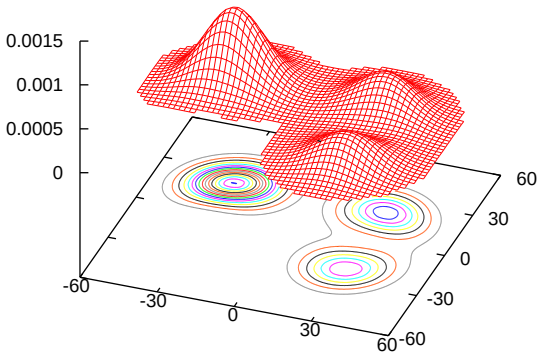

Figure 51: CPD $\mathcal{P}_{\uparrow\downarrow}$ at $B = 0$ for the ground state (with $S = 0, S_z = 0$, parity $P_{xy} = 1$, and energy $E = 111.361$ meV) of $N = 4$ electrons in a double quantum dot at the shorter interdot separation $d = 30$ nm. Case of strong Coulomb repulsion ($\kappa = 2$) with interdot barrier $\epsilon^b = 0.5$. Remaining parameters: $m^* = 0.07m_e$. Distances in nm. Vertical axis in arbitrary units (with the same scale for all seven figures $48 - 54$). The fixed point is located at the maximum of the hump in the lower-left quadrant of the corresponding electron density, i.e., at $\mathbf{r}_0 =(-29$ nm, -19 nm).

In Fig. 54, we display the $\mathcal{P}_{\uparrow\downarrow}$ CPD at $B = 0$ for a similar excited state as in Fig. 52 (with $S = 1, S_z = 0$, parity $P_{xy} = 1$, and energy $E = 111.438$ meV) of $N = 4$ electrons at the shorter interdot separation $d = 30$ nm. Again we consider the case of strong Coulomb repulsion ($\kappa = 2$) with interdot barrier $\epsilon^b = 0.5$. We note that the localization of electrons is stronger for the longer interdot distance [compare Fig. 52 with Fig. 54]. This difference, however, does not influence the coefficients entering inti the associated spin function, which we found remains very close to the specific form in Eq. (4.17).

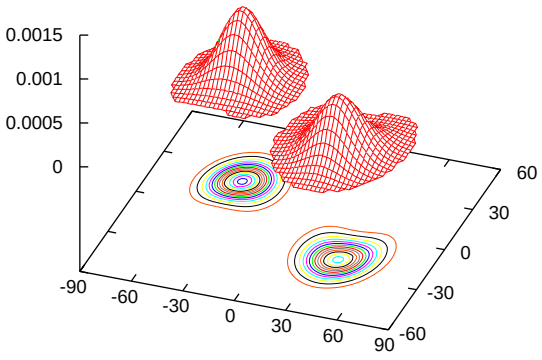

Figure 52: $\mathcal{P}_{\uparrow\downarrow}$ CPD at $B = 0$ for an excited state (with $S = 1, S_z = 0$, parity $P_{xy} = 1$, and energy $E = 94.757$ meV) of $N = 4$ electrons in a double quantum dot at the longer interdot separation $d = 60$ nm. Case of strong Coulomb repulsion ($\kappa = 2$) with interdot barrier $\epsilon^b = 0.5$. Remaining parameters: $m^* = 0.07m_e$. Distances in nm. Vertical axis in arbitrary units (with the same scale for all seven figures $48 - 54$). The fixed point is located at the maximum of the hump in the lower-left quadrant of the corresponding electron density, i.e., at $\mathbf{r}_0 =(-40$ nm, -21 nm). Note that this is a case with $S = 1$; previous figures investigated $S = 0$ cases.

4.4 Results: Spin-resolved conditional probability distributions at $B \neq 0$

In Figs. 55 and 56 we display EXD CPDs at a finite value of the magnetic field, and precisely at $B = 2$ T, for the two states of the low-energy band with $S = 0$, $S_z = 0$ (at the larger interdot separation $d = 60$ nm and strong interelectron repulsion $\kappa = 2$). This value of B was chosen to lie beyond the crossing point for the six states of the low-energy band (which happens at $B \sim 1$ T; see Fig. 41). Comparison with the CPDs of the corresponding states at zero magnetic field (see Figs. 48 and 50) shows that the spin structure of the associated Wigner molecule varies rather slowly with the increasing magnetic field. The small variation is mainly reflected in the roundness

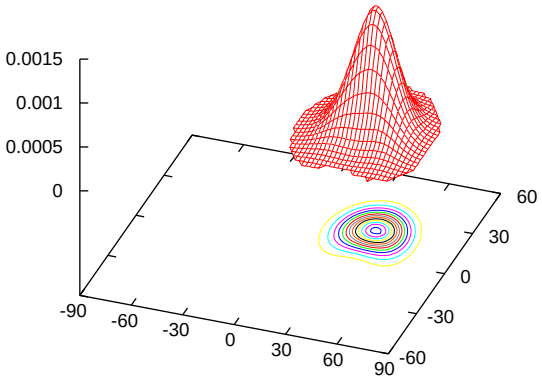

Figure 53: $\mathcal{P}_{\downarrow\downarrow}$ CPD at $B = 0$ for the same excited state as in Fig. 52 (with $S = 1, S_z = 0$, parity $P_{xy} = 1$, and energy $E = 94.757$ meV) of $N = 4$ electrons in a double quantum dot at the longer interdot separation $d = 60$ nm. Case of strong Coulomb repulsion ($\kappa = 2$) with interdot barrier $\epsilon^b = 0.5$. Remaining parameters: $m^* = 0.07m_e$. Distances in nm. Vertical axis in arbitrary units (with the same scale for all seven figures $48 - 54$). The fixed point is located at the maximum of the hump in the lower-left quadrant of the corresponding electron density, i.e., at $\mathbf{r}_0 =(-40$ nm, -21 nm).

of the humps (compare the oblong contour lines at $B = 0$ with the more circular ones at $B = 2$ T; this reflects an increasing electron localization at larger B).

In detail, following the height of the humps in the left upper quadrants, one sees that the CPD in Fig. 55 (case of *lower-energy* state at $B = 2$ T with $S = 0$ and $P_{xy} = 1$) corresponds precisely to that of Fig. 48 (case of *lower-energy* state at $B = 0$ with $S = 0$ and $P_{xy} = 1$). Similarly, the CPD in Fig 56 at $B = 2$ T (*higher-energy* state) corresponds to that of Fig. 50 at $B = 0$ (*higher-energy* state). From this one concludes that the two states with $S = 0$ and $P_{xy} = 1$ do not really cross at the 'crossing' point at $B \sim 1$ T. In reality, this point is an anticrossing point for these two states, although the anticrossing gap is very small to be seen with the naked eye. This behavior agrees with that expected from states having the same quantum

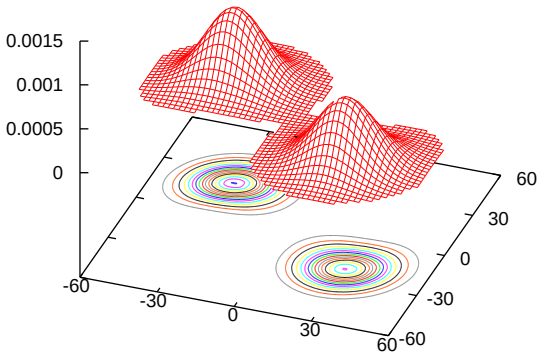

Figure 54: $\mathcal{P}_{\uparrow\downarrow}$ CPD at $B = 0$ for a similar excited state as in Fig. 52 (with $S = 1, S_z = 0$, parity $P_{xy} = 1$, and energy $E = 111.438$ meV) of $N = 4$ electrons in a double quantum dot at the shorter interdot separation $d = 30$ nm. Case of strong Coulomb repulsion ($\kappa = 2$) with interdot barrier $\epsilon^b = 0.5$. Remaining parameters: $m^* = 0.07m_e$. Distances in nm. Vertical axis in arbitrary units (with the same scale for all seven figures $48 - 54$). The fixed point is located at the maximum of the hump in the lower-left quadrant of the corresponding electron density, i.e., at $\mathbf{r}_0 =(-29$ nm, -19 nm).

numbers. We checked that a similar observation applies for the two other states in the low-energy band having the same quantum numbers, i.e., those having $S = 1$ and $P_{xy} = -1$.

4.5 Discussion

4.5.1 Finite Heisenberg spin clusters

Using the spin-resolved CPDs, we showed that the EXD many-body wave functions in the Wigner-molecule regime can be expressed as a linear superposition of a small number of Slater determinants and that this superposition exhibits the structure expected from the theory of many-body spin functions. This finding naturally suggests a strong analogy with the field of nanomagnets and quantum magnetism, usually

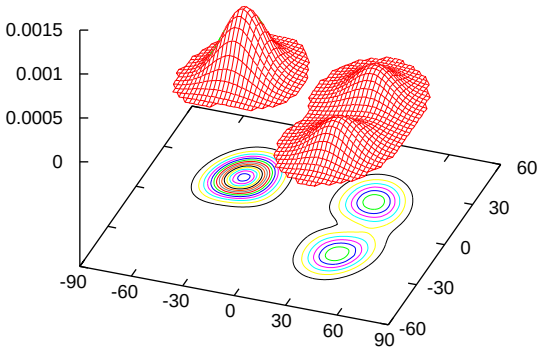

Figure 55: $\mathcal{P}_{\uparrow\downarrow}$ CPD for the lowest-energy state at $B = 2$ T with $S = 0$, $S_z = 0$, parity $P_{xy} = 1$, and energy $E = 94.605$ meV) of $N = 4$ electrons in a double quantum dot at the longer interdot separation $d = 60$ nm. Case of strong Coulomb repulsion ($\kappa = 2$) with interdot barrier $\epsilon^b = 0.5$. Remaining parameters: $m^* = 0.07m_e$. Distances in nm. Vertical axis in arbitrary units (with the same scale for all nine figures $48 - 56$). The fixed point is located at $\mathbf{r}_0 = (-40$ nm, -21 nm).

studied via the explicitly spin-dependent model effective Hamiltonian known as the Heisenberg Hamiltonian, [41, 52, 37] given by:

$$\mathcal{H}'_H = \sum_{i,j} J_{ij}\mathbf{S}_i{\cdot}\mathbf{S}_j - \mathbf{Q}\sum_i \mathbf{S}_i, \tag{4.18}$$

where J_{ij} are the exchange integrals between spins on sites i and j. Even in its more familiar, simplest form

$$\mathcal{H}_H = J\sum_{i,j} \mathbf{S}_i{\cdot}\mathbf{S}_j, \tag{4.19}$$

that is that of the spin-1/2 Heisenberg antiferromagnet with nearest-neighbor interactions only, it is well known that the zero-temperature (at $B = 0$) solutions of Hamiltonian (4.19) involve radically different forms as a function of geometry, dimensionality, and size.

It is natural to compare the EXD spin functions determined in the cpd Section

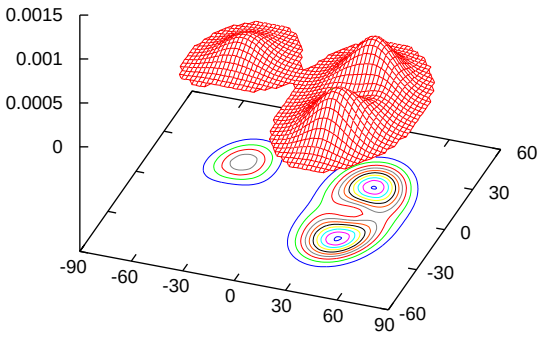

Figure 56: $\mathcal{P}_{\uparrow\downarrow}$ CPD for the excited state at $B = 2$ T with $S = 0, S_z = 0$, parity $P_{xy} = 1$, and energy $E = 95.047$ meV) of $N = 4$ electrons in a double quantum dot at the longer interdot separation $d = 60$ nm. Case of strong Coulomb repulsion ($\kappa = 2$) with interdot barrier $\epsilon^b = 0.5$. Remaining parameters: $m^* = 0.07m_e$. Distances in nm. Vertical axis in arbitrary units (with the same scale for all nine figures $48 - 56$). The fixed point is located at $\mathbf{r}_0$ =(-40 nm, -21 nm).

with well known solutions of the Heisenberg Hamiltonian [Eq. (4.19)] when the four spins are located on four sites arranged in a perfect square.[52, 13] (The perfect-square arrangement arises [8] also in the case of formation of a four-electron Wigner molecule in a single circular quantum dot.) In this case, the ground state of $\mathcal{H}_H$ is the celebrated resonating valence bond (RVB) state[52, 13] which forms the basic block in many theoretical approaches aiming at describing high-temperature superconductors.[5] The RVB state has quantum numbers $S = 0$, $S_z = 0$ and is given by[52, 13]

$$\begin{aligned}\mathcal{X}_{00}^{\rm RVB} &= \frac{1}{2\sqrt{3}}|\uparrow\uparrow\downarrow\downarrow\rangle + \frac{1}{2\sqrt{3}}|\uparrow\downarrow\downarrow\uparrow\rangle + \frac{1}{2\sqrt{3}}|\downarrow\downarrow\uparrow\uparrow\rangle \\ &+\frac{1}{2\sqrt{3}}|\downarrow\uparrow\uparrow\downarrow\rangle - \frac{1}{\sqrt{3}}|\uparrow\downarrow\uparrow\downarrow\rangle - \frac{1}{\sqrt{3}}|\downarrow\uparrow\downarrow\uparrow\rangle.\end{aligned} \tag{4.20}$$

Although the excited-state EXD $\mathcal{X}_{00}^{(2)}$ in the quantum-double-dot case portrayed

in Fig. (50) appears to be similar to the RVB $\mathcal{X}_{00}^{\rm RVB}$ [Eq. (4.20)], they are not equal. Indeed the coefficients of the pair of Slater determimants $\mid\uparrow\downarrow\uparrow\downarrow\rangle$ and $\mid\downarrow\uparrow\downarrow\uparrow\rangle$ have been interchanged with those of $\mid\downarrow\uparrow\uparrow\downarrow\rangle$ and $\mid\uparrow\downarrow\downarrow\uparrow\rangle$.

Similar observations apply also to the $S=0$ and $S_z=0$ remaining states that are orthogonal to $\mathcal{X}_{00}^{(2)}$ [see $\mathcal{X}_{00}^{(1)}$ in Eq. (4.11); case of double quantum dot] and to $\mathcal{X}_{00}^{\rm RVB}$ (case of a perfect square). The latter is given by[52]

$$\mathcal{X}_{00}^{\rm square,exci}=-\frac{1}{2}\mid\uparrow\uparrow\downarrow\downarrow\rangle+\frac{1}{2}\mid\uparrow\downarrow\downarrow\uparrow\rangle+\frac{1}{2}\mid\downarrow\uparrow\uparrow\downarrow\rangle-\frac{1}{2}\mid\downarrow\downarrow\uparrow\uparrow\rangle. \tag{4.21}$$

In particular, one finds

$$\mathcal{X}_{00}^{(2)}=-\frac{1}{2}\mathcal{X}_{00}^{\rm RVB}-\frac{\sqrt{3}}{2}\mathcal{X}_{00}^{\rm square,exci} \tag{4.22}$$

and

$$\mathcal{X}_{00}^{(1)}=-\frac{\sqrt{3}}{2}\mathcal{X}_{00}^{\rm RVB}+\frac{1}{2}\mathcal{X}_{00}^{\rm square,exci}. \tag{4.23}$$

We note that the differences in the $\mathcal{X}_{00}$ spin functions between the DQD case (having a parallelepid arrangement) with the perfect-square case are also reflected in the $\mathcal{P}_{\uparrow\downarrow}$ CPDs. Indeed the CPDs of the DQD exhibit equal-height humps along the smaller side of the parallelepid while those of the perfect-square configuration (and/or circular quantum dot) exhibit equal-height humps along a diagonal [8].

Néel antiferromagnetic ordering, where the average spin per site $<S_j^z>=(-1)^{j+1}/2$, is an important magnetic phenomenon in the thermodymanic limit[13] associated with breaking of the total-spin symmetry. The finite size magnetic clusters discussed here exhibit a sharply different behavior in this respect. Indeed, as discussed in Ref. [13], the four-site Néel state is the single Slater determinant $\mid\downarrow\uparrow\downarrow\uparrow\rangle$ (or $\uparrow\downarrow\uparrow\downarrow\rangle$). It is clear that the total-spin conserving EXD functions $\mathcal{X}_{00}$ are multideterminental and have an average spin per localized electron (per site) $<S_j^z>=0$.

We concur with Ref. [13] that the phenomenon of Néel antifferomagnetism is not applicable to assemblies of few electrons. In the next section, we argue that the appropriate concept for WM states is that of *spin entanglement*.

4.5.2 Spin entanglement

In the previous sections, we showed that the EXD wave functions in the regime of Wigner-molecule formation can be approximated as a superposition of a small number of Slater determinants corresponding to well structured spin functions; see, e.g., $\mathcal{X}_{00}^{(1)}$ in Eq. (4.11). This is a great simplification compared to the initial EXD superposition [Eq. (3.8)], where the counting index is usually $I \geq 500,000$. This reduction of the molecular EXD solutions to their equivalent spin functions enables one to investigate their properties regarding fundamental quantum behavior associated with quantum correlations and fluctuations beyond the mean field.

The smallest number of Slater determinants contributing to the spin functions $\mathcal{X}$'s with $S_z = 0$ is two. We note that for $S_z = 0$ a single determinant of four localized spin orbitals cannot conserve the total spin, and thus mean-field approaches like DFT (which are associated with a single determinant) are unable to describe quantum fluctuations and entanglement (see below). In particular, we note that the spin functions $\mathcal{X}$'s cannot be further reduced to simpler superpositions containing a smaller number of Slater determinants. As a result, they faithfully represent the extent of probabilistic quantum interconnection between the individual electrons participating in the system as described by an EXD solution. This quantum interconnection is widely referred to as *entanglement* [55, 1, 23] and generates correlations between the physical observables of the individual electrons (e.g., spins), even though the individual electrons are spatially separated. This existence of quantum interconnectivity independently of spatial separation has made entanglement the central instrument for the development of the fields of quantum information, such as quantum teleportation, quantum cryptography, and quantum computing. With their localized electrons, Wigner molecules in quantum dots offer another physical solid-state nanosystem where entanglement may be realized and studied.

The mathematical theory of entanglement is still developing and includes several

directions. One way to study entanglement is through the use of properly defined measures of entanglement, e,g, the von Neumann entropy which utilizes the single-particle density matrix. Another way is to catalog and specify classes of entangled states that share common properties regarding multipartite entanglement. A well known class of N-qubit entangled states are the Dicke states [11, 12, 19, 18], which most often are taken to have the symmetric form:

$$\mathcal{X}_{N,k}^{\text{Dicke}} = \left(\begin{array}{c} N \\ k \end{array} \right)^{-1/2} (|\underbrace{11\ldots1}_{k}00\ldots0\rangle + \text{Perm}). \tag{4.24}$$

Each qubit is a linear superposition of two single-particle states denoted by 0 or 1, and the symbol 'Perm' stands for all remaining permutations. The 0 or 1 do not have to be necessarily up or down 1/2-spin states. Two-level atoms in linear ultracold traps have already been used as an implementation of a qubit. Dicke states appear in many physical processes like superradiance and superfluorescence. They can also be realized with photons, where the qubits correspond to the polarization degree of freedom [18].

In the 1/2-spin case of fermions (e.g., for electrons), the Dicke states of Eq. (4.24) correspond to a fully symmetric flip of k out of N localized spins. It is apparent that the four-qubit fully polarized ($S = 2$ with spin projection S_z=0) EXD $\mathcal{X}_{20}$ of Eq. (3.36) is of the Dicke form displayed above in Eq. (4.24). On the other part, the DQD EXD states (with $S_z = 0$) studied with $S = 0$ and/or $S = 1$ represent a natural generalization of Eq. (4.24) to the class of *asymmetric* Dicke states. We hope that our results will motivate experimental research aiming at the realization and control of such states in DQD electronic devices.

Before leaving this section, we note that Dicke states with a single flip ($k = 1$) are known as W states.[65, 61] For $N = 4$ electrons, the latter states are related to EXD solutions with $S_z = \pm 1$. For the connection between W states and EXD states for $N = 3$ electrons in anisotropic quantum dots, see Ref.[77]. W states have already

been realized experimentally using two-level ultracold ions in linear traps [17].

4.6 Conclusion

Extensive investigations of lateral double quantum dots containing four electrons were performed using the exact-diagonalization method, as a function of interdot separation, applied magnetic field, and strength of interelectron repulsion. Novel quantum behavior was discovered compared to circular QDs, concerning both energy spectra and quantum entanglement aspects. Thus it is hoped that the present work will motivate further experimental studies on lateral DQDs beyond the two-electron case [76, 43].

Specifically it was found that, as a function of the magnetic field, the energy spectra exhibit a low-energy band consisting of a group of six states, and that this number six is not accidental, but a consequence of the conservation of the total spin and of the ensuing spin degeneracies and supermultiplicities expressed in the branching diagram. These six states appear to cross at a single value of the magnetic field, and the crossing point gets sharper for larger interdot distances. As the strength of the Coulomb repulsion increases, the six states tend to become degenerate and a well defined energy gap separates them from the higher-in-energy excited states.

The formation of the low-energy band is a consequence of the localization of the four electrons within each dot (with two electrons on each dot). The result is formation (with increasing strength of the Coulomb repulsion) of a Wigner supermolecule, with the four localized electrons at the corners of a rectangular parallelogram. Using the spin-resolved pair-correlation functions, it was shown that one can map the EXD many-body wave functions to the spin functions associated with the four localized electrons. This mapping led us naturally to studying analogies with finite systems described by model Heisenberg Hamiltonians (referred to often as finite Heisenberg clusters). It was found that the determination of the equivalent spin functions enables

investigations concerning the entanglement properties of the EXD solutions. In particular, it was shown that the formation of Wigner supermolecules generates strongly entangled states known in the literature of quantum information as N-qubit Dicke states [12, 19, 18].

REFERENCES

[1] A. Einstein, B. P. and Rosen, N. *Phys. Rev.*, vol. **47**, p. 0777, 1935.

[2] A. Ghosal, A. D. Guclu, C. J. U. D. U. and Baranger, U. H. *Phys. Rev. B*, vol. **76**, p. 085341, 2007.

[3] A. Laio, J. Vande Vondele, U. R. *J. Chem. Phys.*, vol. **116**, p. 6941, 2002.

[4] Allen, M. P. and Tildesley, D. J., *Computer Simulation of Liquids*. Oxford: Clarendon.

[5] Anderson, P. *Physics Today*, p. 8, 2008.

[6] Ashoori, R. C. *Nature*, vol. **379**, p. 413, 1996.

[7] Barnett, R. N. and Landman, U. *Phys. Rev. B*, vol. **48**, p. 2081, 1993.

[8] C. Shi, G. S. J. and Jain, J. K. *Phys. Rev. B*, vol. **75**, p. 165302, 2007.

[9] D. M. Ceperley, B. J. A. *Phys. Rev. Lett.*, vol. **45**, p. 566, 1980.

[10] D. M. Zumbuhl, C. M. Marcus, M. P. H. and Gossard, A. C. *Phys. Rev. Lett.*, vol. **93**, p. 256801, 2004.

[11] Dicke, R. H. *Phys. Rev.*, vol. **93**, p. 99, 1954.

[12] F. Verstraete, J. Dehaene, B. D. M. and Verschelde, H. *Phys. Rev. A*, vol. **65**, p. 052112, 2002.

[13] Fazekas, P., *Lecture notes on electron correlation and magnetism*. Singapore: World Scientific.

[14] Frenkel, D. and Smit, B., *Understanding Molecular Simulation: form algorithms to applications*. San Diego, USA: Academic Press.

[15] G. Burkard, D. L. and DiVincenzo, D. P. *Phys. Rev. B*, vol. **59**, p. 2070, 1999.

[16] Geller, M. R. and Vignale, G. *Phys. Rev. B*, vol. **53**, 1996.

[17] Haffner, H. *Nature*, vol. **438**, p. 643, 2005.

[18] J. K. Korbicz, O. Guhne, M. L. H. H. C. F. R. *Phys. Rev. A*, vol. **74**, p. 052319, 2006.

[19] J. K. Stockton, J. M. Geremia, A. C. D. and Mabuchi, H. *Phys. Rev. A*, vol. **67**, p. 022112, 2003.

[20] J. P. Perdew, K. B. and Ernzerhof, M. *Phys. Rev. Lett.*, vol. **77**, p. 3865, 1996.

[21] J. P. Perdew, W. Y. *Phys. Rev. B*, vol. **33**, p. 8800, 1986.

[22] J. R. R. Verlet, A. E. Bragg, A. K. O. C. D. M. N. *Science*, vol. **310**, p. 93, 2005.

[23] L. Amico, R. Fazio, A. O. and Vedral, V. *Rev. Mod. Phys.*, vol. **80**, p. 517, 2008.

[24] L. Kleinman, D. M. B. *Phys. Rev. Lett.*, vol. **48**, p. 1425, 1982.

[25] L. P. Kouwenhoven, D. G. A. and Tarucha, S. *Rep. Prog. Phys.*, vol. **64**, p. 701, 2001.

[26] L. Turi, W. S. Sheu, P. J. R. *Science*, vol. **309**, p. 914, 2005.

[27] L. X. Zhang, D. V. M. and Leburton, J. P. *Phys. Rev. B*, vol. **74**, p. 205306, 2006.

[28] Loss, D. and DiVincenzo, D. P. *Phys. Rev. A*, vol. **57**, p. 120, 1998.

[29] M. Avinun-Kalish, M. Heiblum, O. Z. D. M. and Umansky, V. *Nature*, vol. **436**, p. 529, 2005.

[30] M. B. Tavernier, E. Anisimovas, F. M. P. B. S. J. A. and Bednarek, S. *Phys. Rev. B*, vol. **68**, p. 205305, 2003.

[31] M. Ciorga, A. S. Sachrajda, P. H. C. G. P. Z. S. J. Y. F. and Wasilewski, Z. *Phys. Rev. B*, vol. **61**, p. 16315, 2000.

[32] M. Eichinger, P. Tavan, J. H. M. P. *J. Chem. Phys.*, vol. **110**, p. 10452, 1999.

[33] M. Fuchs, M. S. *Computer Physics Communications*, vol. **119**, p. 67, 1999.

[34] M. Helle, A. H. and Nieminen, R. M. *Phys. Rev. B*, vol. **72**, p. 205329, 2005.

[35] M. Rontani, C. Cavazzoni, D. B. and Goldoni, G. *J. Chem. Phys.*, vol. **124**, p. 124102, 2006.

[36] M. Tavernier, E. Anisimovas, F. M. P. B. S. J. A. and Bednarek, S. *Phys. Rev. B*, vol. **68**, p. 205305, 2003.

[37] Manousakis, E. *Rev. Mod. Phys.*, vol. **63**, p. 1, 1991.

[38] Maruhn, J. and Greiner, W. *Z. Phys.*, vol. **251**, p. 431, 1972.

[39] N. Troullier, J. L. M. *Phys. Rev. B*, vol. **43**, p. 1993, 1991.

[40] P. A. Maksym, H. Imamura, G. P. M. and Aoki, H. *J. Phys.: Conden. Matter*, vol. **12**, p. 299, 2000.

[41] P. V. Hendriksen, S. L. and Lindgard, P. A. *Phys. Rev. B*, vol. **48**, p. 7259, 1993.

[42] Pauncz, R., *The Construction of Spin Eigenfunctions: An Exercise Book*. New York: Kluwer Academic/Plenum Publishers.

[43] R. Hanson, L. P. Kouwenhoven, J. R. P. S. T. and Vandersypen, L. M. K. *Rev. Mod. Phys.*, vol. **79**, p. 1217, 2007.

[44] R. N. Barnett, U. Landman, C. L. C. and Jortner, J. *J. Chem. Phys.*, vol. **88**, p. 4421, 1988.

[45] R. N. Barnett, U. Landman, C. L. C. and Jortner, J. *Chem. Phys. Lett.*, vol. **145**, p. 382, 1988.

[46] R. N. Barnett, U. Landman, C. L. C. J. J. *Phys. Rev. Lett.*, vol. **59**, p. 811, 1987.

[47] R. Woodworth, A. M. and Lidar, D. A. *J. Phys.: Condens. Mat.*, vol. **18**, 2006.

[48] Reed, M. *Sci. Am.*, vol. **268**, p. 118, 1993.

[49] Reimann, S. M. and Manninen, M. *Rev. Mod. Phys.*, vol. **74**, p. 1283, 2002.

[50] Ruan, W. Y. and Cheung, H. F. *J. Phys.: Condens. Matter*, vol. **11**, p. 435, 1999.

[51] S. H. Vosko, L. W. and Nusair, M. *Can. J. Phys.*, vol. **58**, p. 1200, 1980.

[52] S. Haas in *Lectures on the Physics of Strongly Correlated Systems XII*, e. b. A. A. and F. Mancini (AIP Conf. Proceedings Vol. 1014, Melville, N. Y. .

[53] S. J. Weiner, P. A. Kollmann, D. J. N. D. A. C. *J. Comp. Chem.*, vol. **7**, p. 230, 1986.

[54] S. Tarucha, D. G. Austing, T. H. R. J. v. d. H. and Kouwenhoven, L. P. *Phys. Rev. Lett.*, vol. **77**, p. 3613, 1996.

[55] Schrodinger, E. *Proc. Cambridge Phil. Soc.*, vol. **31**, p. 555, 1935.

[56] Schweigert, V. A. and Peeters, F. M. *Phys. Rev. B*, vol. **51**, p. 7700, 1995.

[57] Suzuki, Y. and Varga, K., *Stochastic Variational Approach to Quantum-Mechanical Few-Body Problems*. Germany: Springer.

[58] Szabo, A. and Ostlund, N. S., *Modern Quantum Chemistry*. New York: McGraw-Hill.

[59] Szafran, B. and Peeters, F. M. *Phys. Rev. B*, vol. **71**, p. 245314, 2005.

[60] U. Heiz, U. L., *Nanocatalysis*. New York, USA: Springer.

[61] V. Coffman, J. K. and Wootters, W. K. *Phys. Rev. A*, vol. **61**, p. 052306, 2000.

[62] Verlet, L. *Phys. Rev.*, vol. **159**, p. 98, 1967.

[63] W. C. Swope, H. C. Andersen, P. H. B. *et al.*. *J. Chem. Phys.*, vol. **76**, p. 637, 1982.

[64] W. D. Cornell, P. Cieplak, C. I. B. I. R. G. K. M. M. D. M. F. D. C. S. T. F. J. W. C. P. A. K. *J. Am. Chem. Soc.*, vol. **117**, p. 5179, 1995.

[65] W. Dur, G. V. and Cirac, J. I. *Phys. Rev. A*, vol. **62**, p. 062314, 2000.

[66] W. L. Jorgensen, J. Chandrasekhar, J. M. R. W. I. and Klein, M. L. *J. Chem. Phys.*, vol. **79**, p. 926, 1983.

[67] W. Y. Ruan, K. S. Chan, H. P. H. and Pun, E. Y. B. *J. Phys.: Condens. Matter*, vol. **12**, p. 3911, 2000.

[68] Wong, C. Y. *Phys. Lett.*, vol. **30B**, p. 61, 1969.

[69] Yannouleas, C. and Landman, U. *J. Phys. Chem.*, vol. **99**, p. 14577, 1995.

[70] Yannouleas, C. and Landman, U. *Phys. Rev. Lett.*, vol. **82**, p. 5325, 1999.

[71] Yannouleas, C. and Landman, U. *Phys. Rev. Lett.*, vol. **85**, p. 1726, 2000.

[72] Yannouleas, C. and Landman, U. *Phys. Rev. B*, vol. **66**, p. 115315, 2002.

[73] Yannouleas, C. and Landman, U. *J. Phys.: Condens. Matter*, vol. **14**, p. 591, 2002.

[74] Yannouleas, C. and Landman, U. *Phys. Rev. B*, vol. **68**, p. 035326, 2003.

[75] Yannouleas, C. and Landman, U. *Phys. Rev. B*, vol. **69**, p. 113306, 2004.

[76] Yannouleas, C. and Landman, U. *Rep. Prog. Phys.*, vol. **70**, p. 2067, 2007.

[77] Yuesong Li, C. Y. and Landman, U. *Phys. Rev. B*, vol. **76**, p. 245310, 2007.

VITA

Ying Li was born on July 16th, 1981 in Zhuzhou, Hunan Province, China. She started her undergraduate study in physics in Beijing University in 1999. After obtaining a Bachelor degree in 2003, she came to School of Physics, Georgia Institute of Technology to further her study. Since then, she has been working with Professor Uzi Landman on Quantum Mechanics simulations for water clusters and quantum dots.